# Geofísica Internacional

Revista Trimestral Publicada por el Instituto de Geofísica de la
Universidad Nacional Autónoma de México

# — Geofísica Internacional —

## Contents

Measurements of upper mantle shear wave anisotropy from a permanent network in southern Mexico.

**Steven A. C. van Benthem, Raúl W. Valenzuela, Gustavo J. Ponce**

385

# QVOA techniques for fracture characterization

Vladimir Sabinin

## Resumen

Se desarrollan nuevas técnicas de cálculo en el análisis del factor de calidad frente a la distancia fuente receptor y el acimut (QVOA) para caracterización de fracturas. Estas técnicas se aplican a datos sintéticos superficiales de reflexión con ruido.

Palabras clave: QVOA, factor de calidad, medio HTI, anisotropía sísmica, caracterización de yacimientos fracturados.

## Abstract

New computational techniques of QVOA analysis (Quality factor Versus Offset and Azimuth) for fracture characterization are developed. The techniques are applied to synthetic surface data of reflection with noise.

Key words: QVOA, quality factor, HTI medium, seismic anisotropy, fracture-reservoir characterization.

V. Sabinin
Instituto Mexicano del Petróleo
México D.F., México
*Corresponding author: vsabinin@yahoo.com*

## Introduction

Quality factor $Q$ is a seismic characteristic of attenuation property of a medium. By the value of $Q$-factor, one may estimate what kind of liquid fills pores of the medium (a reservoir characterization), because the attenuation of reservoir is due to presence of a liquid in the pores. For estimating factor $Q$, many different computational methods have been suggested (e.g., Tonn, 1991; Quan & Harris, 1997; Dasios et al., 2001; Zhang & Ulrych, 2002), as well as methodologies of its application to real data (Dasgupta & Clark, 1998).

QVOA analysis ($Q$-factor Versus Offset, and Azimuth) was first intended by Chichinina et al. (2004, 2005). Then it was further developed by Chichinina et al. (2006a, 2006b, 2006c), and Zhu and Tsvankin (2006). In fractured anisotropic media, anisotropy of $Q$ is present (Clark et al., 2001; Chichinina et al., 2004, 2005). Namely, the value of quality factor $Q$ depends on offset and azimuth. An approximate formula of this dependence was first suggested by Chichinina et al. (2006a, 2006b) for transversely isotropic media with a horizontal axis of symmetry (HTI), as well as an idea to apply it to estimation of principal fracture directions. Formulation of the QVOA analysis by Chichinina et al. (2006b) is similar to formulation of AVOA analysis (Amplitude Versus Offset, and Azimuth) by Rüger (1998) which gives good results in fracture characterization for media without attenuation (Sabinin & Chichinina, 2008).

Here computational techniques of QVOA analysis for estimation of fracture directions are suggested. Some of them are developed by analogy with known AVOA techniques (Mallik et al., 1998; Jenner, 2002). The others are original.

The QVOA techniques deal with estimating an attenuation factor (or quality factor $Q$) in surface data of reflection, what is not a trivial problem. Methodologies of such estimation of $Q$ are proposed by Behura & Tsvankin (2009), Shekar & Tsvankin (2011), Reine et al. (2012), and Sabinin (2012).

### Estimation of a symmetry axis angle by QVOA

Attenuation of wave amplitudes due to dispersion obeys a law (e.g., Tonn, 1991):

$$a(t) = a_0(t)\exp(-\beta r) \qquad (1)$$

where $r$ is a travel distance, and $\beta$ is an absorption coefficient.

Quality factor $Q$ is defined (e.g., Sheriff, 2002) as the ratio of $2\pi$ times the peak energy to the energy dissipated in a cycle:

$$Q = \frac{2\pi E}{\Delta E} \qquad (2)$$

It relates to $\beta$ as follows (Futterman, 1962):

$$\frac{2\pi}{Q} = 1 - e^{-2d} \qquad (3)$$

where $d = \dfrac{\beta r}{\tau f}$, $f$ is frequency, and $\tau$ is travel time. For large values of $Q$, the approximation $Q = \dfrac{\pi}{d}$ is valid.

Let us define the attenuation factor $\alpha$ as

$$\alpha = \frac{2\pi}{Q} \qquad (4)$$

Value $\alpha$ varies between 0 and 1.

For a model of viscoelastic media with complex stiffness tensor, Carcione (1995) defined the formula $\dfrac{2\pi}{Q} = \dfrac{\text{Im}[V^2]}{\text{Re}[V^2]}$ where $V$ is the complex velocity, which was used by Chichinina et al. (2006a, 2006b). This definition is valid only for large $Q$ values. In the general case, following the definition of $Q$ (Equation 2), it must be

$$\alpha = \frac{\text{Im}[V^2]}{|V|^2} \qquad (5)$$

For anisotropic media with attenuation, from (5), by following Chichinina et al. (2006b), one can describe a dependence of the attenuation factor on a wave-ray travel (incidence) angle $\theta$, and on a source-receiver azimuth $\phi$ by the approximate formula:

$$\alpha \approx A + B(\phi)\sin^2\theta + C(\phi)\sin^4\theta \qquad (6)$$

where (Chichinina et al., 2006c)

$$B = B_0\cos^2(\phi - \phi_0),$$
$$C = C_0\cos^4(\phi - \phi_0), \qquad (7)$$

$A$, $B_0$, $C_0$, are constants, provided $B_0 > 0$ for HTI media (Chichinina et al., 2004, 2006c), and $\phi_0$ is the symmetry axis angle, usually unknown, which has to be estimated.

The incidence angle $\theta$ has a sense of the angle between axis $z$ and the wave ray in the anisotropic medium with attenuation. The approximation was made under the assumption of a small value of $\sin^6\theta$, which practically means: $\sin^2\theta < 0.36$, or $\theta < 37º$ .

## Numerical methods for estimating the symmetry axis angle

One can compute the value $\alpha$ in the target anisotropic layer with attenuation from seismograms of P-waves reflected from the top and the bottom of this layer (see next section). Usually, the data used are 3D seismic data from spaced receivers and sources within nodes of a rectangle grid at the surface. The symmetry axis angle is usually obtained for a square surrounding a node of the grid (for a bin), by using seismic traces which Common Middle Point (CMP) is within this bin. If such traces are few, then neighbor bins are combined into a superbin, and calculations are made for it. Therefore, a preliminary stage of the estimation is a selection and an extraction of seismic traces of the superbin from the 3D data.

All methods described below are applied to the individual superbin. Let the superbin have $n$ traces ($i = 1,..., n$) with incidence angles $\theta_i$ in the target layer and azimuthal angles $\phi_i$.

The first two methods use also sectoring; i.e., the traces of the superbin are sorted into $m$ azimuthally equal sectors ($j = 1,..., m$), with $k_j$ traces in each sector, with incidence angles $\theta_k$ ($k = 1,..., k_j$) in the target layer. It is adopted that all traces in the individual sector $j$ have the same value of azimuth $\phi_j$, equal to the middle azimuth of the sector.

## Approximate method of sectors (ASM)

It is the most computationally simple method based on the idea by Mallik *et al*. (1998) for the AVOA. From (6) one can write for the sector $j$:

$$\alpha_{jk} = A_j + B_j \sin^2 \theta_k + C_j \sin^4 \theta_k \qquad (8)$$

where $\alpha_{jk}$ is the value of $\alpha$ calculated from the trace $k$ in the sector $j$.

Having $\alpha_{jk}$ and $\theta_k$ for all $k$ in the sector $j$ ($k_j \geq 3$), one can calculate $A_j$, $B_j$, and $C_j$ from (8) by the least-squares method (e.g., Sabinin & Chichinina, 2008). These calculations have to be made for all sectors.

The unknown value $\phi_0$ may be obtained from the first of equations (7) written for each sector $j$:

$$B_j = B_0 \cos^2(\phi_j - \phi_0), j = 1,...,m \qquad (9)$$

As a rule, $B_j$ is calculated with errors incorporated by the least-squares method from the data. Equation (9) is valid only for precise, theoretical values of $B_j$, and reasonably can be replaced by another. Let $B_j = B_j^{(p)} + \delta_j$, where $B_j^{(p)}$ is the precise value, and $\delta_j$ is an error. Then equation (9) can be replaced by the following approximate equation, which is proved to be more convenient for calculations:

$$B_j = a + b\cos[2(\phi_j - \phi_0)], j = 1,...,m \quad (10)$$

If the error $\delta_j$ is not large, then $a$ and $b$ must be close to each other for an HTI medium ($a \approx b$), although generally saying $a \neq b$.

System (10) has three unknowns ($a$, $b$, and $\phi_0$), therefore $m$ should be at least 3 for obtaining a solution. It is the same system as in the AVOA technique by Sabinin & Chichinina (2008). System (10) is solved by the least-squares method, and has two solutions (two $\phi_0$ differing by $\pi/2$ with the same $b$ but of opposite sign). The condition $b > 0$ may be used to distinguish symmetry-axis and fracture-strike directions (see Equation 7).

## Method of sectors (SM)

It differs from ASM by the method of solving the azimuthal problem (9). Instead of the approximate equation (10), equation (9) is written in its precise form:

$$B_j = b\xi_j, j = 1,...,m \qquad (11)$$

where $\xi_j = \cos^2(\phi_j - \phi_0)$

This simplification leads to a more complicated solution. Let us consider the functional of error

$$F = \tfrac{1}{m}\sum_{j=1}^{m}(b\xi_j - B_j)^2 \qquad (12)$$

Functional $F$ must be minimized over parameters $b$ and $\phi_0$. For this, it is necessary to solve the system of two equations:

$$\partial F / \partial b = 0, \quad \partial F / \partial \phi_0 = 0. \qquad (13)$$

Transformation of (13) gives the following non-linear equation for obtaining $\phi_0$:

$$AD - BC = 0 \qquad (14)$$

where $A = \tfrac{1}{m}\sum_{j=1}^{m}\xi_j^2$, $B = \tfrac{1}{m}\sum_{j=1}^{m}y_j\xi_j$, $C = \tfrac{1}{m}\sum_{j=1}^{m}\xi_j B_j$,

$D = \tfrac{1}{m}\sum_{j=1}^{m}y_j B_j$, and $y_j = \sin[2(\phi_j - \phi_0)]$ .

Additionally, $b = C / A$

Equation (14) is trigonometric non-linear and is solved by the method of half-dividing. It usually has more than one solution for $\phi_0$. From these solutions, one chooses the one that gives the minimum for the functional (12). This choosing can be erroneous for highly noised data.

**Approximate truncate method (ATM)**

This method is similar to Jenner (2002) for the AVOA. The sectoring is not needed. Equation (6) is truncated for simplicity, and it is combined with (10), as in ASM. It gives after transformation:

$$\alpha_i = a + b\sin^2\theta_i + d\sin^2\theta_i \cos[2(\phi_i - \phi_0)]$$

(15)

where $\alpha_i$ is the value $\alpha$ calculated from the trace $i$ of the superbin.

If we define $s_i = \sin^2\theta_i$, $S = \sin(2\phi_0)$, $C = \cos(2\phi_0)$, $g_i = \cos(2\phi_i)$, and $h_i = \sin(2\phi_i)$, then equation (15) can be rewritten into a more convenient form as:

$$\alpha_i = a + bs_i + dCs_ig_i + dSs_ih_i$$

(16)

The values $s_i$, $g_i$, and $h_i$ are known because they can be calculated from the headers of the seismograms and the parameters of the medium.

Let us consider the functional of error

$$F = \frac{1}{n}\sum_{i=1}^{n}(a + bs_i + dCs_ig_i + dSs_ih_i - \alpha_i)^2 .$$

Functional $F$ must be minimized over parameters $a$, $b$, $d$, and $\phi_0$. For this, it is necessary to solve the system of four equations:

$$\partial F / \partial a = 0, \quad \partial F / \partial b = 0,$$
$$\partial F / \partial d = 0, \quad \partial F / \partial \phi_0 = 0.$$

(17)

The solution of system (17) gives the equation for obtaining the parameter $\phi_0$:

$$\tan(2\phi_0) \equiv \frac{S}{C} = \frac{A_2H_1 - A_1H_2}{A_2H_2 - B_1H_1}$$

(18)

where $A_1 = a_1b_1 - a_2^2$, $B_1 = a_1c_1 - a_3^2$,

$A_2 = a_1b_2 - a_2a_3$, $H_1 = F_2a_1 - F_1a_2$,

$H_2 = F_3a_1 - F_1a_3$, $a_1 = B - A^2$, $b_1 = I - D^2$,

$c_1 = J - E^2$, $a_2 = G - AD$, $b_2 = K - ED$,

$a_3 = H - AE$, $F_1 = f_1 - Af_0$, $F_2 = f_2 - Df_0$,

$$F_3 = f_3 - Ef_0, \quad A = \frac{1}{n}\sum_{i=1}^{n}s_i, \quad B = \frac{1}{n}\sum_{i=1}^{n}s_i^2,$$

$$D = \frac{1}{n}\sum_{i=1}^{n}g_is_i, \quad E = \frac{1}{n}\sum_{i=1}^{n}h_is_i, \quad G = \frac{1}{n}\sum_{i=1}^{n}g_is_i^2,$$

$$H = \frac{1}{n}\sum_{i=1}^{n}h_is_i^2, \quad I = \frac{1}{n}\sum_{i=1}^{n}g_i^2s_i^2, \quad J = \frac{1}{n}\sum_{i=1}^{n}h_i^2s_i^2,$$

$$K = \frac{1}{n}\sum_{i=1}^{n}g_ih_is_i^2, \quad f_0 = \frac{1}{n}\sum_{i=1}^{n}\alpha_i, \quad f_1 = \frac{1}{n}\sum_{i=1}^{n}s_i\alpha_i,$$

$$f_2 = \frac{1}{n}\sum_{i=1}^{n}g_is_i\alpha_i, \quad f_3 = \frac{1}{n}\sum_{i=1}^{n}h_is_i\alpha_i,$$

The other parameters are:
$$d = \frac{A_2H_1 - A_1H_2}{S(A_2^2 - A_1B_1)}, b = (F_1 - dCa_2 - dSa_3) / a_1$$
and $a = f_0 - bA - dCD - dSE$

From (18), one can see that the solution $\phi_0$ has a period of $\frac{\pi}{2}$. This value of the period means that we must use an additional condition for understanding which value of $\phi_0$ is the symmetry-axis azimuth. Application of the method has shown that the condition $b > 0$, as by analogy with ASM, fails sometimes.

**Truncate method (TM)**

This method differs from ATM by using equation (11) instead of (10). It leads to the following equation for superbin instead of (15):

$$\alpha_i = a + bs_i\xi_i$$

(19)

where $\xi_i = \cos^2(\phi_i - \phi_0)$.

In order to solve (19) by the least-squares method, let us consider the functional of error

$$F = \frac{1}{n}\sum_{i=1}^{n}(a + bs_i\xi_i - \alpha_i)^2$$

(20)

Functional $F$ must be minimized over parameters $a$, $b$, and $\phi_0$. For this purpose, it is necessary to solve the system of three equations:

$$\partial F / \partial a = 0, \quad \partial F / \partial b = 0, \quad \partial F / \partial \phi_0 = 0.$$

(21)

Transformation of (21) gives the non-linear equation for obtaining $\phi_0$:

$$CA_1 + DB_1 - F_2C_1 = 0$$

(22)

where $A_1 = AF_1 - BF_0$, $B_1 = AF_0 - F_1$,

$$C_1 = A^2 - B, \quad A = \tfrac{1}{n}\sum_{i=1}^{n} s_i \xi_i, \quad B = \tfrac{1}{n}\sum_{i=1}^{n} (s_i \xi_i)^2,$$

$$C = \tfrac{1}{n}\sum_{i=1}^{n} s_i y_i, \quad D = \tfrac{1}{n}\sum_{i=1}^{n} s_i^2 y_i \xi_i, \quad F_0 = \tfrac{1}{n}\sum_{i=1}^{n} \alpha_i,$$

$$F_1 = \tfrac{1}{n}\sum_{i=1}^{n} \xi_i s_i \alpha_i, \quad F_2 = \tfrac{1}{n}\sum_{i=1}^{n} y_i s_i \alpha_i, \text{ and}$$

$$y_i = \sin[2(\phi_i - \phi_0)]$$

Additionally, $b = B_1 / C_1$, and $a = A_1 / C_1$

Equation (22) is trigonometric non-linear and it is solved by the method of half-dividing. It usually has more than one solution for $\phi_0$. From these solutions, one chooses the one that yields the minimum for the functional (20).

## General method (GM)

This method differs from TM by using the full form of equation (6). One can write instead of (19):

$$\alpha_i = a + b s_i \xi_i + c s_i^2 \xi_i^2 \qquad (23)$$

Let us consider the functional of error

$$F = \tfrac{1}{n}\sum_{i=1}^{n} [a + b s_i \xi_i + c s_i^2 \xi_i^2 - \alpha_i]^2 \qquad (24)$$

Functional $F$ must be minimized over parameters $a$, $b$, $c$, and $\phi_0$. For this, it is necessary to solve the system of four equations:

$$\partial F / \partial a = 0, \quad \partial F / \partial b = 0,$$
$$\partial F / \partial c = 0, \quad \partial F / \partial \phi_0 = 0. \qquad (25)$$

Three first equations of the system (25) give expressions for the parameters $a$, $b$, and $c$:

$$c = \frac{a_2 f_1 - a_1 f_2}{a_2^2 - a_1 a_3}, \quad b = \frac{f_1 - c a_2}{a_1},$$
$$a = F_0 - cB - bA \qquad (26)$$

where $a_1 = A^2 - B$, $a_2 = AB - C$, $a_3 = B^2 - D$,

$$f_1 = AF_0 - F_1, \quad f_2 = BF_0 - F_2, \quad A = \tfrac{1}{n}\sum_{i=1}^{n} s_i \xi_i,$$

$$B = \tfrac{1}{n}\sum_{i=1}^{n} s_i^2 \xi_i^2, \quad C = \tfrac{1}{n}\sum_{i=1}^{n} s_i^3 \xi_i^3, \quad D = \tfrac{1}{n}\sum_{i=1}^{n} s_i^4 \xi_i^4,$$

$$F_0 = \tfrac{1}{n}\sum_{i=1}^{n} \alpha_i, \quad F_1 = \tfrac{1}{n}\sum_{i=1}^{n} s_i \xi_i \alpha_i, \text{ and}$$

$$F_2 = \tfrac{1}{n}\sum_{i=1}^{n} s_i^2 \xi_i^2 \alpha_i.$$

The fourth equation of (25) can be transformed into a non-linear equation for obtaining $\phi_0$:

$$b(aG + bH - E_0)$$
$$+2c(aH + cK - E_1) + 3bcL = 0 \qquad (27)$$

where $G = \tfrac{1}{n}\sum_{i=1}^{n} y_i s_i, \quad H = \tfrac{1}{n}\sum_{i=1}^{n} y_i s_i^2 \xi_i,$

$$L = \tfrac{1}{n}\sum_{i=1}^{n} y_i s_i^3 \xi_i^2, \quad K = \tfrac{1}{n}\sum_{i=1}^{n} y_i s_i^4 \xi_i^3,$$

$$E_0 = \tfrac{1}{n}\sum_{i=1}^{n} y_i s_i \alpha_i, \quad E_1 = \tfrac{1}{n}\sum_{i=1}^{n} y_i s_i^2 \xi_i \alpha_i, \text{ and}$$

$$y_i = \sin[2(\phi_i - \phi_0)].$$

The system (26) – (27) is solved by the method of half-dividing. Similar to SM and TM, the system usually has more than one solution for $\phi_0$. One must choose the one that gives the minimum for the functional (24). The condition $b > 0$ is used to choose the symmetry-axis direction.

## Estimation of the attenuation factor

A correct estimation of the attenuation factor $\alpha$ from seismograms is very important for the proposed QVOA techniques. There are some good methods of estimating $\alpha$ (or quality factor $Q$), see Introduction. Here, it is suggested a methodology adapted to surface data of reflection.

The Frequency Shift Method (FS) by Quan & Harris (1997) was chosen here because it operates with integral values and hence is less sensitive to noise and gives values of $\alpha$ close to the classical Spectral Ratio Method (e.g., Tonn, 1991).

The ratio of spectral amplitudes of waves reflected from the bottom and from the top of the target layer with attenuation (see Figure 1) can be expressed from equations (1) and (3) as (e.g., Jannsen *et al.*, 1985)

$$S(f) \equiv \frac{A_b}{A_t} = R(f) \exp(-d\tau f) \qquad (28)$$

where $A_t$ and $A_b$ are amplitudes of spectra of reflected waves from top and bottom of the target layer, respectively, $R(f)$ is a coefficient that combines reflectivity set and geometrical spreading, and $\tau$ is the travel time of the ray inside the target layer.

With the assumption of weak dependency of $R$ with frequency $f$, equation (28) can be rewritten in the form:
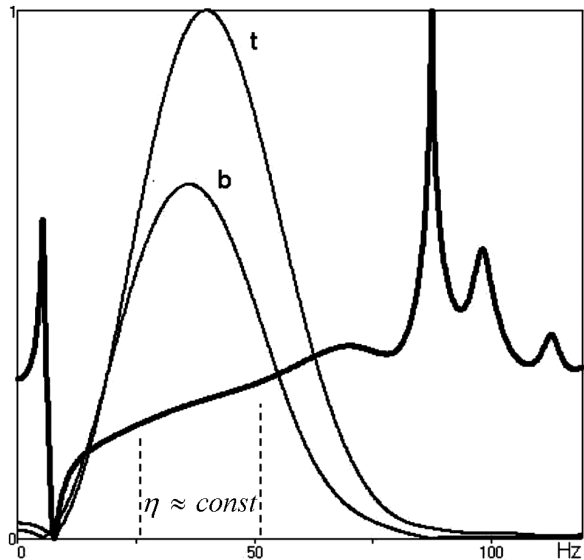
**Figure 1.** Spectra of the reflected waves from top (t) and bottom (b) of the target layer, and a logarithm of its ratio (thick line), in normalized units.

$$\ln S = -\eta f + \eta_0 \qquad (29)$$

where $\eta = d\tau$.

Following Quan & Harris (1997), the coefficient $\eta$ of equation (29) is calculated by the algorithm:

$$a_i = \sum_f A_i, \quad f_i = \frac{1}{a_i} \sum_f f A_i, \quad i = t, b,$$

$$\sigma_t^2 = \frac{1}{a_t} \sum_f (f - f_t)^2 A_t, \quad \eta = \frac{f_t - f_b}{\sigma_t^2}$$

where sums are taken over an interval of frequencies where $\eta$ is nearly constant (see Figure 1).

Value $\alpha$ is calculated via equations (3) and (4), where $d = \eta/\tau$.

Data with noise can introduce significant error in estimating $\alpha$ values. For more ability of QVOA techniques, only values with $\bar{\alpha} - 0.2 < \alpha < \bar{\alpha} + 0.2$, where $\bar{\alpha}$ is the arithmetic mean value of $\alpha$ over traces, are taken into consideration by the techniques.

For applying the FS method, it is necessary to choose a window for the impulse in the time domain, and a window (interval) in the spectral domain. If the seismic source generates a Ricker wavelet, I would choose the time window including three central phases of the impulse. For real data, if it is difficult to determine the three phases of the

impulse because of noise, then one can chose an impulse of less number of phases. Then I would compose a wave with much more samples than the impulse truncated by this window, by adding zeros after the impulse. Typically for seismic problems, the window has near 300 samples, and the composed wave has 16384 samples. Then I would make the Fast Fourier transform of this wave to obtain the spectrum. The more samples the better spectrum.

Also, as it was noticed by Dasgupta & Clark (1998) for real data whose amplitudes (and spectra) are deformed by the normal moveout (NMO) correction, it is necessary to restore the data to its pre-NMO form.

The spectra of the impulse usually have the shape of a bell. The spectral interval should be chosen there where a plot of the logarithm of spectral ratio $\ln S$ (see Figure 1) has a part with linear behavior ($\eta \approx const$), and near the peak of the spectra in order to decrease errors in calculations. By observing spectra of impulses from many synthetic seismograms, it was found that the spectral interval between the peak frequency of the top spectrum (t) and 0.8 of the peak frequency of the bottom spectrum (b) is quite satisfactory. For making the position of interval more precise, one can use an adaptive procedure of the best fitting to the linear part of $\ln S$ with the least-square method.

An important value in the calculation of $\alpha$ is the travel time $\tau$ of the ray inside the target layer. It is greater than the difference in time between reflected impulses at the same trace, $\Delta t$.

A system of non-linear equations can be derived by the tracing method for calculating $\tau$ in a multilayered reservoir (Sabinin, 2012). It allows to obtain the difference between $\Delta t$ and $\tau$, and also the incidence angle $\theta$, and the refraction point $x$ shown in Figure 2.
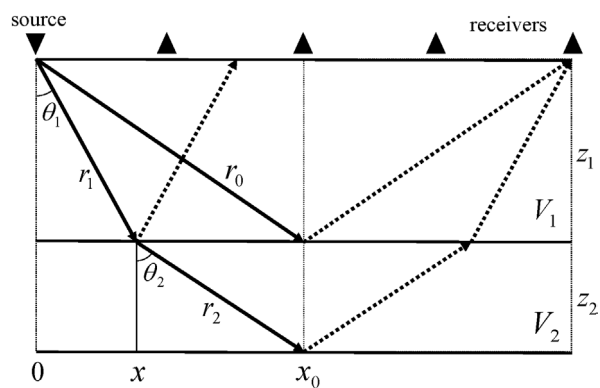


**Figure 2.** Scheme of P-wave reflections in two upper layers of a three-layer medium (the second layer is target).
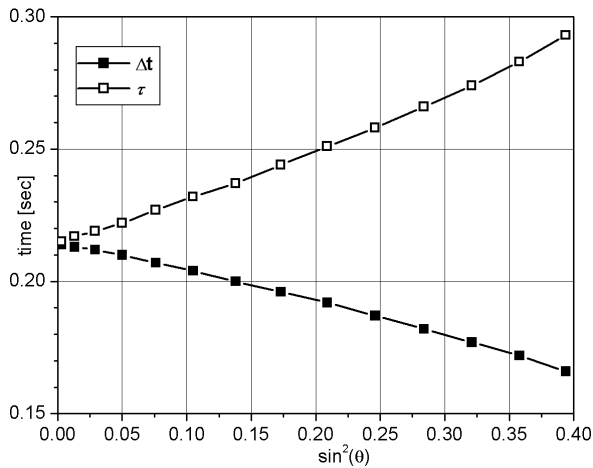
**Figure 3.** Example of calculating incidence angle $\theta$, travel time $\tau$, and $\Delta t$.

Alternative methods were developed by Behura & Tsvankin (2009), Shekar & Tsvankin (2011), Reine *et al.* (2012).

The difference between $\Delta t$ and $\tau$ can be seen in Figure 3. It increases significantly with incidence angle or offset.

As can be seen in Figure 2, one should use the wave reflected from the point $x$ at the top of the target layer to calculate the spectral amplitude $A_t$ (Reine *et al.*, 2012; Sabinin, 2012). This reflected wave can arrive at the surface between receivers. Knowing the value of $x$, one may obtain this wave (or its spectrum) by interpolation from waves (or spectra) of adjacent traces, taking into account different values of geometrical spreading.

**Example of aplication of the techniques**

The techniques are compared in ability to give the most precise value of symmetry axis angle $\phi_0$ for HTI medium. At present, reliable field methods of obtaining $\phi_0$ do not exist. Therefore, I generated synthetic seismograms by applying the technique by Sabinin (2012) of 2D viscoelastic modeling. A three-layer area was constructed with an anisotropic viscoelastic layer in the middle. I set $\phi_0 = 60°$, and derived models for $\phi_j = 0°$, 30°, 45°, 75°, 90° by rotating the stiffness tensor for the anisotropic layer.

The stiffness tensor for HTI medium (e.g., Chichinina *et al.*, 2006b) was rotated by 60° to obtain the model for $\phi_j = 0°$, by 30° for $\phi_j = 30°$, 90° and by 15° for $\phi_j = 45°$, 75°. Anisotropic parameters $\Delta_N = 0.35$, and $\Delta_T = 0.2$ were used in the stiffness tensor.

The attenuation was assumed isotropic in the anisotropic layer, and values of relaxation times

were chosen to obtain the factor $Q$ near 60. Host rock velocities $V_P$ in three layers from surface were given the values 3200, 4000, and 4800 $m/s$, $V_S$ were twice less than $V_P$; densities were the same for the three layers, and thicknesses of the first two layers from surface were 1590 and 410 m.

A source of explosion type generated one Ricker impulse of frequency 45 *Hz.* Receivers were spaced over every 200 m beginning from the position of the source, and measured the $z$-component of velocity.

For data being quasi-real, I added a random Gauss normal (white) noise to the synthetic seismograms generated. Maximum amplitude of the noise was chosen as 10% of the maximum amplitude of the impulse reflected from the top boundary of the target middle layer in the first trace.

In Figure 4, the seismogram for azimuth 0º is presented. As one may see, the amplitude of noise reached up to 50% of the wave amplitude in the middle traces, and up to 100% in far traces.

In Table 1, the symmetry axis angles calculated with the proposed numerical methods are compared. The methods were applied both, to traces smoothed by splines of third order and to non-smoothed (natural) traces.

For noisy data, the result of estimating $\phi_0$ depends on the choice of time windows. The results in Table 1 are obtained with an automatic choice of time windows by a hyperbolic dependence on offset with the initial window set manually. This manual setting was varied up to 10% of the time window.

The results presented in Table 1 are for the best choice of some smart attempts of defining the time windows at the traces. The maximum difference between the estimated $\phi_0$ and the correct value of 60º in these attempts, characterizes a sensitivity of the method to the window choice. The approximate values of the sensitivity for smoothed traces are also presented in Table 1.

**Table 1.** Values of $\phi_0$ calculated by different methods.

| Method | Smoothed | Natural | Sensitivity * |
|--------|----------|---------|---------------|
| ASM    | 62.7     | 56.7    | 15%           |
| SM     | 64.1     | 57.6    | 20%           |
| ATM    | 57.1     | 57.8    | 20%           |
| TM     | 64.1     | 64.6    | 15%           |
| GM     | 59.6     | 61.0    | 3%            |

* Sensitivity values are for smoothed traces
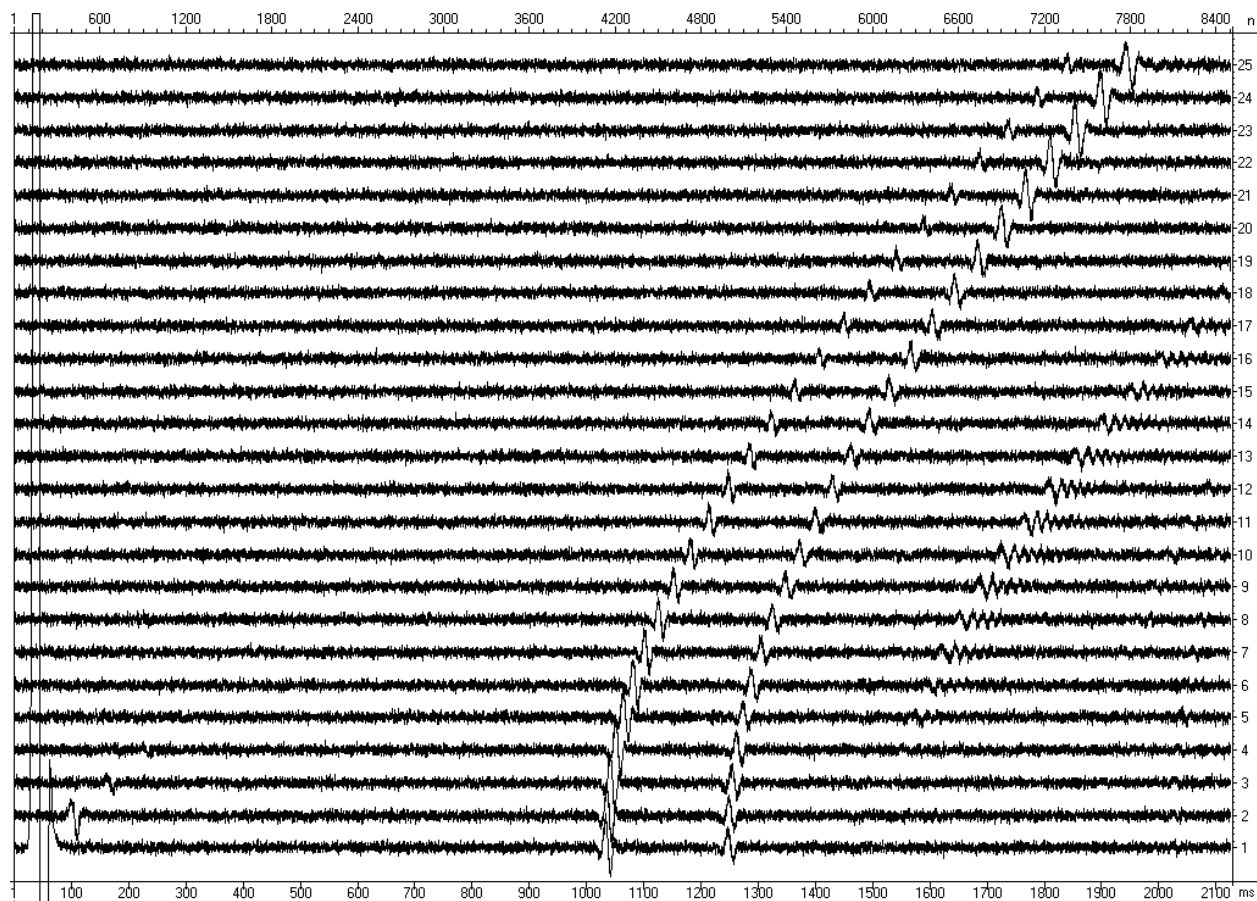
**Figure 4.** Synthetic seismogram with added 10% noise. The $x$ axis is time in ms; the $y$ axis is the number of the trace, each receiver is spaced 200 m. Zero time represents the origin time of the source.

## Discussion and conclusion

The results in Table 1 show superior quality of the General method (GM). It gives stable non-sensitive values with small error. This may be explained by the synthetic nature of the data.

The other methods give good results too, but with a large sensitivity to the choice of time window. For example, 20% for ATM and SM means that one may obtain the value of $\phi_0$ with error up to ±12º (0.2x60º).

Smoothing impulses seems to be useful for reducing sensitivity. Smoothing spectra also improves the results.

In synthetic data without noise, all techniques give nearly precise results with low sensitivity.

One can strongly conclude from results for GM that the third term of the approximation in Equation (6) is important when considering synthetic data.

In applying to real field data, the methods can give other results because of other structure of noise.

In real data, the role of the third (squared) term of approximation (6) can become small or wrong. Therefore, the precision of non-truncated methods may be reduced.

The least-squares method used in the techniques gives the better solution, the operating with more traces. Therefore, the methods of sectors (ASM, SM) should give worse results than the others because they operate with much less traces: coarsely $k_j \approx n/m$.

It should also be noted that SM and ASM are constructed for sectored data and must really on having an additional error because of the need to set a unique value of azimuth for all traces in a sector. This error must be less by decreasing the width of the sector. It must also depend on disposition of the traces inside the sectors.

The maximum value of this error can be easily estimated. For example, let the width of the sector be equal to 10º, and all traces in the sector in the example of previous section be disposed not at the middle azimuth, as above, but at the border of the sector; i.e. at $\phi_j$=5º, 35º, 50º, 80º, 95º. This case will consequently correspond to $\phi_0$=65º, and to an error of 5º in $\phi_0$.

All suggested methods are not ideal and can be non-reliable in real data. The methods GM, TM, and SM demand the solution of non-linear equations and further choosing one solution from many. This choosing may fail in real data. Contrary, the methods ASM and ATM give only one pair of solutions but use approximate equation (10) instead of (9).

The criterion $B_0 > 0$ for distinguishing the pair of symmetry axis and fracture strike directions, see (7), may unexpectedly fail in real data, too.

The logarithm of spectral ratio may not have the straight linear part near the peaks of the spectra, even in smoothed real data, and therefore the proposed algorithm of setting spectral windows may lead to wrong values of $\alpha$.

The smoothing by splines is also not the best solution for improving real data.

In such conditions of problems with real data, the best strategy in fracture-reservoir characterization is to apply all these methods together and check if the results obtained with different methods are close to each other. The more methods, the better forecasting.

Here, we discussed some common problems of QVOA techniques. A more careful investigation of the techniques in synthetic data needs to be done in more complicated experiments. The investigation of different methods of smoothing is also interesting. This is a deal of future publications.

Numerical experiments with real data must not use $\phi_0$, but other parameters for a comparison of the techniques, because of the correct value $\phi_0$ is not known in field data. Such work is beyond the scope of the present publication, and might be hold yet.

Here, the numerical techniques for estimation of fracture directions by applying theory of QVOA analysis were suggested. One of them (GM) is proved good in synthetic data with noise.

## Acknowledgement

## Bibliography

Behura J., Tsvankin I., 2009, Estimation of interval anisotropic attenuation from reflection data, *Geophysics*, 74, 6, A69-A74.

Carcione J.M., 1995, Constitutive model and wave equations for linear, viscoelastic, anisotropic media, *Geophysics*, 60, 2, 537-548.

Chichinina T., Sabinin V., Ronquillo-Jarillo G., 2004, P-wave attenuation anisotropy in fracture characterization: numerical modeling for reflection data: 74th Annual International Meeting, SEG, *Expanded Abstracts*, 143–146.

Chichinina T., Sabinin V. Ronquillo-Jarillo G., 2005, QVOA analysis as an instrument for fracture characterization: SEG 75th Annual International Meeting, paper ANI2.2, p.127-130.

Chichinina T.I., Sabinin V.I., Ronquillo-Jarillo G., Obolentseva I.R., 2006a, Azimuthal QVO analysis applied to oil and gas exploration, *Russian Geology and Geophysics*, 47, 2, p. 265-283.

Chichinina T., Sabinin V., Ronquillo-Jarillo G., 2006b, QVOA analysis: P-wave attenuation anisotropy for fracture characterization, Geophysics, 71, 3, C37-C48.

Chichinina T., Sabinin V., Ronquillo-Jarillo G., 2006c, QVOA method or Q-anisotropy for fracture-reservoir characterization. EAGE 68th Conference & Exhibition – Vienna, Austria, 12-15 June 2006. P147.

Clark R.A., Carter A.J., Nevill P.C., Benson P.M., 2001, Attenuation measurements from surface seismic data: azimuthal variation and time–lapse case studies: 63rd Meeting, European Association Exploration Geophysicists, *Extended Abstracts*, paper L28.

Dasgupta R., Clark R.A., 1998, Estimation of Q from surface seismic reflection data. *Geophysics*, 63, 2120-2128.

Dasios A., Astin T.R., McCann C., 2001, Compressional-wave Q estimation from full-waveform sonic data, *Geophysical Prospecting*, 49, 353-373.

Futterman W.I., 1962, Dispersive body waves: *J. Geophys. Res.*, 67, 5279-5291.

Jannsen D., Voss J., Theilen F., 1985, Comparison of methods to determine Q in shallow marine sediments from vertical reflection seismograms, *Geophysical Prospecting*, 33, 479-497.

Jenner E., 2002, Azimuthal AVO: Methodology and data examples, The Leading Edge, 21, 8, 782-786.

Mallik S., Craft K.L., Meister L.J., Chambers R.E., 1998, Determination of the principal directions of azimuthal anisotropy from P-wave seismic data: *Geophysics*, 63, 692-706.

Quan Y., Harris J.M., 1997, Seismic attenuation tomography using the frequency shift method, *Geophysics*, 62, 3, 895-905.

Reine C., Clark R., van der Baan M., 2012, Robust prestack Q-determination using surface seismic data: Part 1 – Method and synthetic examples, *Geophysics*, 77, 1, R45-R56.

Rüger A., 1998, Variation of P-wave reflectivity with offset and azimuth in anisotropic media: *Geophysics*, 63, 935-947.

Sabinin V., 2012, Viscoelastic modeling and factor Q for reflection data. *Geofisica Internacional*, 51, 4, 377-391.

Sabinin V., Chichinina T., 2008, AVOA technique for fracture characterization: resolving ambiguity, *Geofisica Internacional*, 47, 1, p.3-11.

Shekar B., Tsvankin I., 2011, Estimation of shear-wave interval attenuation from mode-converted data, *Geophysics*, 76, 6, D11-D19.

Sheriff R.E., 2002, Encyclopedic dictionary of exploration geophysics, SEG, 4th ed., 429 p.

Tonn R., 1991, The determination of the seismic quality factor Q from VSP data: a comparison of different computational methods, *Geophysical Prospecting*, 39, 1-37.

Zhang C., Ulrych T.J., 2002, Estimation of quality factors from CMP records, *Geophysics*, 67, 5, 1542-1547.

Zhu Y., Tsvankin I., 2006, Plane-wave propagation in attenuative transversely isotropic media: *Geophysics*, 71, 2, T17 - T30.

# Spatial and temporal variations of atmospheric aerosol optical thickness in northwestern Mexico

Ricardo M. Llamas[*], Roberto Bonifaz, Mauro Valdés, David Riveros-Rosas and Amando Leyva-Contreras

## Resumen

El propósito de este trabajo fue el estudio de los aerosoles atmosféricos en el Noroeste de México mediante el parámetro conocido como Espesor Óptico del Aerosol (AOT). Este parámetro representa uno de los coeficientes de extinción de la radiación solar y un indicador de partículas suspendidas en la atmósfera. Para la determinación del AOT recurrimos al uso de sensores remotos localizados fuera de la atmósfera. En particular, el Espectrorradiómetro de Imágenes de Media Resolución (MODIS), el cual es capaz de obtener mediciones del AOT atmosférico. La información proporcionada por MODIS debe ser validada antes de considerarse fiable; para esta tarea, se obtuvieron mediciones desde la superficie para establecer una correlación con los datos derivados del sensor remoto. El artículo describe el proceso de validación que fue aplicado a los datos del sensor MODIS en contraste con mediciones obtenidas por uno de los fotómetros de la Red Robótica para medición de Aerosoles (AERONET) ubicado en la ciudad de Hermosillo, Sonora. Adicionalmente, se presenta un análisis temporal basado en el comportamiento de las gráficas del AOT, así como un análisis espacial derivado de la información contenida en los mapas de distribución del AOT.

Palabras clave: AOT, aerosoles, MODIS, AERONET, noroeste de México, análisis temporal, análisis espacial

## Abstract

The purpose of this paper was to study aerosol particles in the Northwestern region of Mexico (NWM) through Aerosol Optical Thickness (AOT) parameter in the atmosphere. This parameter represents one of the extinction coefficients of solar radiation and the rate of suspended particles in the atmosphere. For determination of AOT, we considered the use of remote sensors outside of the atmosphere. In particular, Moderate Resolution Imaging Spectroradiometer (MODIS) which can measure the atmospheric AOT thickness. Data from the MODIS sensor must be validated before they are considered reliable. For this task, we required surface measurements to obtain a correlation with the data acquired with the remote radiometer. The paper describes the validation process performed for data obtained with MODIS through measurements provided by an AErosol RObotic NETwork (AERONET) photometer located in the city of Hermosillo, Sonora, NWM. Additionally, we carried out a temporal analysis based on the behavior of the AOT graphics and spatial analysis supported in maps with sufficient information.

Key words: AOT, Aerosols, MODIS, AERONET, Northwestern Mexico, Temporal analysis, Spatial analysis.

R.M. Llamas[*]
Comisión Nacional para el Conocimiento y Uso de la Biodiversidad (CONABIO)
Av. Liga Periférico-Insurgentes Sur 4903
Col. Parques del Pedregal
Del. Tlapan, 14010
México D.F., México
[*]Corresponding author: rllamas@conabio.gob.mx

R. Bonifaz
M. Valdés
D. Riveros-Rosas
A. Leyva-Contreras
Instituto de Geofísica
Universidad Nacional Autónoma de México
Ciudad Universitaria s/n, 04510
México D.F., México

## Introduction

One of the main factors that interact actively with the energy from the Sun is identified as aerosol particles, which influence the processes of absorption, refraction, and scattering of solar radiation that is present in the atmosphere and that create a dynamic climate on Earth as a result of these interactions (Iqbal, 1983). This information from aerosol monitoring is useful not only for others as part of the study of the atmosphere, but it can also find many applications in research on climate change and air pollution caused by human activities and natural phenomena. Many of these applications lie on identifying optimal areas in the use of alternative and renewable energy, such as that from the Sun (Deepak, 1982) (Gueymard and Wilcox, 2011; Broesamle et al., 2001).

Recent models for estimating solar resource use require parameters such as topography, vegetation, albedo, and optical thickness of aerosols in the atmosphere among other elements (Bosch et al., 2010). The use of ground stations is economically unfeasible for estimating AOT over large territories; thus, the use of satellite images represents a viable option for estimation of several atmospheric and geographic parameters that affect the solar radiation that reaches the Earth's surface (Perez et al., 1997).

AOT is used generally to determine the concentration of atmospheric solid particles; their knowledge is useful in conducting studies and in the analysis of smoke from forest fires (Chia et al., 2007), air quality in urban areas (Grosso et al., 2007), the relationship between AOT and wind speed over the ocean surface (Glantz et al., 2006), the influence of anthropogenic aerosols on climate change (Charlson et al., 1992), as well in numerous validation studies using instruments located on surface (Bai et al., 2008), (Correia and Pires, 2006; Ichoku et al., 2002a; Liang et al., 2006), among others. One of the most interesting applications of the estimation of AOT in the atmosphere comprises estimation of solar radiation on the surface because of the importance that this implies in the planning and design of solar applications for power generation (Gueymard and Wilcox, 2011; Broesamle et al., 2001; Bosch et al., 2010; Perez et al., 1997).

There are several sensors that orbit the Earth for the acquisition of data from numerous natural variables that are utilized for studies of the Earth's surface and for analyzing the dynamics of the atmosphere. In particular, the MODIS radiometer, is set on-board the platforms Terra (launched on 1999) and Aqua (launched on 2002) and offers the possibility of obtaining values related with a large amount of data among 36 spectral bands spanning from visible to infrared spectrum, 0.425–14.235

μm, respectively, providing images with spatial resolution at nadir of 1 km, and at 500 and 250 m (Wolfe et al., 1998). The advantages of MODIS sensor in the study of atmospheric phenomena are very broad and it has specific advantages in the analysis of AOT.

Aerosol data provided by MODIS sensor must be validated by surface-based measurements (Liang et al., 2006). For this task, the photometers from AErosol RObotic NETwork (AERONET) can be used. Using this data is possible to obtain optical thickness values at a particular point while the platform in which MODIS is attached performs its coverage over the same area. In the present study, the validation process is developed for Northwestern Mexico (NWM), where to our knowledge no study of this type has been conducted before. The method used for data acquisition and refinement covers the period from 2001–2003, which was selected according to available information for first years of MODIS sensor on Terra satellite and AERONET data availability in the city of Hermosillo, Sonora. In addition, we present the criteria to determine the extent of the area in which AOT values were processed from satellite images, the parameters for granting the same mapping characteristics, and the extraction of spectral bands for the optical thickness spray on the land surface.

### Data acquisition and pre-processing

*Information source – MODIS*

MODIS aerosol products were downloaded from Atmosphere Archive and Distribution System (LAADS Web) of the National Aeronautical and Space Agency (NASA) Goddard Space Flight Center. The products selected were derived from Terra platform level 2 (MOD04 L2) with spatial resolution of 10 × 10 km at nadir in hierarchical data format (HDF) files, which contain values at three different wavelengths for corrected optical depth land (0.47, 0.55, and 0.66 μm) among 62 science data-set options. Data acquisition was performed in terms of NWM as main covered area in all images through h07v06 and h08v06 tiles. Period between 2001 and 2003 was selected as temporal span. Terra products were selected over Aqua due to data availability, regarding the launching date of each platform. All files were reprojected into Lambert conical conformal projection employing the same cartographic parameters that are commonly established by Mexico's National Institute for Statistics and Geography (INEGI, 2011).

The wavelength selected for validation process with AERONET data was 0.66 μm, broadly to 0.675 μm available from sun photometer measurements and regarded in previous studies

(Bai *et al*., 2008; Ichoku *et al*., 2002b; Remer *et al*., 2002). Then, region of interest (ROI) was delimited to obtain the mean value for all pixels with data inside selected area of 50 × 50 km (5 × 5 pixels). The criteria for choosing polygon size depended on lack of congruence between 1 point over the surface where the photometer is located and the dimensions of one single pixel in the image. Furthermore, it is difficult to imagine suspended particles without vertical and horizontal movements along atmospheric strata; hence, determination of the correct area proportions is an important step prior to post-processing. Thus, different area sizes were tested according to previous attempts (Ichoku *et al*., 2002b) (Figure 1). As (Ichoku *et al*., 2002b) mentioned, the average speed of aerosol particles in lower atmospheric layers is 50 km/h, and this represents a 1-h window for AOT data gathered by AERONET instruments in a 5 x 5 pixels polygon of MOD04L2 product.

The reference pixel for ROI was centered over AERONET site coordinates in the Geological Institute Building supported by the National Autonomous University of Mexico (UNAM) at N 29°05', W 110°58'. Once all of the files were acquired and ROI was set up, all images were stacked to produce time series from which basic statistics (mean and Standard deviation [SD]) were derived.

*Information source – AERONET*

AOT data from AERONET was downloaded from the level 2 dataset, with an eye toward further analysis; besides this level was used to build the C005 algorithm (Remer *et al*., 2006), which build up the last version of MODIS products. Time period for chosen data was matched with MODIS AOT available images between 2001 and 2003. The UNAM-Hermosillo AERONET station archives a good and continuous data series and was selected for the comparison, taking into account its information availability.

AERONET offers AOT values at eight different wavelengths and records between 7 a.m. and 7 p.m. (local time) every 15 min. In this case, the 0.675-µm wavelength was processed because this wavelength depicts closest matching to the 0.66-µm MODIS band. In order to select the dataset from AERONET based on the MODIS pass, a 3-h range was set up to correlate AOT from the previously mentioned sources in an attempt to overcome the scarce availability of 60-min values at level 2 data. Furthermore, previous analysis of all HDF files depicted that all images were retrieved by MODIS from 4:30 to 7:30 p.m. Greenwich Mean Time (GMT). By means of structured query language (SQL) instructions, mean values were acquired in the same period of time for 2001 and 2002; initially, 2003 was considered in the complete validation process, but non-continuous records yielded the recommendation to omit the third year.

***Results***

*MODIS-AERONET Validation Process*

Once all information was processed, it was developed in a table of data availability for the period 2001–2002. Analysis of MODIS and AERONET files showed that the existence of comparable data was very low. This is because both sources have long periods without AERONET data whereas MODIS data is available, and vice versa. At the end, we compared 57 cases (days)
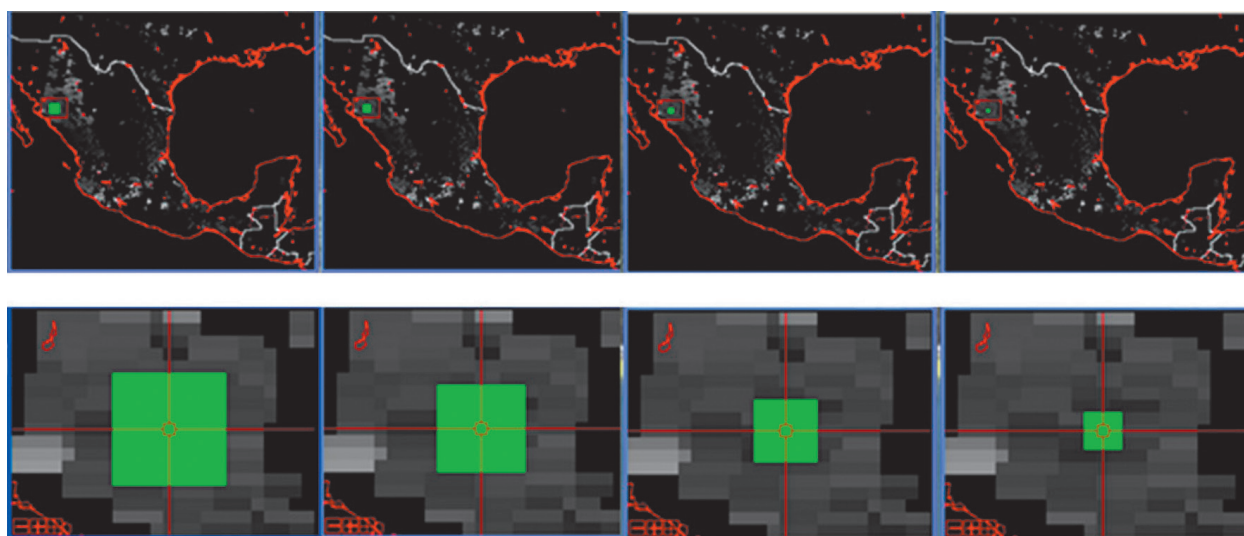


**Figure 1.** Areas tested to determine region of interest.

over the period 2001–2002 in which values from both MODIS and the AERONET photometer exist in Hermosillo, Sonora.

Time series for both sets of values is very similar (Figure 2). When performing linear regression between them (Figure 3), we identified those >2 SD away from values obtained from the regression. These data were removed for analysis. In total, we performed 2 linear regressions and eliminated 7 data representing 12.3% of outliers. Figures 3 and 4 show graphs obtained from linear regression fit and the analysis of waste before and after filtering the data.

The final determination of co-efficient $R^2$ = 0.891 was obtained for a set of 50 data between 2001 and 2002. This result, compared with previous studies, presents a higher correlation on confrontation with a co-efficient of $R^2 = 0.729$

(Ichoku *et al*., 2002b) and was close to results in which the correlation obtained is $R^2 = 0.9245$ (Bai *et al*., 2008). However, we should note that these measurements were obtained from different regions and different datasets from amounts of records with different values; thus, results are employed as parameter of comparison and not for validation of those obtained in this work.

In order to evaluate the correlation between both data series, MODIS and AERONET, we performed the Spearman rank correlation test and the Pearson rank correlation test. For Spearman test we obtain a correlation coefficient of C=0.887 (p < 2e-7, N= 57) and for Pearson test we obtain a correlation coefficient of C=0.834 (p < 8e-16, N= 57). The correlation in both tests is high and the probability of error is low enough to be considered negligible.
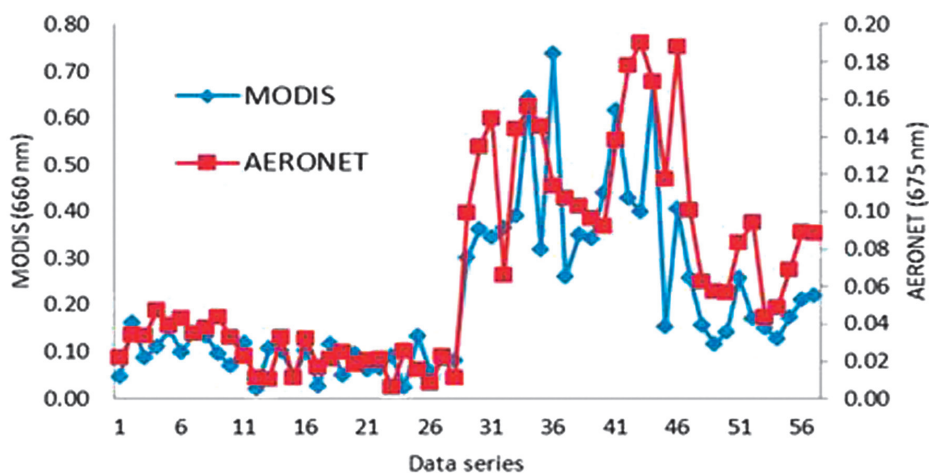


**Figure 2.** Aerosol Optical Thickness (AOT) data series from Moderate Resolution Imaging Spectroradiometer (MODIS) and AErosol RObotic NETwork (AERONET).
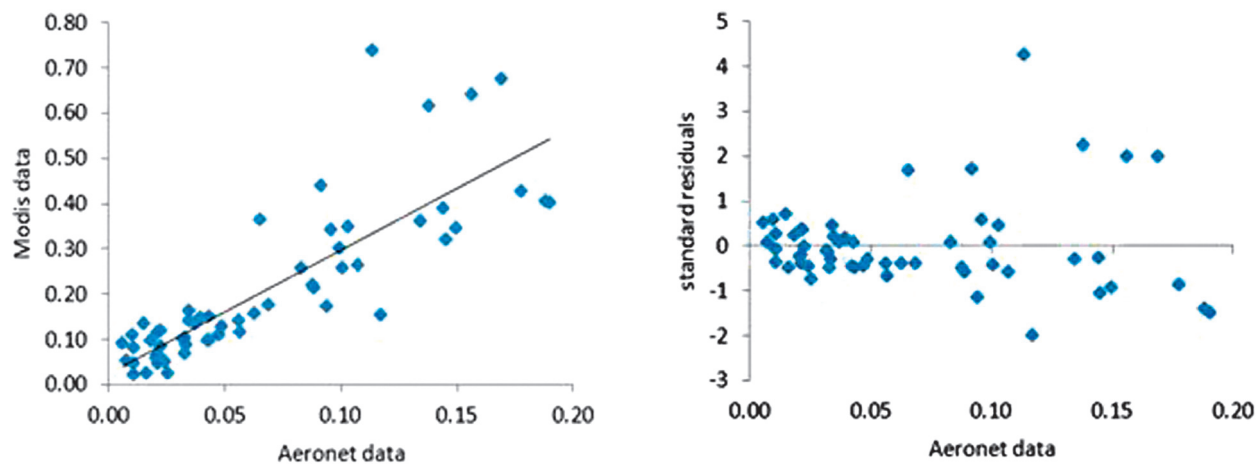


**Figure 3.** Linear regression and residuals analysis for AErosol RObotic NETwork (AERONET) and Moderate Resolution Imaging Spectroradiometer (MODIS) data. Initial data set.
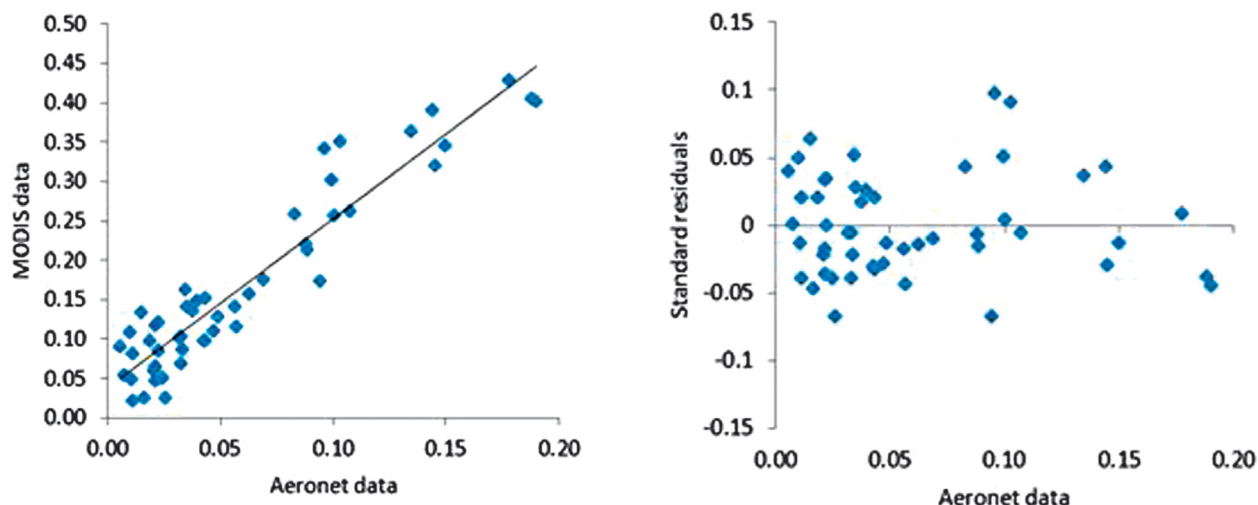
**Figure 4.** Linear regression and residuals analysis for Moderate Resolution Imaging Spectroradiometer (MODIS) and AErosol RObotic NETwork (AERONET) after filtering of data.

Based on data from the MODIS sensor and once we had completed validation with AERONET measurements in the previous section, we were able to consider that MODIS data are suitable for studying not only temporarily optical thickness behavior spray in the city of Hermosillo, Sonora, but, according to the correlation coefficients, MODIS values can be utilized for spatial analysis of the AOT in the entire coverage area of MODIS images corresponding to NWM, even though baseline data were obtained from the state of Sonora.

### Discussion

#### Time Analysis

The graphs presented in this section (Figures 5 and 6) refer to the average behavior of AOT in a ROI of 2,500 km² (5 × 5 pixels) over city of Hermosillo, which were obtained as measurements for validation of MODIS data and do not refer to variations in optical thickness across the NWM. This is due to that for this second case, it would be necessary to perform digital processing of satellite images to obtain the value at different points, although in this study we report a subsequent spatial analysis based on information reflected on final maps.

Comparative analysis of values in the 3-year period attempts to identify patterns in the presence of suspended particles as well to demonstrate if there is seasonality in the measurements explaining AOT behavior. Thus, other factors determine the concentration of aerosols in the atmosphere.

When we observe the behavior of the AOT data of Hermosillo over the polygon set for study period, there are different peaks with values >0.6 in the months of March, May, and June, while the months with the lowest values are December and January; this shows a decrease of optical thickness in the coldest months (Figure 5).

In the case of 2002, the behavior of AOT was depicted despite the limited availability of data. In June 2001 and 2002, there is a maximum AOT value as a result of gradual increase in the first half of the year. After June, a decrease of AOT concentration is observed during the second half of the year. Unlike 2003, AOT values remained relatively low throughout the year; this trend is also suggested with the available data. This suggests a seasonal pattern that advice to verify information for prior years and after ones as well. In addition, there are small peaks in August and September and lonely spots between November and December as well as between January and March.

By interpreting the annual behavior of the AOT during the 3 years (Figures 6 and 7), it is clear that 2001 and 2002 exhibit similar behavior. Figure 7 shows that higher average values correspond to the months of June, with measurements >0.4 units for 2001 and 2002. The lowest values occur in the months of November, December, and January, the same in both cases, indicating an agreement with months with lowest temperatures.

We must take in account that data availability in 2002 (Figure 6) is scarce or non-existent during a few months; thus, in this case, the behavior is deduced by observing the monthly data and
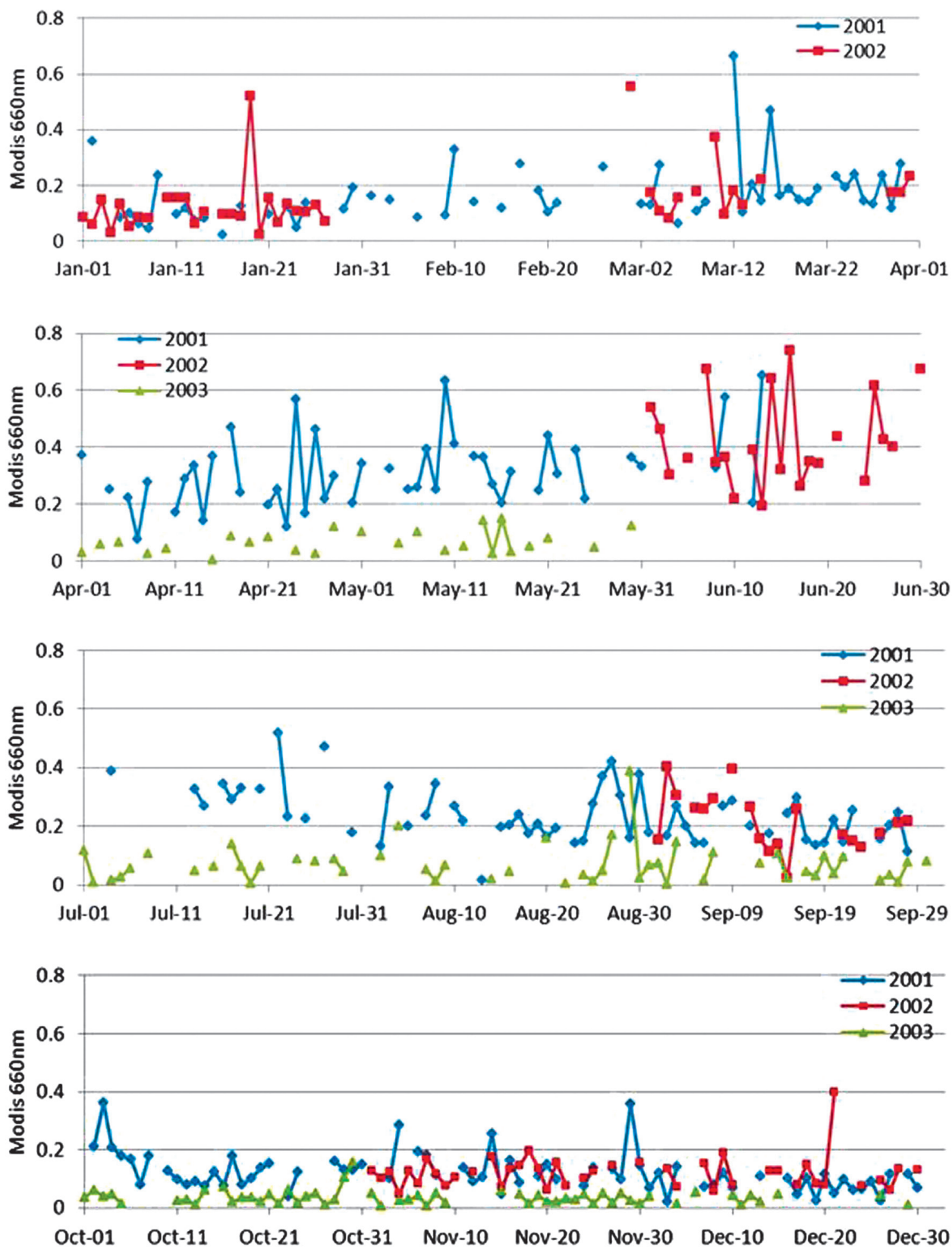
**Figure 5.** Variations in Aerosol optical thickness (AOT) behavior, over 5 x 5 pixels polygon set on Hermosillo, Sonora, for the period comprising January 2001 to December 2003.
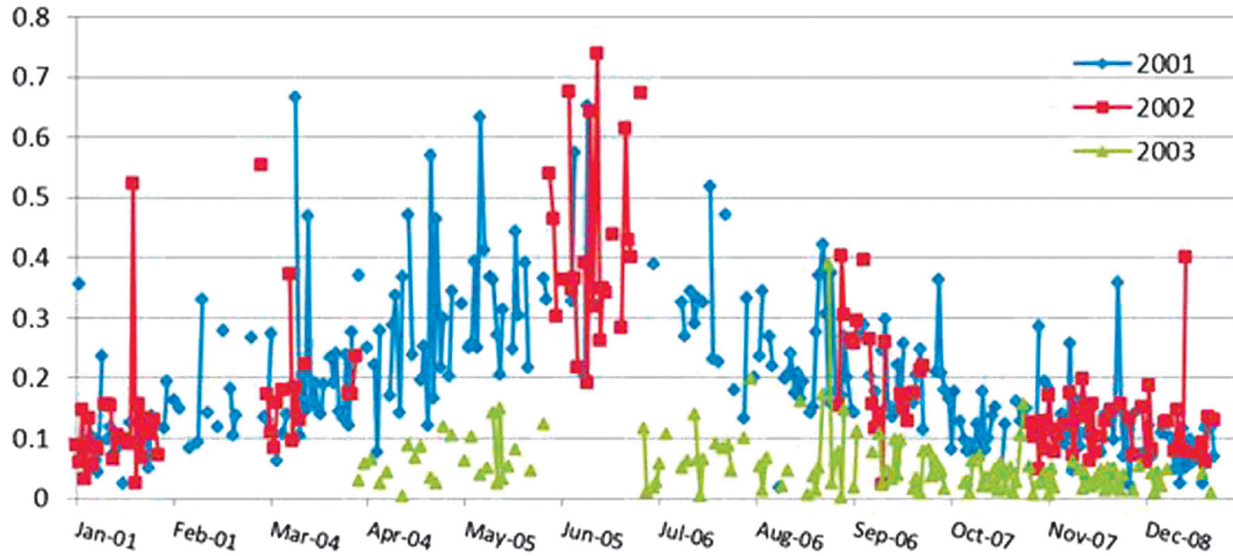
**Figure 6.** Comparative graph of Aerosol optical thickness (AOT) behavior for 2001, 2002, and 2003.
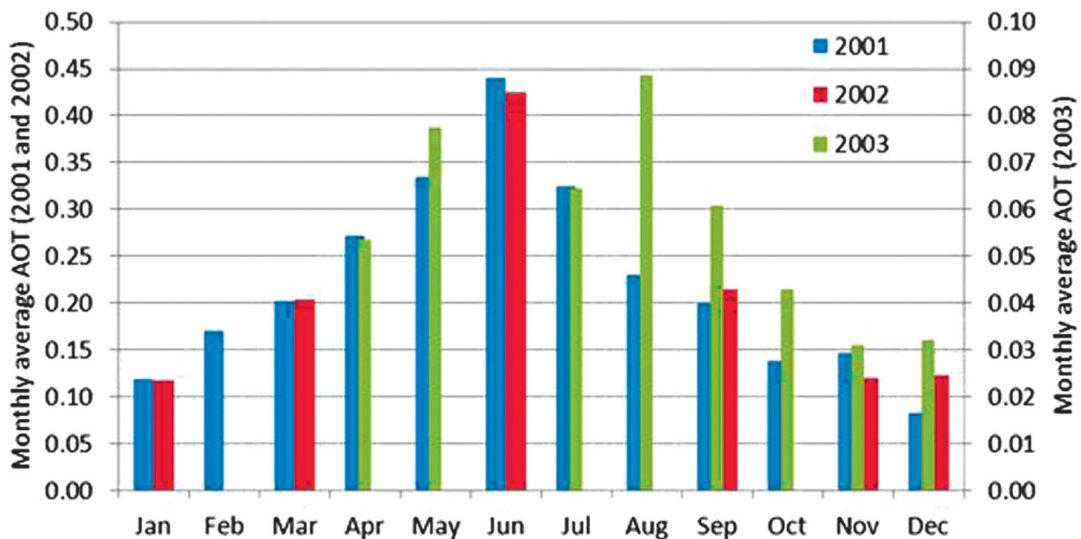


**Figure 7.** Monthly comparison graph of AOT behavior for the years 2001, 2002, and 2003.

analysis in relation to other years in order to infer AOT trends over the year, although analysis of the complete study period must be considered in determining patterns in the particle concentration. In 2003, there are 8 months with available data, excluding the first 3 months of the year and the month of June, which does not allow for clearly analysis of the annual performance of optical thickness. However, available data show that in the months of May through October, there is a gradual increase, and a decrease in AOT values around June. This appears to confirm the seasonal pattern observed in the previous 2 years, although absolute AOT values for the entire year of 2003 are lower than those of previous years.

Finally, to compare AOT behavior during the 3-year period, it is noteworthy that while in the annual charts the cyclical behavior of the concentration of atmospheric particles is not clearly observed, when we considered all data together, there is a clear seasonal pattern of an increase and a decrease in optical thickness values, in which measurements are higher from the second third of the year.

For 2001 and 2002, this was fulfilled by presenting the highest values in March and June with two peaks in their respective charts. However, the year 2003 differs from this behavior and exhibits highest values in August and September,

which would be strange if we take prior years as reference. However, when considering the behavior of the atmosphere along the last year (2003), it is possible to correlate these measurements with the presence of two major cyclonic events that exerted an influence on the region during that year.

According to the U.S. National Hurricane Service (NOAA, 2003a), in 2003, atypical landfall in NWM occurred, the second strongest tropical cyclone of the season: the first, *Ignacio*, became hurricane on August 26 and entered into the Gulf of Baja California with a slow movement that brought heavy rainfall, while the second, *Marty* began to develop on September 10 and peaked on day 22 of the month as a hurricane (NOAA, 2003b).

This may partially explain the high AOT values in these months due to the presence of large numbers of hygroscopic nuclei in large cloud formations due to cyclonic events and to the attenuation of the passage of solar radiation at the Earth's surface as a result of the high concentration of suspended particles (Iqbal, 1983).

It is also notable that during the 3 years, months with the lowest optical-thickness values correspond to December and January 2001 and 2002, while in the case of 2003, the month of December has the lowest values. Despite that there is no data for the January period, the graphical behavior of the 3 years indicates that in each year, the months mentioned show the same characteristics in terms of particle concentration in the atmosphere.

*Spatial Analysis*

Once MODIS data were validated with AERONET sensor data from the city of Hermosillo, MODIS images can be used for data acquisition of optical thickness throughout area covered by sensor snapshots. For the image selection representing the best description of optical depth in NWM, monthly data median was selected from AERONET in order to determine the day that shows most representative AOT distribution in the study area most clearly. Considering that the availability of images is not complete in each month of the 3-year period and that in many cases all values are concentrated at short period of time in the month we found most useful median usage. If we had used mean to get monthly values, those had been representative just of a part of month instead of entire monthly period. However, when we use median, we take into account AOT behavior at the most possible middle of the month. Also, it is known that the mean could be affected by extreme values, while the median is not (Triola, 2008).

In the preparation of maps based on information from the images, variations of the particle concentration of aerosols are shown not only over the area of 2,500-km² plot in the city of Hermosillo, but also in space for the entirety of NWM, in addition to information contained in images taken with the MODIS aerosol-type product to know the origin of the particles in each map. In the images presented in this subsection (Figure 8), we observe the behavior of the optical thickness across the NWM, and by means of image analysis, it is possible to interpret not only the patterns of aerosol-particle concentration, but also the distribution of particle type, mainly in the state of Sonora, which is represented in all of the final maps.

These maps, in conjunction with the correlation work previously performed with photometer measurements of the Hermosillo City AERONET networks, represent valid data for all areas of Mexico and the parts of the U.S. that are represented in the final maps. Furthermore, these maps cover NWM on many days different from those ones which data for validation processing were obtained. Hence, the behavior observed in the previous graphs maintains strict concordance solely with adjacent pixels over Hermosillo instead of each one of covered area in the final maps, although closest pixels show similar trends.

In 2001, through analysis of maps of every month of the year, there is a notorious gradual increase that reaches its peak on July and then gradually decreases until December; additionally, the month of January presents the lowest optical-thickness values for the entire region.

During 2002, although we do not have maps of every month, it is possible to identify a similar pattern of rise and fall as in the previous year, with highest values in June. According to the monthly image, there is an abrupt increase of AOT in relation to the information available for the first half of the year.

In this same year, after the maximum value observed in June is clearly observed a decrease in optical thickness, even with the lack of maps for every month of the second quarter of 2002, the images of September, November, and December clearly illustrate a gradual decrease among each of these, which means that this pattern is consistent with AOT behavior in the months for which no data are available.

In 2003, by interpreting the images, it can be concluded that although there are no maps of the first 3 months of the year, there is an increase in optical-thickness values from April, reaching its highest peak, as in the previous 2 years, between June and July, but in this case by presenting a second increase in August and September.

**Figure 8.** Aerosol optical thickness values along 2001–2003 over NWM, small images show representative months derived from MODIS aerosol-type product.
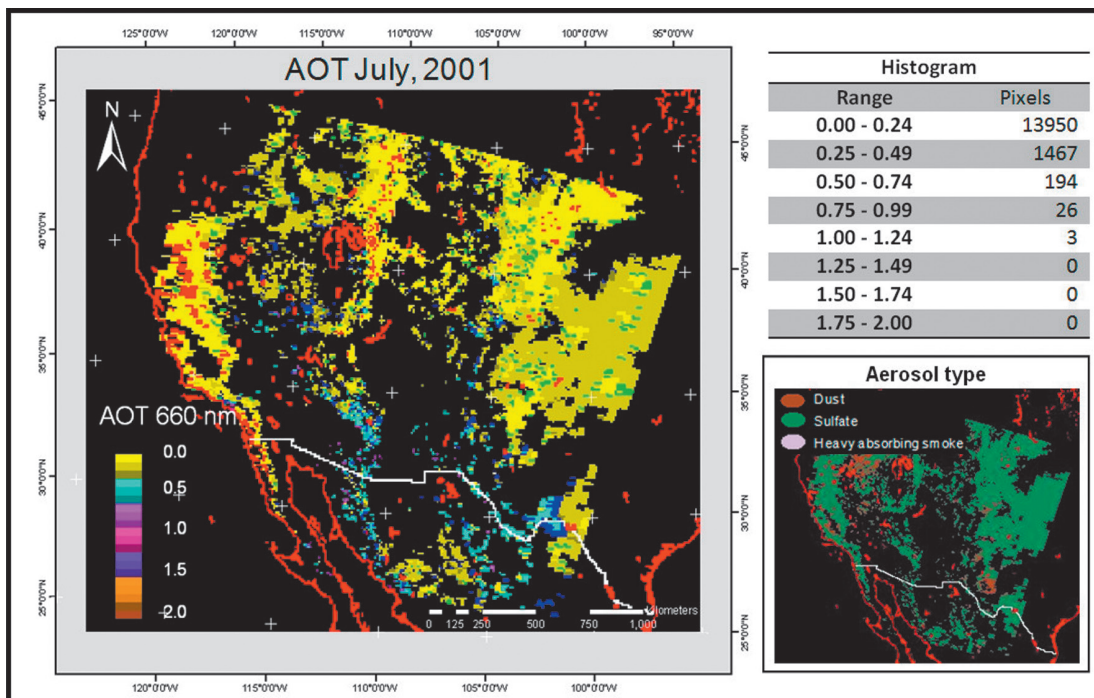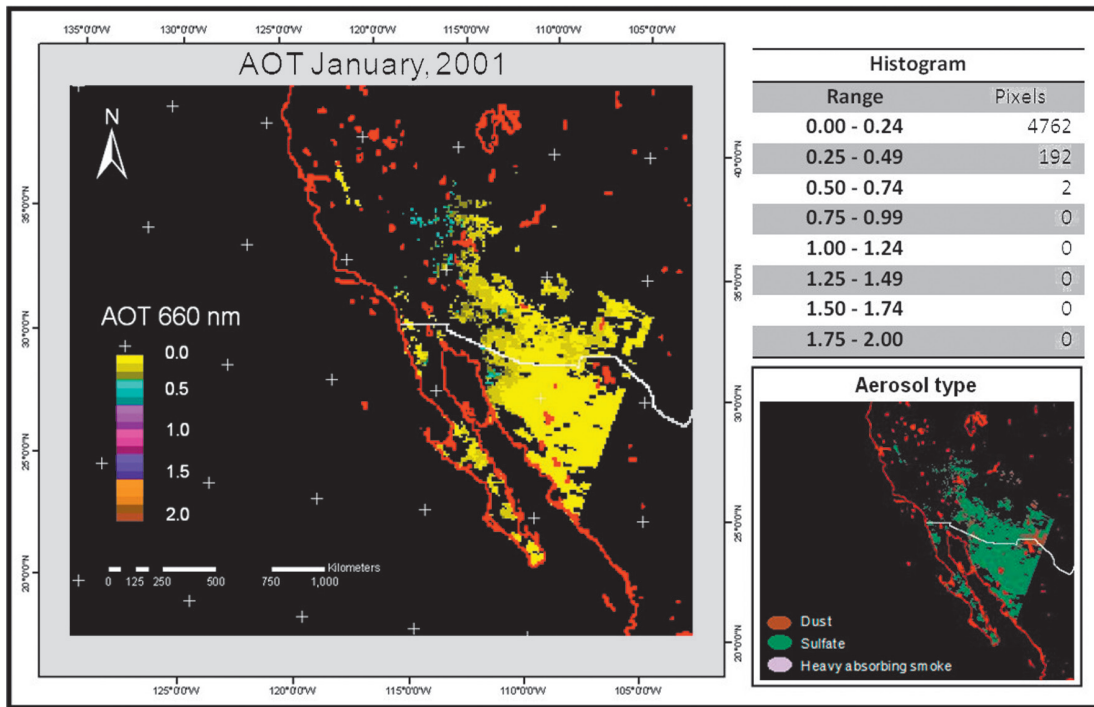
**Figure 8.** Continuation.
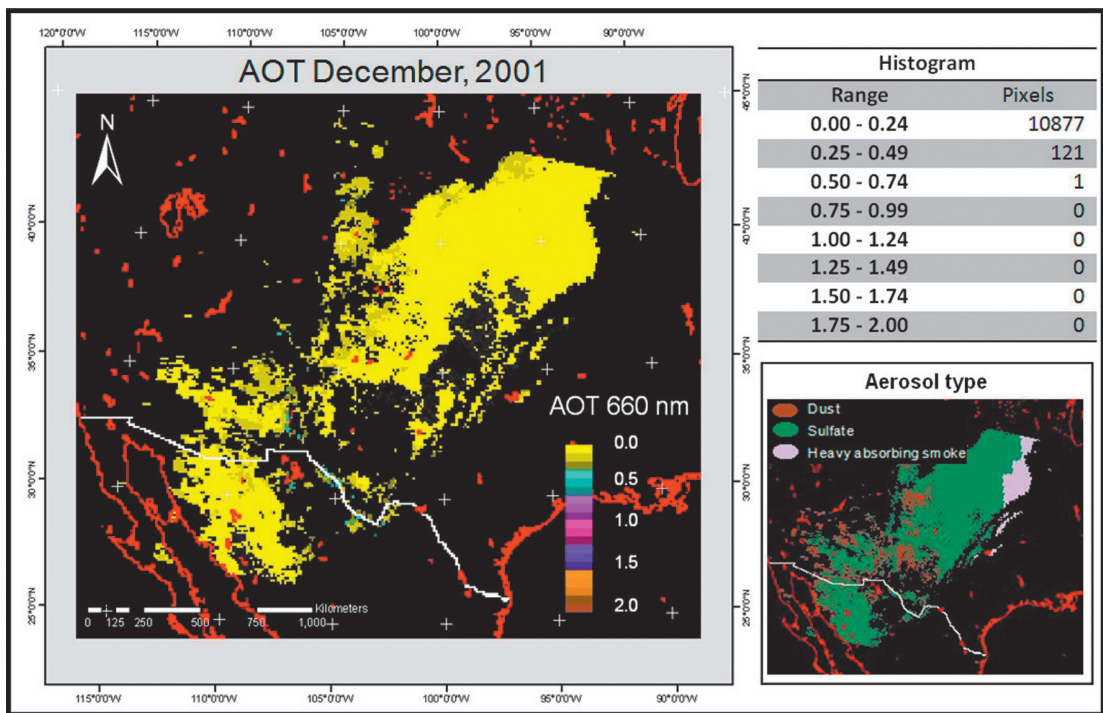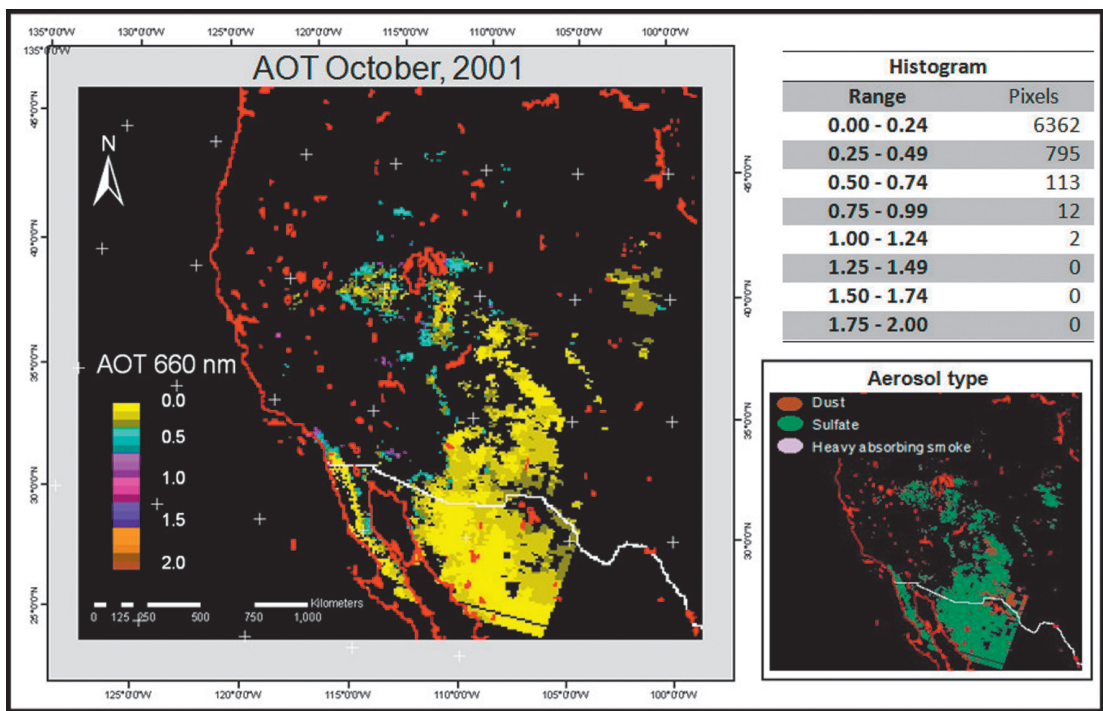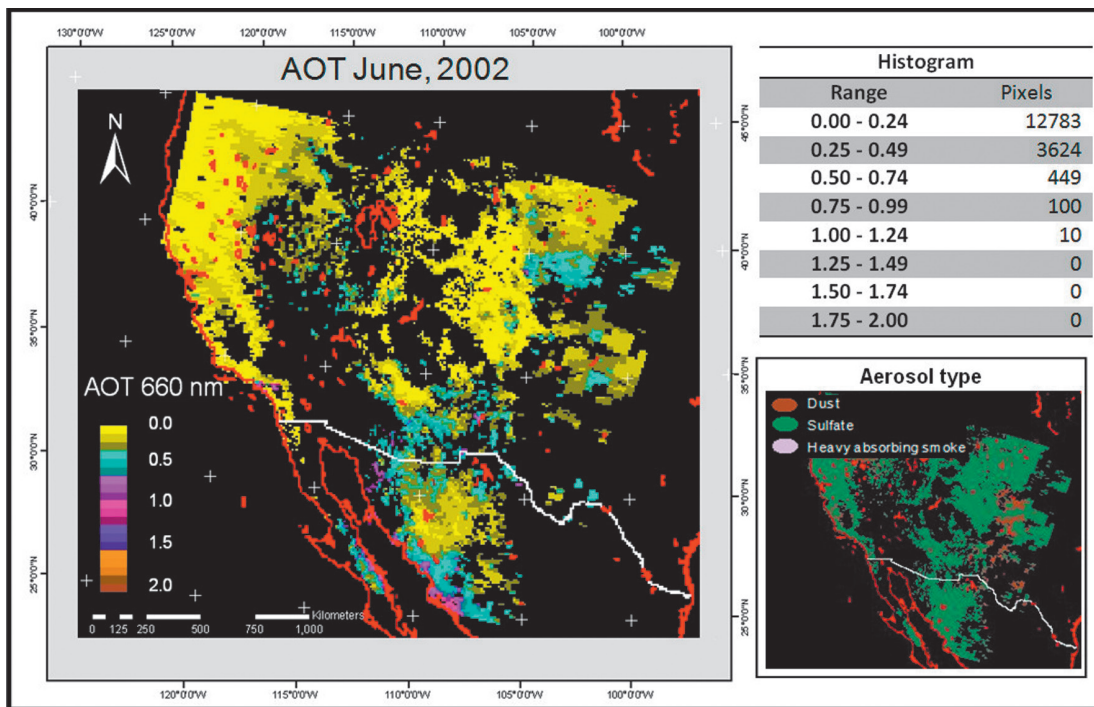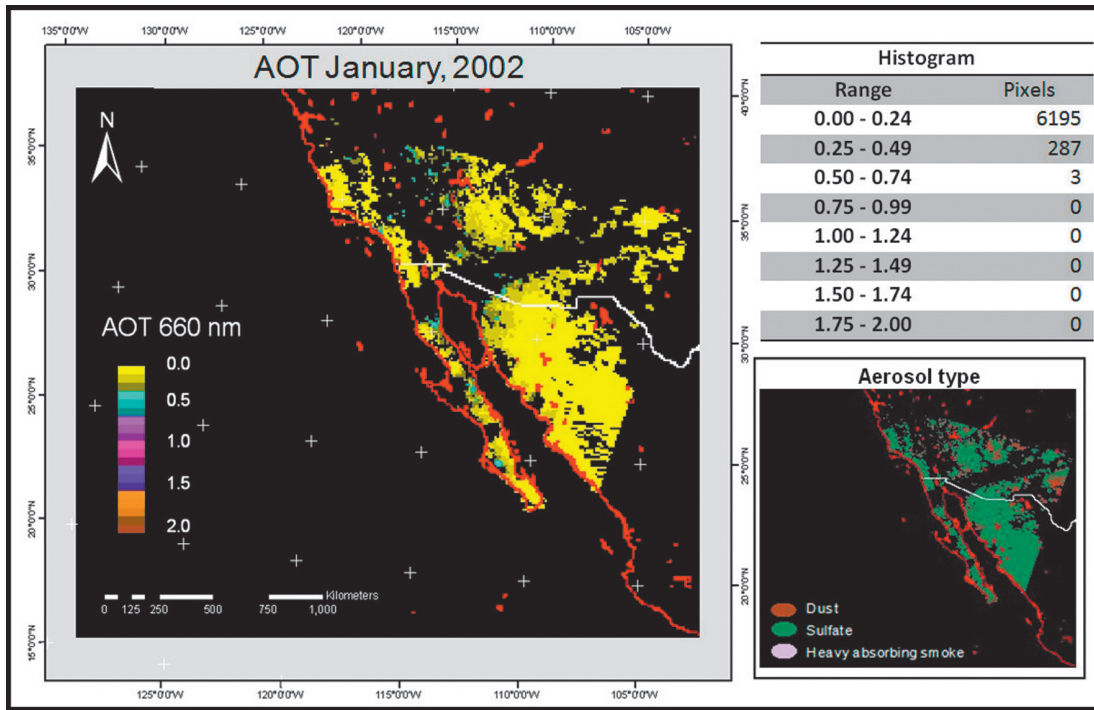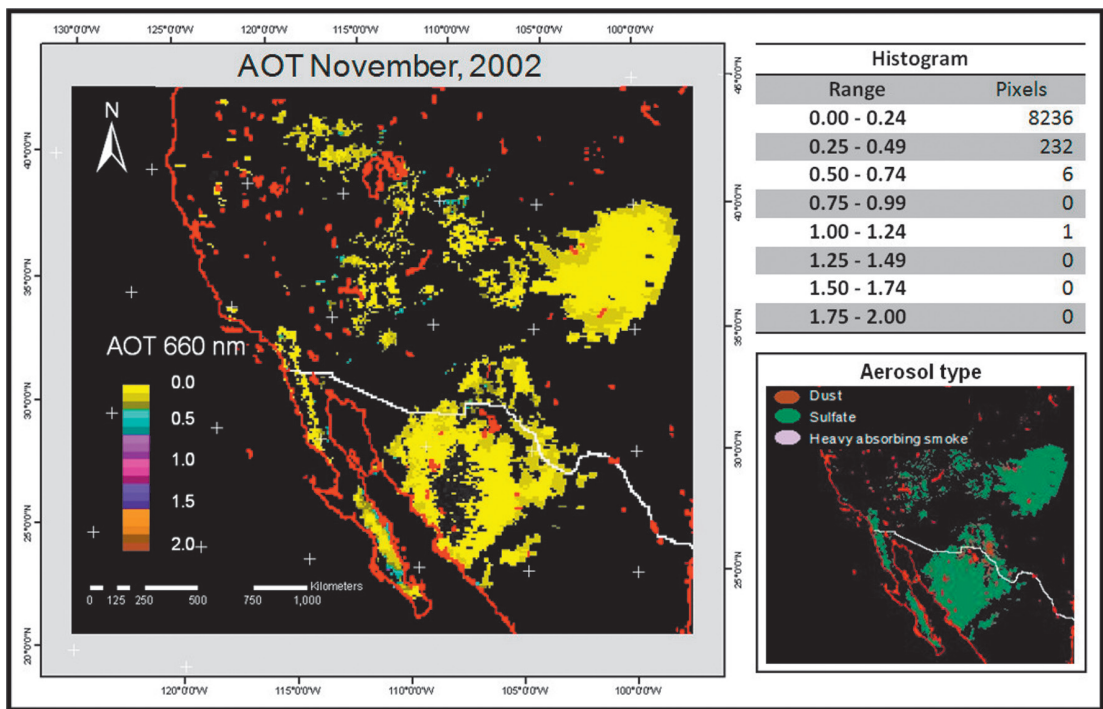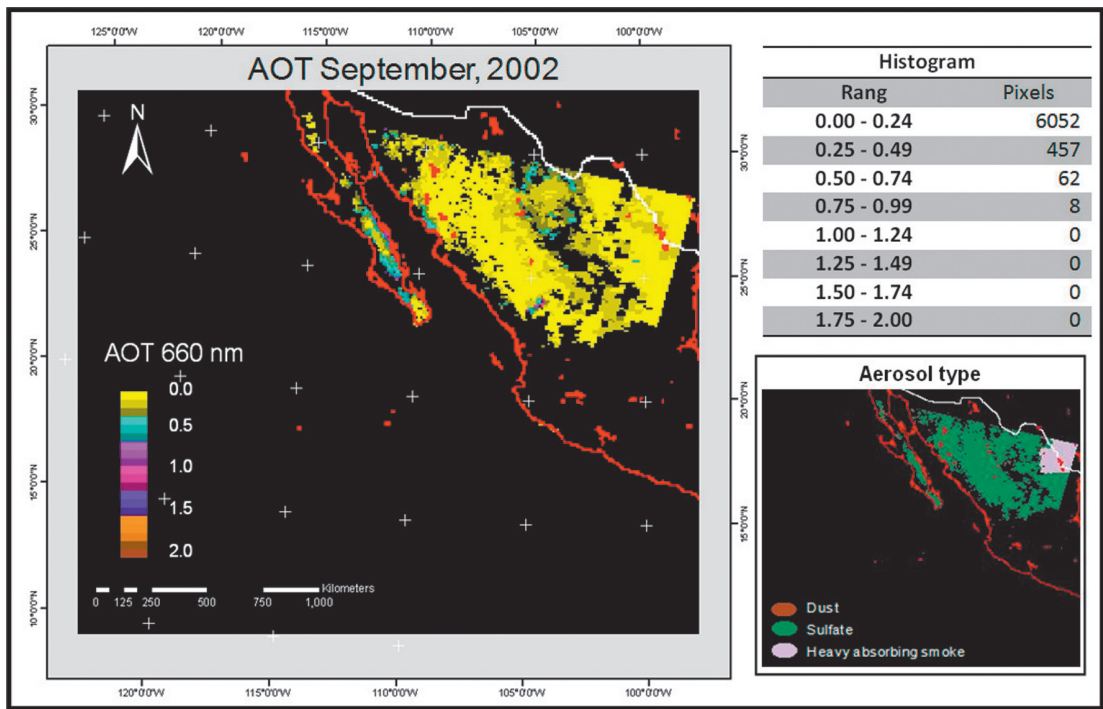
**Figure 8.** Continuation.

**Figure 8.** Continuation.

**Figure 8.** Continuation.
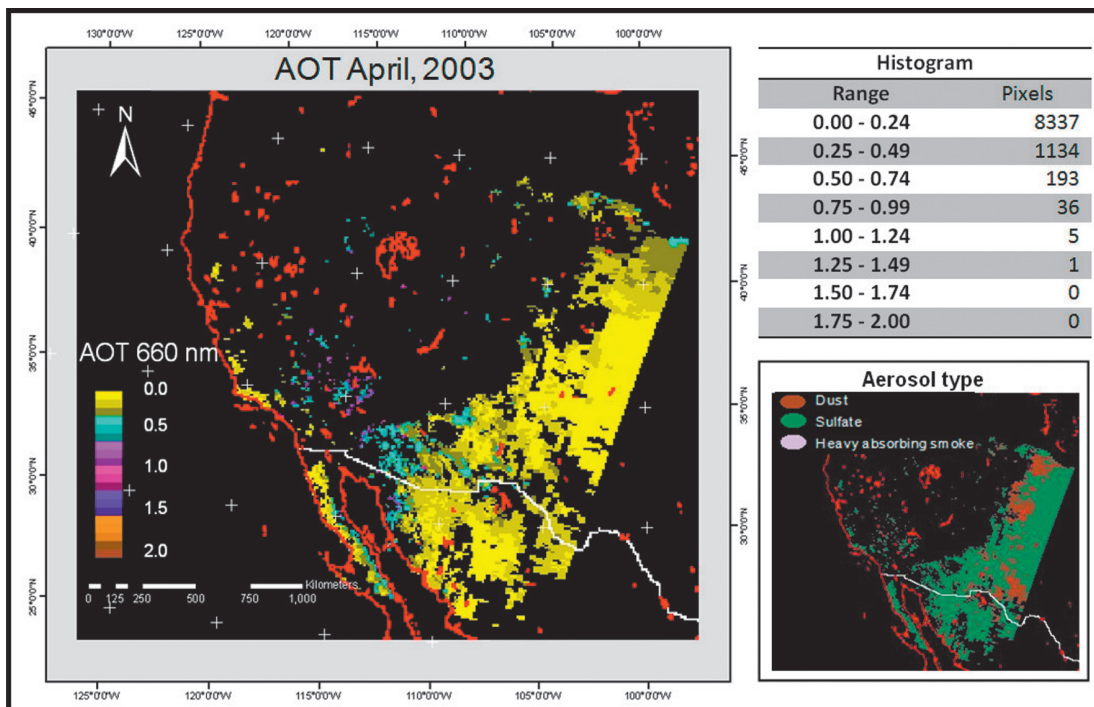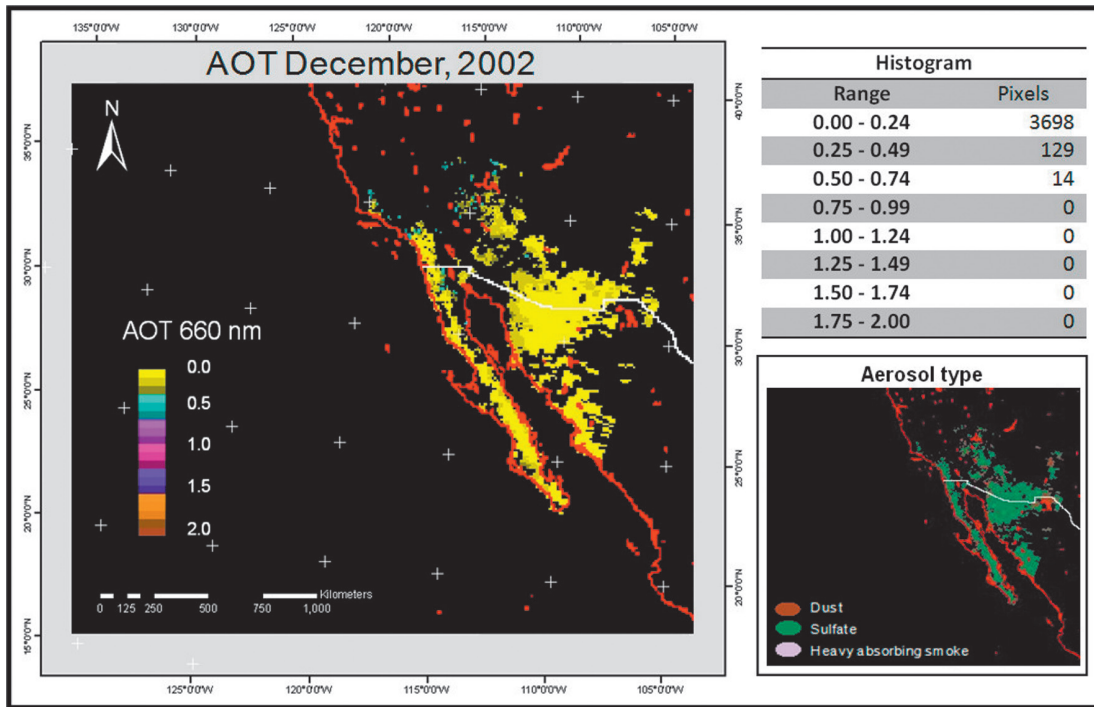
**Figure 8.** Continuation.
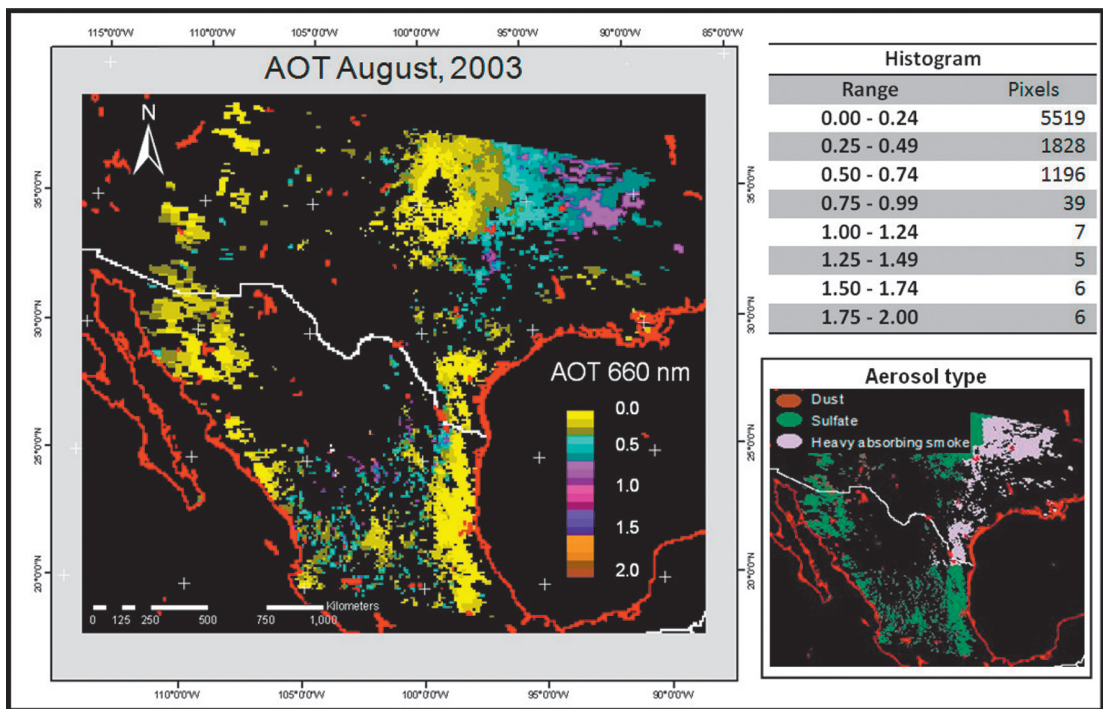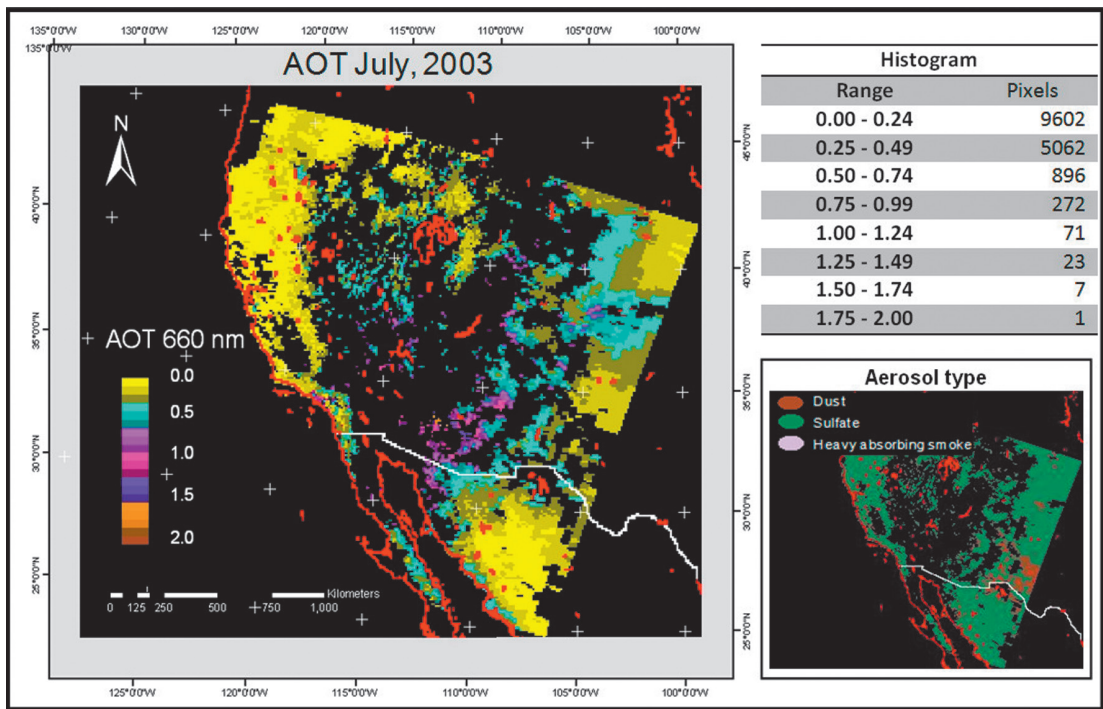
**Figure 8.** Continuation.
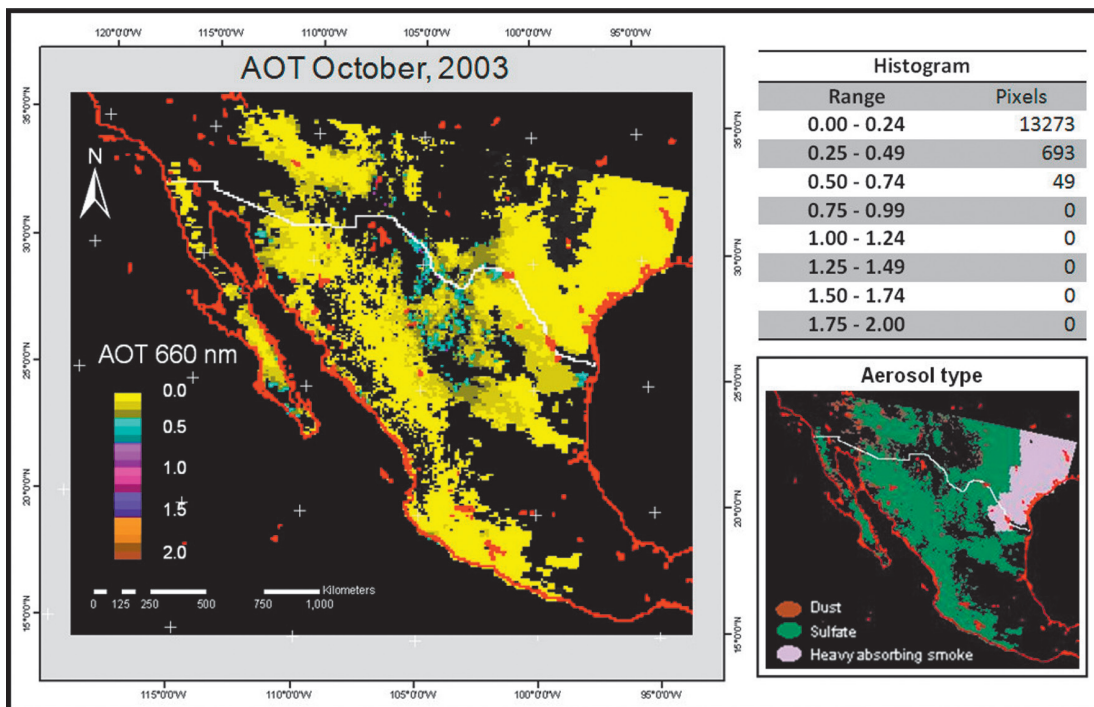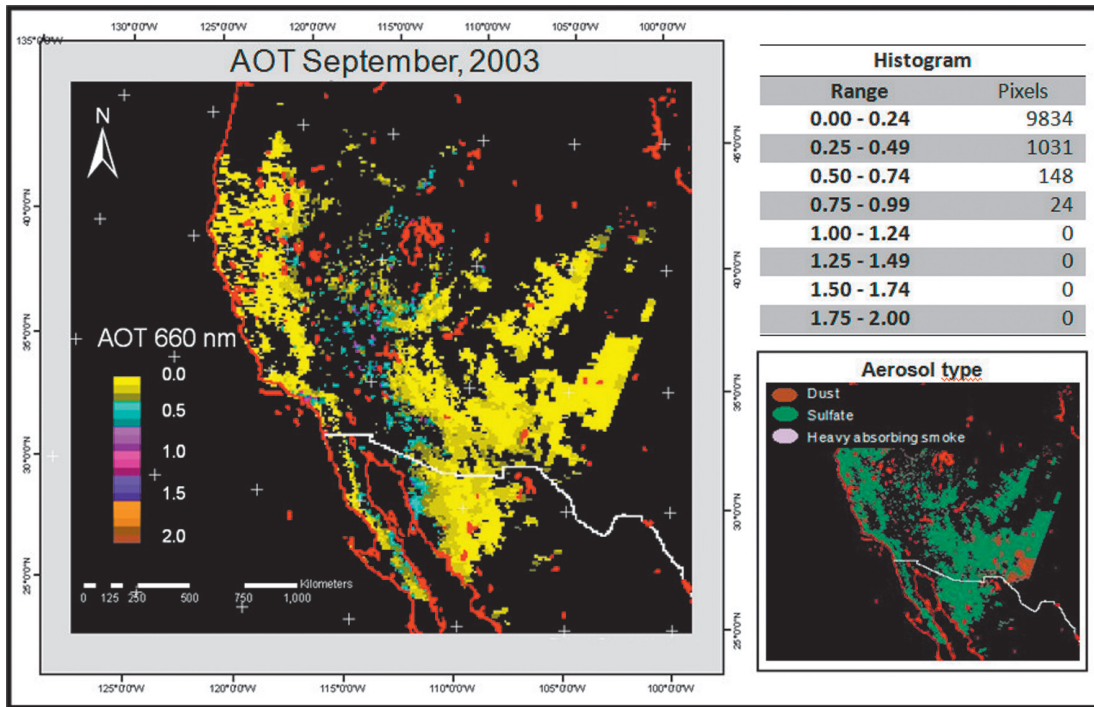
**Figure 8.** Continuation.
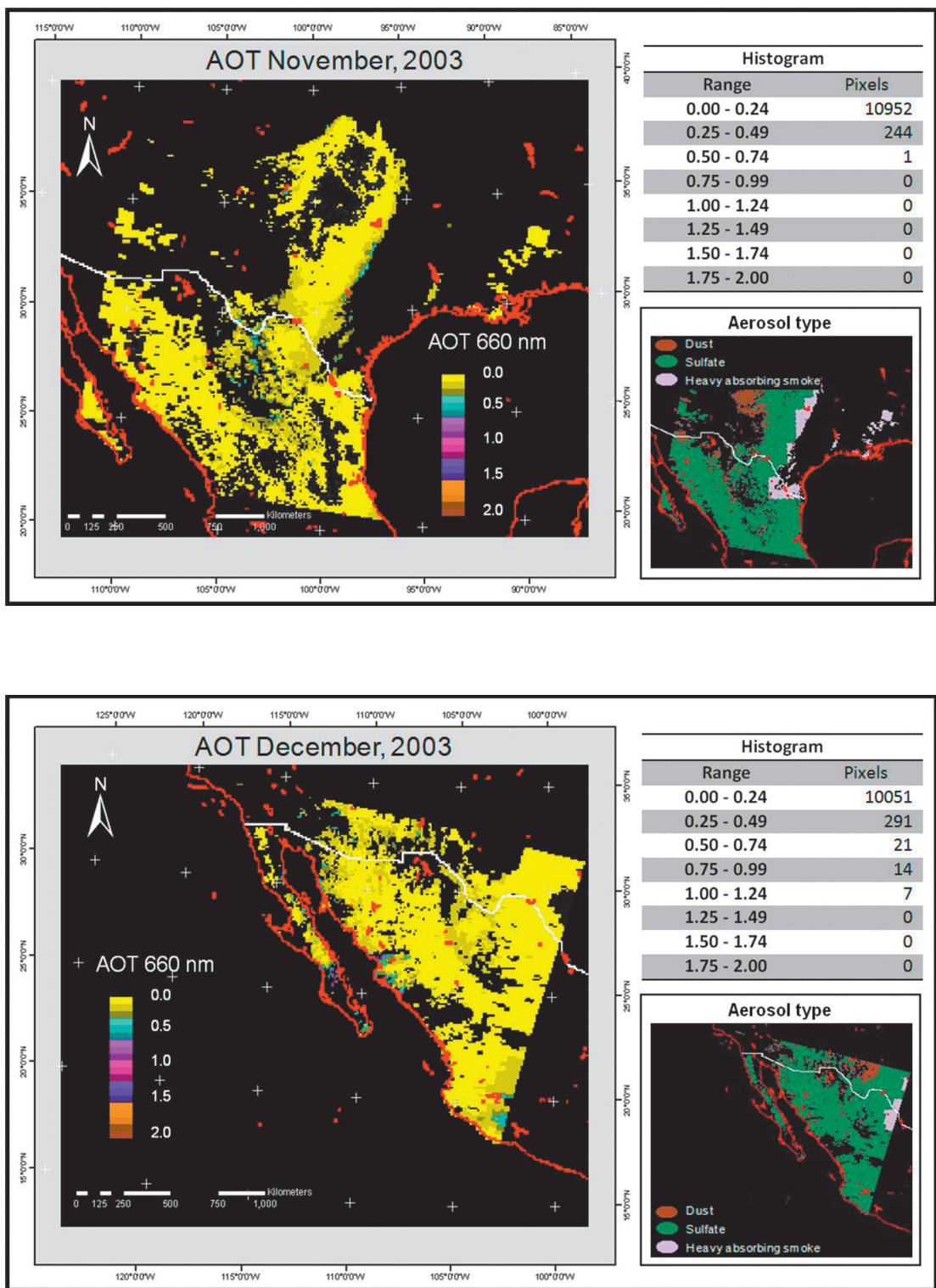
In general, highest values (>0.5) are located in the northwestern portion of Sonora, near Desert of Altar and northern coast of the state, although in this case it is possible to assume a similar distribution even when the images do not provide data for the whole area. These values are possibly related with the arid conditions of the region, because sparse vegetation and presence of the desert facilitate the incorporation of particles into the atmosphere that ultimately are recorded by the MODIS sensor.

Similarly, in relation to temporal variations, values close to 1.0 or higher on NWM set up during July 2001, June 2002, May 2003, and June 2003. Implying the existence of seasonal pattern between the rainy and the dry season, because based on the analysis of annual precipitation, we know that these months represent the driest period and then the beginning of rainy season, which is influenced by the Mexican monsoon when all of the dust particles work as hygroscope nuclei in cloud formation. Thus, it is possible to deduce that there is a pattern in the annual behavior, presenting highest values in June and July for 3 years and lowest values on December and January for the 2001–2003 period.

The pattern of increasing and decreasing of AOT over the first and second halves of the years, respectively, are clearly presented in 2001 and 2002, while in 2003, a second peak in AOT concentration is observed in plots and images. It happens on August and September, mainly in the portion near to interior coast of Gulf of Baja California, the Altar Desert, and the center of the peninsula, which might be related with the presence of two stronger cyclonic events during hurricane season in 2003. These were cyclones Ignacio and Marty respectively (NOAA, 2003a; NOAA, 2003b) while in the month of October of the same year, after the passage of two hurricanes, the pattern of behavior was re-established and exhibited a decrease in AOT values in December as in two previous years. In addition, it took into account the periods with higher rainfall, consistent with the summer and fall months (year 2003), during which it is known that rainfall is greatest in NWM, also due to moisture penetration on the continent connected with Mexican Monsoon and Southwest Monsoon of America (Reyes *et al*., 1994).

In the case of Baja California peninsula, throughout the study period, we identify the highest values (0.5–1.0 and over), on May, June, July, and August 2001, June 2002, and in April, May, and July 2003. Generally, we observed that the peninsula has the highest values throughout the period, unlike the NWM mainland. Possibly related with the narrow north-south profile of this physiographic province, which is influenced by

aerosols of marine origin throughout East-West extension and that is reflected in measurements made by the sensor and in processed images.

Additionally, by analyzing the histograms of each image and once identified those areas with highest concentration of particles in the region and seasonal patterns, we are able to notice that images with the highest concentration of valued pixels show lower ranges (0.00–0.24 and 0.25–0.99); especially in January, February, March, and April 2001, increasing from May until July. In this increase, the pixels are related with classes or ranges between 0.5 and 0.99, subsequently decreasing from August to December of that year.

This behavior is repeated in the same way in 2002 and 2003, years covered in the study, which also has the highest concentration of pixels of <0.49 in the first and last months of each year, while there was an increased presence of values >0.5 in total existing pixels in the images presented in June, 2002, May 2003, and July 2003.

In relation to these histograms, it is noteworthy that their analysis is relative, because the amount and location of the pixel value is not uniform in all images and covered area is different for each image. Nonetheless the observed behavior corresponds to the criteria given previously and reaffirms spatial and temporal patterns of AOT.

In each map presented, there is also attached information related with the predominant aerosol type in the atmosphere, which was obtained from a sub-product of MD04L2 related to this parameter. This exhibits a notoriously large predominance of sulfate aerosols in contrast with the other types shown in NWM images, in which a direct relationship was not identified between aerosol type and particle-concentration values expressed by AOT. It is interesting to notice that dust-related aerosols are generally located in northern areas of states of Chihuahua, Coahuila and Nuevo León and in the southern U.S. along border areas (Figure 8).

The third type of aerosol, heavy absorption smoke, was not identified on NWM. Thanks to coverage of some images and to availability of information of this parameter is possible to determine its concentration in the entire Northern coastal area Gulf of Mexico, where oil is probably the activity that affects particle emission to the atmosphere. The same type of aerosol particles is also identified is also identified in the lower Mississippi River Basin, mainly in the agricultural region of the U.S. which extends from Illinois to the border with Mexico in the State of Texas. While our work is focused on NWM, there is no presence of this type of particle in any analyzed image.

Furthermore, we observe in the images that highest values are located mainly near to the coast of the Gulf of Baja California and these values decrease in the interior region of the state of Sonora, increasing again, but less so than on the coast, on western slope of Sierra Madre Occidental. In this area the presence of natural vegetation encourages the emission of biomass into the atmosphere in larger quantities than in the areas located in the center of the entity, where there are drier zones.

Additionally, it is notorious that in most of the maps, highest AOT values are found near latitude 30°, which is possibly related to the transport of particles from the arid Southwestern U.S., under influence of trade winds and westerlies. Although it should be remarked that the influence of Santa Ana winds (JPL, 2002) in NWM may explain the higher concentration of suspended particles in Baja California peninsula and the coastline of the states of Sonora and Sinaloa. Despite we do not observe their overall influence on AOT spatial-temporal variation for the entire region from October to March, when Santa Ana winds occur, this does not correspond to months with the greatest increase in optical thickness.

As part of the analysis of AOT images, we also undertook identification of hotspots in satellite images provided by the National Commission for the Knowledge and Use of Biodiversity (CONABIO, 2010) to determine whether during study period, the occurrence of wildfires was active in terms of particle emission to the atmosphere. However, no direct relationship was found because, in all images analyzed. We identified that the greatest concentration of hotspots is related to wild fires in the central and southern part of Mexico. Thus, while it is appropriate to take the occurrence of these events into account, we not considered that they have a higher weight in AOT values.

Finally, by comparing the behavior of AOT along 3-year study period, we were unable to observe a gradual increase in the concentration of particles in the atmosphere because, according to the graphs of temporal AOT variation, the year 2003 in general exhibited values below those of the average. Despite what we might expect if we relate these variations to chronic expansion of urban areas throughout the country and consequently increasing emissions of anthropogenic aerosols. Based on the criteria presented in this subsection related to analysis of final maps, to histograms of each graph, and to AOT behavior, these appear to confirm the identification of a seasonal pattern in the behavior of optical thickness in NWM during 2001–2003. Besides this pattern can also be influenced by the occurrence of extraordinary events throughout each year, but in general there were no significant changes in the space-time trend.

## Conclusions

By means of performing a study of the correlation between data measured by the AERONET sensor in the city of Hermosillo, Sonora, Mexico, and those of the MODIS satellite, we obtained a correlation coefficient of $R^2 = 0.891$. The study allows us to observe the behavior of the aerosol particles at this site during the 2001–2003 period. Thus, we consider that the data employed in this research are reliable for their purposes and useful in identifying temporal and spatial patterns in AOT behavior.

The main pattern observed depicts highest AOT values during the rainy season in NWM and in the 2 prior months. The relationship between these values can be associated with low atmospheric pressures due to high temperatures, which cause convergence of air masses related to North American monsoon. The convective air currents encourage and facilitate the incorporation of particles into the atmosphere before rainy season and the formation of high vertical developed clouds from August to October.

Furthermore, other factors were identified in AOT behavior, as well hurricanes during the rainy season in 2003, generating highest values for that year despite its low values in comparison with the whole 3-years period.

In addition to the influence of the physiographic shape of Baja California peninsula and inland NWM in AOT values, the presence of large areas with scarce vegetation aids to stimulate the emission of particles from the ground. In the same way, high-density vegetation areas increase biomass emission in mountain ranges located on eastern portion of Sonora.

Finally, it was not possible to compare the results of this research with others, considering that to our knowledge, there are no previous attempts to study aerosol behavior in NWM. Thus, further work is required to build up a stronger database in order to helps monitor and understand how AOT values are influenced by different factors and how these are related to information from researches in several scientific fields.

## Bibliography

Bai L., Xue Y., Guang J., Wang Y., Li Y., Ai J., Wan W., Guo J., 2008, Primary Validation of the Syntem Aerosol Retrieval Model over Beijing Area Using Aeronet Data, in XXIst ISPRS Congress, 37, edited by C. Jun, pp. 195–200, Beijing.

Bosch J.L., Batlles F.J., Zarzalejo L.F., López G., 2010, Solar resources estimation combining

digital terrain models and satellite images techniques, *Renewable Energy*, 35, 12, 2853–2861 [online] Available from: http://www.sciencedirect.com/science/article/pii/S0960148110002296.

Broesamle H., Mannstein H., Schillings C., Trieb F., 2001, Assessment of solar electricity potentials in North Africa based on satellite data and a geographic information system, *Solar Energy*, 70, 1, 1–12 [online] Available from: http://www.sciencedirect.com/science/article/pii/S0038092X00001262.

Charlson R.J., Schwartz S.E., Hales J.M., Cess R.D., Coakley J.A., 1992, Climate Forcing by Anthropogenic Aerosols, *Science*, 255(5043), 423–430, doi:10.1016/0168-583X(95)00944-2 [online] Available from: http://linkinghub.elsevier.com/retrieve/pii/0168583X95009442.

Chia A.S., Lim K.H., Chew B.N., Salinas S.V., Liew S.C., 2007, Detection of smoke haze from vegetation fires using modis aerosol products, in 28th Asian Conference on Remote Sensing, pp. 1–6, Curran Associates, Inc., Kuala Lumpur, Malaysia. [online] Available from: http://www.a-a-r-s.org/acrs/proceeding/ACRS2007/Papers/PS1.G6.3.pdf.

CONABIO, 2010, Sistema de Alerta Temprana de Incendios Forestales, Comisión Nacional para el Conocimiento y Uso de la Biodiversidad [online] Available from: http://www.conabio.gob.mx/incendios/.

Correia A., Pires C., 2006, Validation of Aerosol Optical Depth Retrievals by Remote Sensing over Barzil and South America Using MODIS, in XIV Congresso Brasileiro de Meteorologia, pp. 1–7, Florianópolis, Brazil. [online] Available from: http://www.cbmet.com/cbm-files/14-44954441ffd7f22785afbe0248c3b8b3.pdf.

Deepak A., 1982, Atmospheric Aerosols, Their Formation, Optical Properties and Effects, *Spectrum Press*, Hampton, VA, USA.

Glantz P., Nilsson D.E., Von Hoyningen-Huene W., 2006, Estimating a relationship between aerosol optical thickness and surface wind speed over the ocean, *Atmospheric Chemistry and Physics Discussions*, 6, 11621–11651 [online] Available from: http://www.atmos-chem-phys-discuss.net/6/11621/2006/acpd-6-11621-2006.pdf.

Grosso N., Ferreira F., Mesquita S., 2007, Improvement in particles (PM10) urban air quality mapping interpolation using remote sensing data, in Air Pollution Modeling and Its Application XVIII, vol. Volume 6, edited by C. B. and E. R. B. T.-D. in *E. Science*, pp. 265–274, Elsevier. [online] Available from: http://www.sciencedirect.com/science/article/pii/S1474817707060317.

Gueymard C.A., Wilcox S.M., 2011, Assessment of spatial and temporal variability in the US solar resource from radiometric measurements and predictions from models using ground-based or satellite data, *Solar Energy*, 85(5), 1068–1084 [online] Available from: http://www.sciencedirect.com/science/article/pii/S0038092X11000855.

Ichoku C., Chu D.A., Mattoo S., Kaufman Y.J., Remer L.A., Tanré D., Slutsker I., Holben B.N., 2002a, A spatio-temporal approach for global validation and analysis of MODIS aerosol products, *Geophysical Research Letters*, 29, 12, 1–4, doi:10.1029/2001GL013206 [online] Available from: http://www.agu.org/pubs/crossref/2002/2001GL013206.shtml.

Ichoku C., Kaufman Y.J., Remer L.A., Levy R., Chu D.A., Rong-Rong L., Tanré D., Mattoo S., 2002b, MODIS aerosol products: quality assessment and regional application case studies based on two years of operation, in *Geoscience and Remote Sensing Symposium*, 2002. IGARSS '02. 2002 IEEE International, pp. 1180–1182.

INEGI, 2011, Proyecto de Infromación Básica de INEGI, Instituto Nacional de Estadística y Geografía [online] Available from: http://mapserver.inegi.gob.mx/geografia/espanol/prodyserv/iris3/seccion/proyinfbasica.cfm (Accessed 11 February 2013).

Iqbal M., 1983, An Introducction to Solar Radiation, University of British Columbia, Toronto, Canada.

JPL, PHOTOJOURNAL, 2002, Dusty Skies over Southern California, Jet Propulsion Laboratory [online] Available from: http://photojournal.jpl.nasa.gov/catalog/PIA03445.

Liang S., Zhong B., Fang H., 2006, Improved estimation of aerosol optical depth from MODIS imagery over land surfaces, *Remote Sensing of Environment*, 104, 416–425, doi:10.1016/j.rse.2006.05.016 [online] Available from: http://linkinghub.elsevier.com/retrieve/pii/S0034425706002045 (Accessed 5 August 2010).

NOAA, 2003a, Tropical Cyclone Report. Hurricane Ignacio, National Hurricane Center [online] Available from: http://www.nhc.noaa.gov/2003ignacio.shtml.

NOAA, 2003b, Tropical Cyclone Report. Hurricane Marty, National Hurricane Center [online] Available from: http://www.nhc.noaa.gov/2003marty.shtml.

Perez R., Seals R., Zelenka A., 1997, Comparing satellite remote sensing and ground network measurements for the production of site/time specific irradiance data, *Solar Energy*, 60, 2, 89–96 [online] Available from: http://www.sciencedirect.com/science/article/pii/S0038092X96001624.

Remer L.A., Tanré D., Kaufman Y.J., Ichoku C., Mattoo S., Levy R., Chu D.A., Holben B., Dubovik O., Smirnov A., Martins J.V., *et al*., 2002, Validation of MODIS aerosol retrieval over ocean, *Geophysical Research Letters*, 29, 12, MOD3–1–MOD3–4.

Remer L.A., Tanré D., Kaufman Y.J., Levy R., Mattoo S., 2006, Algorithm for Remote Sensing of Tropopheric Aerosol from MODIS: Collection 5 Product ID: MOD04/MYD04.

Reyes S., Douglas M.W., Maddox R.A., 1994, El monzón del suroeste de Norteamérica, *Atmósfera*, 7, 117–137.

Triola M., 2008, Estadística, 10th ed., Pearson Educación, Mexico City.

Wolfe R.E., Roy D.P., Vermote E., 1998, MODIS land data storage, gridding, and compositing methodology: Level 2 grid, *Geoscience and Remote Sensing*, IEEE Transactions on, 36, 4, 1324–1338.

**APPENDIX 1**

**Table 1.** Data availability from Moderate Resolution Imaging Spectroradiometer (MODIS) and AErosol RObotic NETwork (AERONET).

| Date | MODIS (660 nm) | AERONET (675 nm) | Date | MODIS (660 nm) | AERONET (675 nm) |
|------|------|------|------|------|------|
| 15/11/2001 | 0.047000 | 0.02151636 | 05/06/2002 | 0.362714 | 0.13462458 |
| 16/11/2001 | 0.163150 | 0.03446177 | 08/06/2002 | 0.345778 | 0.14995492 |
| 17/11/2001 | 0.087000 | 0.03355362 | 09/06/2002 | 0.365000 | 0.06558950 |
| 19/11/2001 | 0.110375 | 0.04732900 | 12/06/2002 | 0.390875 | 0.14424058 |
| 20/11/2001 | 0.147600 | 0.03939413 | 14/06/2002 | 0.642000 | 0.15638400 |
| 21/11/2001 | 0.098000 | 0.04258614 | 15/06/2002 | 0.319500 | 0.14523883 |
| 25/11/2001 | 0.139846 | 0.03491987 | 16/06/2002 | 0.739000 | 0.11349450 |
| 27/11/2001 | 0.134500 | 0.03744760 | 17/06/2002 | 0.262231 | 0.10734983 |
| 28/11/2001 | 0.097308 | 0.04334970 | 18/06/2002 | 0.350000 | 0.10298600 |
| 01/12/2001 | 0.068889 | 0.03290827 | 19/06/2002 | 0.341333 | 0.09602550 |
| 02/12/2001 | 0.120050 | 0.02228500 | 21/06/2002 | 0.439333 | 0.09180567 |
| 03/12/2001 | 0.022143 | 0.01115900 | 25/06/2002 | 0.615000 | 0.13830422 |
| 13/12/2001 | 0.108263 | 0.01001254 | 26/06/2002 | 0.428000 | 0.17784543 |
| 16/12/2001 | 0.101826 | 0.03282064 | 27/06/2002 | 0.401000 | 0.19024858 |
| 17/12/2001 | 0.047667 | 0.01083812 | 30/06/2002 | 0.674333 | 0.16896028 |
| 18/12/2001 | 0.100737 | 0.03201989 | 01/09/2002 | 0.154000 | 0.11731225 |
| 19/12/2001 | 0.025385 | 0.01651793 | 02/09/2002 | 0.404000 | 0.18827701 |
| 20/12/2001 | 0.116947 | 0.02131789 | 05/09/2002 | 0.257280 | 0.10057900 |
| 21/12/2001 | 0.050429 | 0.02466560 | 12/09/2002 | 0.157333 | 0.06258500 |
| 22/12/2001 | 0.097143 | 0.01854000 | 13/09/2002 | 0.116000 | 0.05697200 |
| 23/12/2001 | 0.060143 | 0.02065667 | 14/09/2002 | 0.140957 | 0.05644433 |
| 24/12/2001 | 0.065250 | 0.02142057 | 16/09/2002 | 0.258667 | 0.08315050 |
| 25/12/2001 | 0.089650 | 0.00585738 | 21/09/2002 | 0.172524 | 0.09421967 |
| 26/12/2001 | 0.025200 | 0.02577600 | 22/09/2002 | 0.151000 | 0.04333180 |
| 05/01/2002 | 0.133684 | 0.01517575 | 23/09/2002 | 0.128400 | 0.04876790 |
| 06/01/2002 | 0.054333 | 0.00776320 | 25/09/2002 | 0.175000 | 0.06890750 |
| 07/01/2002 | 0.085143 | 0.02254000 | 27/09/2002 | 0.212333 | 0.08882033 |
| 08/01/2002 | 0.081563 | 0.01104217 | 28/09/2002 | 0.220000 | 0.08812280 |
| 03/06/2002 | 0.302125 | 0.09941730 | | | |

# Relationship between solar radiation and dimethylsulfide concentrations using in situ data for the pristine region of the southern hemisphere

Jaime Osorio, Blanca Mendoza and Jorge Zavala-Hidalgo

**Resumen**

Los procesos biológicos han sido propuestos como una de las componentes que hacen variar el clima. El Dimetilsulfuro (DMS) es el principal componente del sulfuro biogénico en la atmósfera. El DMS es producido, principalmente, por la biósfera marina y juega un papel importante en el ciclo del azufre atmosférico. Actualmente se acepta que la biota terrestre no sólo se adapta a las condiciones ambientales sino que las influencia a través de regulaciones en la composición química de la atmósfera. En este estudio se utiliza el método de ondeletas para investigar la relación entre DMS, Nubes bajas (LCC), Radiación Ultravioleta A (UVA), Radiación Solar Total (TSI) y Temperatura Superficial Oceánica (SST) en la llamada zona prístina del Hemisferio Sur. Se encontró que las series analizadas presentan diferentes periodicidades que pueden ser asociadas con fenómenos climáticos de gran escala tales como El Niño (ENSO) o la Oscilación Cuasi-Bienal (QBO), y/o con la actividad solar. Los resultados indican, de manera intermitente pero sostenida, una correlación DMS-SST y una anti-correlación DMS-UVA; pero DMS-TSI y DMS-LCC tienen una relación no lineal. La longitud temporal de las series sólo nos permite analizar periodicidades menores a 11 años, entonces, nos limitamos a analizar la posibilidad de que la radiación solar influya en el clima de la Tierra en periodos de tiempo menores que el ciclo solar de 11 años. Nuestros resultados también sugieren una interacción de retroalimentación positiva entre el DMS y la radiación solar.

Palabras clave: Dimetilsulfuro, Radiación Solar, clima, nubes, retroalimentación, análisis de Ondeleta.

**Abstract**

The biological processes have been proposed as climate variability contributors. Dimethylsulfide (DMS) is the main biogenic sulfur compound in the atmosphere; it is mainly produced by the marine biosphere and plays an important role in the atmospheric sulfur cycle. Currently it is accepted that terrestrial biota not only adapts to environmental conditions but also influences them through regulations of the chemical composition of the atmosphere. In the present study we used a wavelet method to investigate the relationship between DMS, Low cloud cover (LCC), Ultraviolet Radiation A (UVA), Total Solar Irradiance (TSI) and Sea Surface Temperature (SST) in the so called pristine zone of the Southern Hemisphere. We found that the series analyzed have different periodicities which can be associated with large scale climatic phenomena such as El Niño (ENSO) or the Quasi-Biennial Oscillation (QBO), and/or to solar activity. Our results show an intermittent but sustained DMS-SST correlation and a DMS-UVA anti correlation; but DMS-TSI and DMS-LCC show nonlinear relationships. The time-span of the series allow us to study only periodicities shorter than 11 years, then we limit our analysis to the possibility that solar radiation influences the Earth climate in periods shorter than the 11-year solar cycle. Our results also suggest a positive feedback interaction between DMS and solar radiation.

Key words: Dimethylsulfide, Solar Radiation, climate, clouds, feedback, wavelet analysis.

J. Osorio
Posgrado en Ciencias de la Tierra
Instituto de Geofísica
Universidad Nacional Autónoma de México
Circuito Exterior s/n,
Ciudad Universitaria
Del. Coyoacán, 04510
México D.F., México.
*Corresponding author: jaime@geofisica.unam.mx

B. Mendoza
Departamento de Ciencias Espaciales
Instituto de Geofísica
Universidad Nacional Autónoma de México
Circuito Exterior s/n,

Ciudad Universitaria
Del. Coyoacán, 04510
México D.F., México.

J. Zavala-Hidalgo
Interacción Océano-Atmósfera
Centro de Ciencias de la Atmósfera
Universidad Nacional Autónoma de México
Circuito Exterior s/n,
Ciudad Universitaria
Del. Coyoacán, 04510
México D.F., México.

## Introduction

The solar activity has been proposed as an external factor of Earth's climate change. Solar phenomena such as total and spectral solar irradiance could change the Earth's radiation balance and hence climate (Gray *et al*., 2010). However, biological processes have also been proposed as another factor of climate change through its impact on albedo associated with clouds. One of the most important issues regarding the Earth function system is whether the biota in the ocean responds to changes in climate (Charlson *et al*., 1987, Miller *et al*., 2003, Sarmiento *et al*., 2004). According to several authors, the major source of cloud condensation nuclei (CCN) over the oceans is dimethylsulfide (DMS) (e.g., Andreae and Crutzen, 1997; Vallina *et al*., 2007).

Dimethyl Sulphonium Propionate in phytoplankton cells is released into the water column where it is transformed into dimethylsulfide. The dimethylsulfide goes through the sea surface to the atmosphere as a gas, where it oxidizes to form a range of products, among them $SO_2$. This compound oxidizes to $H_2SO_4$, which forms sulphate particles that act as CCN. The dimethylsulfide concentration is controlled by the phytoplankton biomass and by a web of ecological and biogeochemical processes driving by the geophysical context (Simó, 2001). Solar radiation is the primary driving mechanism of the geophysical context and is responsible for the growth of the phytoplankton communities. Clouds have a major impact on the amount of heat and radiation budget of the atmosphere. Clouds modify both albedo (short-wave) and long-wave radiation. In particular, for low clouds over oceans, the albedo effect is the most important result of cloud radiation interaction and has a net cooling effect on the climate (Chen *et al*., 1999, Rossow, 1999).

The DMS, solar radiation and cloud albedo are hypothesized to have a feedback interaction (Charlson *et al*., 1987; Shaw *et al*., 1998; Gunson *et al*., 2006). This feedback can be either negative or positive. A negative feedback process requires a positive correlation between solar irradiance and DMS: increases in solar irradiance reaching the sea surface increase the DMS, augmenting the CCN and the albedo. An overall increase in the albedo produces a decrease in the irradiance reaching the sea surface and thus cooling occurs. A positive feedback requires an anti-correlation between solar irradiance and the DMS: decreases in solar irradiance produce a decrease of the DMS, the CCN and the albedo; a net reduced albedo allows more radiation to be absorbed, producing heating. Using seasonal and annual time scales, a first attempt to find correlations between a global database of DMS concentration and several geophysical parameters was unsuccessful (Kettle *et al*., 1999).

Quantitative studies that use data bases spanning roughly three decades (Simó and Dachs, 2002; Simó and Vallina, 2007; Vallina *et al*., 2007) have concluded that the DMS and solar radiation have a high positive correlation on seasonal time scales for most of the ocean, favoring a negative feedback on climate. Another study (Larsen, 2005), based on a conceptual model, proposed a positive feedback. A positive feedback would also imply an anti-correlation between Total Solar Irradiance (TSI) and cloud cover. Indeed, a global anti-correlation between TSI and oceanic low cloud cover has been found (Kristjánsson *et al*., 2002; Lockwood, 2005). Furthermore, case studies using ultraviolet (UV) light do not allow conclusive results regarding the sign of the solar radiation-DMS correlation (Kniventon *et al*., 2003; Toole and Siegel, 2004; Toole *et al*., 2006).

Another study on decadal relation between north and south high latitude concentrations of Methane Sulphonic Acid (MSA), associated exclusively to DMS, and TSI, found that at the time scales coincident with the 22-years magnetic solar cycle, the north-MSA and TSI follow each other, favoring a negative feedback on local climate; but at the time scales of the 11-years solar cycle for north and south, the MSA-TSI presents an anti-correlation that has increased since the 1940s favoring a positive feedback on local climate (Mendoza and Velasco, 2009), this indicates that the relations between the variables of interest may change with time and location.

The purpose of the present study is to examine in a selected location of the Southern Hemisphere and at time-scales shorter than the solar cycle the relationship between DMS and climate and DMS and solar phenomena, through clouds, sea surface temperature (SST) and the UV radiation A (UVA). A time series of UV radiation was used because this radiation has a role in a number of the key processes controlling DMS concentrations in seawater. Several studies link the production of DMS and UV (e.g. Toole *et al., 2006, Kniventon *et al*., 2003), some studies report increases and other significant decreases in DMS production, also the phytoplankton responds dramatically to UV radiation (Toole and Siegel, 2004). These studies indicate a relationship between UV and DMS in the ocean (Kniventon, 2003).

### Region of study and data

The data analysis was performed for the Southern Hemisphere between 40º- 75ºS latitude and 150W-155E longitude. Considering the abundance of chlorophyll by regions, this area includes the biogeochemical provinces ANTA, APLR, CHIL, FKLD, SANT and SSTC (Longhurst, 1995).

The concept of biogeochemical provinces is based on the observation that large ocean regions are characterized by coherent physical forcing and biological conditions at the seasonal scale, which are representative of macroscale ocean ecosystems. The boundaries between provinces are generally persistent but are also spatially and temporally variable, because they are linked to physical properties which are known to change position seasonally and inter annually. The boundaries of Longhurst's provinces were selected subjectively and intuitively on the basis of climatological data (mixed layer depth, solar irradiance penetration and chlorophyll concentrations) and common knowledge on the biological properties extracted from scattered data in the existing literature (Longhurst, 1995; Hardman-Mountford *et al.* 2008).

Longhurst (1995) recognize four primary domains of the global pelagic ecosystem. The first one is Polar: the seasonal cycle of sea ice in high latitudes results in a brackish surface layer in spring and summer as freshwater is released from melting winter ice cover; this phenomenon occurs most consistently in the marginal ice zone and leads to an active bloom as soon as ice break-up occurs). The second domain is Westerlies: the defining characteristic of this domain is seasonality in wind stress imposed by the westerlies associated with the Aleutian, Iceland and Antarctic atmospheric low-pressure cells, together with seasonality in the radiation flux at the sea surface. The third domain is Trade Winds: the Ekman layer of low latitudes is resistant to wind deepening and the scale of baroclinicity is weeks, rather than years as in higher latitude. The fourth domain is Coastal: the characteristic of this domain is to embrace the concept of a coastal boundary domain as defined for regions where the general oceanic circulation is significantly modified by interaction with coastal topography and with its coastal wind regimen.

These are themselves partitioned into 57 secondary biogeochemical provinces which we have used as the units of our global computation of primary production. For the Polar domain we use the biogeochemical provinces ANTA (Antarctic. Lies between the Polar Frontal Zone and the Antarctic Divergence, having two components: a zone of permanently open water and a zone seasonally carrying pack ice) and APLR (Austral Polar. This is a ribbon of westward-moving Antarctic Surface Water, up to 300 km wide, ice covered in winter but with some open water areas in summer, between the Antarctic Divergence and the continent). For the Westerlies domain we use the biogeochemical provinces SANT (Subantarctic. From the Subtropical Convergence south to the Antarctic Polar Front, which is the southern limit of the Polar Frontal zone and

which covers ~4º latitude) and SSTC (South Subtropical Convergence. The most northerly of the annular features of the Southern Ocean. The frontal zone is sufficiently dynamic to have an associated eddy field and includes several surface discontinuity fronts). For the Coastal domain we use the biogeochemical provinces CHIL (Chile-Peru Current Coastal. Defined, like its Benguela homologue, as extending from the coastline to the offshore anticyclonic eddy field. To the south, it is defined by the divergence zone at ~45º S and to the north at its separation from the coast near the equator) and FKLD (Southwest Atlantic Continental Shelf. Argentine shelf and Falklands Plateau from Mar de Plata to Tierra del Fuego) (Longhurst, 1995).

This area (study region) is the least polluted in the world, the so-called pristine zone, and then solar effects on biota and climate should be more evident. Over 90% of the area is ocean; the remaining 10% corresponds to the southern parts of Chile, Argentina, Tasmania and New Zealand (South Island). The studied period is 1983-2010, containing almost 27 years of data.

The DMS data set was obtained from NOAA-Global Surface Seawater Dimethylsulfide Database (http://saga.pmel.noaa.gov/dms). The original data series in this database contains the DMS measurements collected in the global oceans during 1972-2011 and are given as raw data samples (Figure 1a). The sequence of data presents important gaps in space and time; more details are given in Kettle *et al*. (1999).We can take a monthly resolution for the DMS data along full year periods, regardless of the polar jet stream effects, since this jet blows at an altitude ranging from 11 to 16 kilometers, and therefore does not have interaction with the DMS concentrations (Savitskiy and Lessing, 1979; Gallego *et al*., 2005; Pidwirny, 2006).

We also use the SST time series (Figure 1b), obtained from NOAA-Earth System Research Laboratory (http://www.esrl.noaa.gov/psd/cgi-bin/data/timeseries/timeseries1.pl). Used here is the Low Cloud Cover Anomaly data (LCC) from the International Satellite Cloud Climatology Project (ISCCP) (http://isccp.giss.nasa.gov); two series of low cloud cover anomalies were obtained: Visible-Infrared (VIS-IR) and Infrared (IR) (Figs. 1c and 1d).

Additionally, we work with the UVA between 320 to 400 nm, because 95% of wavelengths longer than 310 nm reach the surface (Lean *et al*., 1997) and has a large impact on marine ecosystems (Häder *et al*., 2003; Toole *et al*., 2006; Hefu *et al*., 1997; Slezak *et al*., 2003; Kniventon *et al*., 2003; Häder *et al*., 2011). We use the UVA composite series constructed from

the Nimbus 7 (1978-1985), NOAA-9 (1985-1989), NOAA-11 (1989-1992) and SUSIM satellites between 1992 and 2008 (DeLand *et al*., 2008). The atmospheric attenuated UVA series was calculated at sea surface level using the Santa Barbara Disorted Atmospheric Radiative Transfer (SBDART) program; it was obtained from the site http://www.icess.ucsb.edu/esrg/SBDART. html (Ricchiazzi *et al*., 1998). The average UVA attenuation at surface was estimated to be ~ 5% less than at the top of the atmosphere (Figure 1e).

Finally, we work with the PMOD composite TSI time series obtained from the Physikalisch Meteorologisches Observatorium Davos-World Radiation Center (Fröhlich, 2009) (Figure 1f) (ftp:// ftp.pmodwrc.ch/pub/data/irradiance/composite/ DataPlots/ext_composite_d41_62_1204.dat).

## The method

Some of the previous efforts on elucidating a plausible contribution of DMS on the Earth's climate have been mostly based on correlation analysis models. Such analysis suggest certain relation between the time series, however, they are of global nature and do not provide precise information about such relations. Moreover, the fact that two series have similar periodicities does not necessarily imply that one is the cause and the other is the effect, and even if the correlation coefficient is very low, there is the possibility of an existing relation in spite of a low spectral power of one or both time series. Here we apply the wavelet method that allows to address such problems.

### *Wavelet Analysis*

In order to analyze local variations of power within a single non-stationary time series at multiple periodicities we apply the wavelet method using the Morlet Wavelet (Torrence and Compo, 1998; Grinsted *et al*., 2004).

The Morlet Wavelet consists of a complex exponential, where is the time, is the wavelet scale and is the non-dimension frequency. Here we use in order to satisfy the admissibility condition (Farge, 1992). Torrence and Compo (1998) have defined the wavelet power , where is the wavelet transform of a time series and is the time index.

We estimate the significance level for each scale using only values inside the cone of influence (COI). The COI is the region of the wavelet spectrum out of which edge effect become important and is defined here as the e-folding time for the autocorrelation of wavelet power at each scale.

This e-folding time is chosen so that the wavelet power for a discontinuity at the edge drops by the factor and ensures that the edge effects are negligible beyond this point (Torrence and Compo, 1998).

Wavelet power spectral density was calculated for each of the time series described in Section 2, the black thin lines mark the interval of 95% confidence or COI. An appropriate background spectrum is either the white noise (with a flat power spectrum) or the red noise (increasing power with decreasing frequency). We calculate the significance levels in the global wavelet spectra with a simple red noise model (Gilman *et al*., 1963). We only take into account those periodicities above the red noise level.

Furthermore, we find the wavelet coherence spectra (Torrence and Compo, 1998; Grinsted *et al*., 2004). It is especially useful in highlighting the time and frequency intervals when the two phenomena have a strong interaction. If the coherence of two series is high, the arrows in the coherence spectra figures show the phase between the phenomena. Arrows at (horizontal right) indicate that both phenomena are in phase, and arrows at (horizontal left) indicate that they are in anti-phase. It is very important to point out that these two cases imply a linear relation between the considered phenomena. Arrows at and (vertical up and down, respectively) or any other angle imply a non-linear or complex relation between the two series (Torrence and Compo, 1998).

We also include the global spectra in the wavelet and coherence plots, which is an average of the power of each periodicities inside the COI (Mendoza *et al*., 2007; Valdés-Galicia and Velasco, 2008; Velasco and Mendoza, 2008). The uncertainties of the peaks of both global wavelet and coherence spectra are obtained from the peak full-width at the half-maximum of the peak.

## Analysis and results

The results obtained with the wavelet analysis will be presented and discussed in this section.

### *The global wavelet spectrum*

The results of the wavelet method are shown in Figure 1, a summary of the periodicities found for all the time series is shown in Table 1. The DMS global wavelet spectrum (Figure 1a) shows significant periodicities ~2 and 4 years. The SST global wavelet spectrum (Figure 1b) shows only one periodicity close to 1 year. The LCC-IR global wavelet spectrum (Figure 1c) presents significant peaks ~0.6, 1.5, 2 and 8 years, and the LCCVIS-IR global spectrum has significant periodicities ~0.6, 1, 5 and 8 years but taking into account the uncertainties these peaks coincide with the LCC-IR

**Figure 1.** Wavelet Analysis. Each panel at the top shows the corresponding time series, at the middle the wavelet spectra and at the right the global wavelet spectra. (a) Dimethylsulfide (DMS), (b) Sea Surface Temperature (SST), (c) Low Cloud Cover Infrared Anomaly (LCC-IR), (d) Low Cloud Cover Visible-Infrared Anomaly (LCCVIS-IR), (e) Ultraviolet Radiation A (UVA), (f) Total Solar Irradiance (TSI). The color code indicating the statistical significance level for the spectral plots appears at the bottom of the figure; in particular the 95% level is inside the contours. The red dashed line in the global wavelet spectra represents the red noise level.

peaks. The UVA and TSI global wavelet spectrum (Figures 1e and 1f) show that the 11-years periodicity has the largest power, however its significance is low and partially outside the COI due to the short time interval.

*The wavelet coherence spectra*

The results of the wavelet coherence analysis appear in Figure 2 and present the coherence analysis between DMS vs SST, DMS vs LCC-IR, DMS vs LCCVIS-IR, DMS vs UVA and DMS vs TSI respectively. For each panel, the time

**Table 1.** Summary of periodicities.

| Periodicity (Yr) | TSp |
|---|---|
| **Dimethylsulfide (DMS)** | |
| 1.8 ± 0.2 | 1988-1994 |
| | 1998-2003 |
| 3.7 ± 0.4 | 1988-1994 |
| | 2001-2006 |
| **Sea Surface Temperature (SST)** | |
| 1 ± 0.5 | 1983-2010 |
| **Low Cloud Cover (IR)** | |
| 0.6 ± 0.1 | 1986-1987 |
| | 1998-2002 |
| 1.5 ± 0.5 | 1998-1999 |
| 1.8 ± 0.2 | 1996-2002 |
| 3.5 ± 0.5 | 1995-2002 |
| 4.5 ± 0.5 | 1993-2003 |
| 8.2 ± 0.8 | 1994-1999 |
| **Low Cloud Cover (VIS-IR)** | |
| 0.6 ± 0.1 | 1987-1988 |
| | 1994-1996 |
| 1 ± 0.5 | 1986-1988 |
| | 1994-1996 |
| | 1998-2000 |
| 5 ± 0.3 | 1990-2000 |
| 8.2 ± 0.3 | 1995-1999 |
| **Ultraviolet Radiation A (UVA)** | |
| 11 ± 3 | 1995-1999 |
| **Total Solar Irradiance (TSI)** | |
| 11 ± 3 | 1995-1999 |

TSp= Time Span inside the COI. The periodicities on or above the red noise level in the global wavelet plots appear in bold numbers.

series appears at the top, the wavelet coherence spectrum appears at the middle and the global wavelet coherence spectra is at the right. Table 2 summarizes the results; the strongest periodicities appear in bold number.

The Figure 2a shows that the DMS and SST time series have the most persistent and prominent coherence ~1 year and tends to be in phase, moreover, periodicities ~0.4, 2 and ~4 years, also notable in the wavelet coherence are

mainly in phase, the wavelet coherence spectra analysis show an intermittent but sustained correlation between the analyzed series.

The coherences between DMS and LCC-IR and LCCVIS-IR appearing in Figures 2b and 2c do not show a definite phase. The Figure 2d shows that the DMS and UVA time series have the most persistent and prominent coherence ~0.5, 1 and 3 year and tend to be in anti-phase, the anticorrelation (anti-phase) is intermittent but sustained; while the peak ~8 years is in phase but outside the COI due to the time interval of the series.

The Figure 2e shows that the DMS and TSI time series have the most persistent and prominent coherence ~2 years and tends to be in anti-phase, moreover, persistent coherence at ~0.4 and 1 year is out of phase and ~8 years is in phase but outside the COI due to the time interval of the series.

The periodicities found are between ~0.4 and ~8 years. Peaks shorter than 1 year may be due to seasonal climatic phenomena. The ~2 years period can be associated with the Quasi-Biennial Oscillation (QBO) in the stratosphere (Holton *et al*., 1972; Dunkerton, 1997; Baldwin *et al*., 2001; Naujokat, 1986; Holton *et al*., 1980) and with the solar activity (Kane, 2005). The QBO dominates the variability of the equatorial stratosphere and is easily seen as downward propagating easterly and westerly wind regimes, with a variable period averaging approximately 28 months. The QBO is a tropical phenomenon; it affects the stratospheric flow from pole to pole by modulating the effects of extratropical waves. The QBO is present also in other stratospheric parameters not only tropical but also extra-tropical weather and other regions, as the mesosphere and troposphere. There is an established body of literature (Roy and Haigh, 2011; Labitzke, 2012; Weng, 2012), initiated by the pioneering work of Labitzke (1987), which has identified the influence of solar activity on the QBO.

In particular, it was found that by segregating the meteorological data by the QBO phase a clear signal of the 11-year solar cycle was revealed. More specifically, that the January-February temperature at 30 hPa over the North Pole tends to be warmer during the west phase of the QBO at high solar activity (HS/wQBO) and also during the east phase at low solar activity (LS/eQBO). Consistently, cold polar temperatures occur during LS/wQBO and HS/eQBO (Labitzke and van Loon, 1992). Other results suggest that solar variability, modulated by the phase of QBO, influences zonal mean temperatures at high latitudes in the lower stratosphere, in the mid-latitude troposphere and sea level pressure near the poles (Roy and Haigh, 2011).
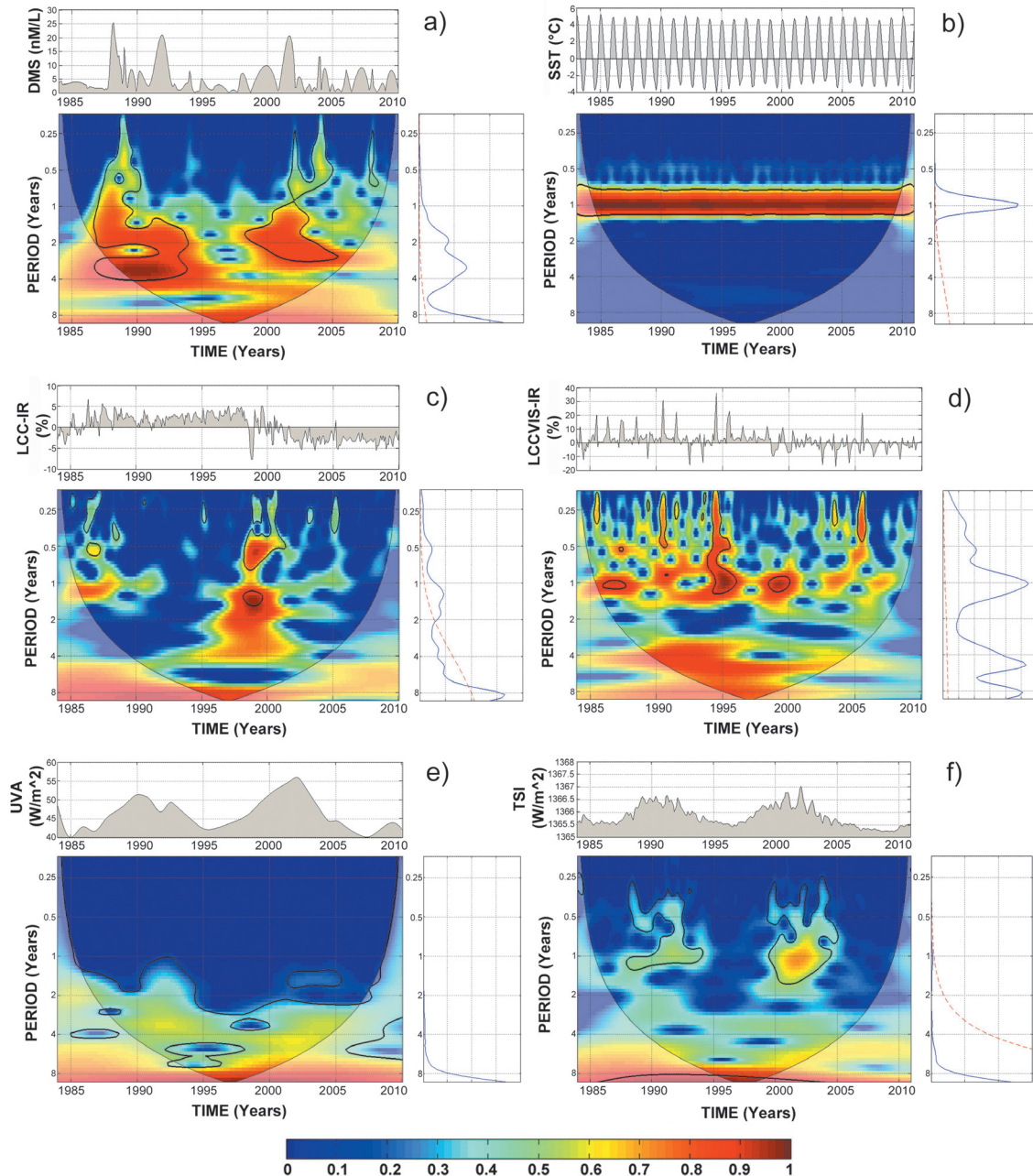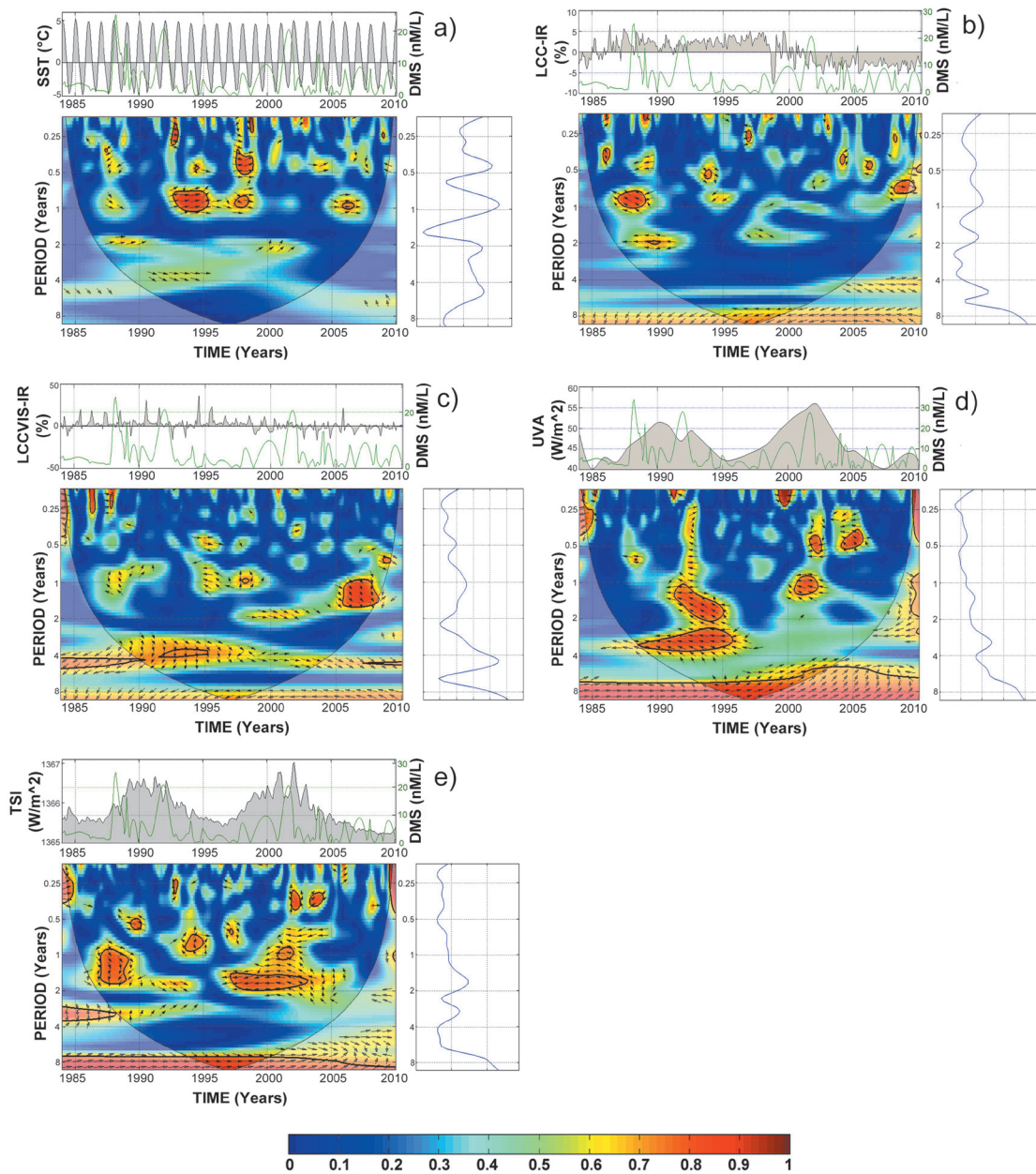
**Figure 2.** Wavelet Coherence Analysis. Each panel at the top shows the corresponding time series, at the middle the wavelet coherence spectra and at the right the global wavelet coherence spectra. (a) DMS vs SST, (b) DMS vs LCC-IR, (c) DMS vs. LCCVIS-IR (d) DMS vs UVA, (e) DMS vs. TSI. The color code indicating the statistical significance level for the spectral plots appears at the bottom of the figure; in particular the 95% level is inside the contours.

The periodicities ~3 and 4 years could be related to the El Niño-Southern Oscillation (ENSO) (Nuzhdina, 2002; Njau, 2006) and to a sunspot periodicity (Polygiannakis *et al., 2003*).

The ENSO is the result of a cyclic warming and cooling of the surface ocean of the central and eastern Pacific, it occurs at irregular intervals between 2 and 7 years in conjunction with the Southern Oscillation, a massive seesawing of atmospheric pressure between the southeastern and the western tropical Pacific.

The ENSO leads to changes in ocean temperature that influence salinity changing environmental conditions for marine ecosystems. These changes affect fish populations, marine phytoplankton and chlorophyll. The direct influence of ENSO is reflected in the ocean, marine biota and climate. Recent work suggest an ENSO- like response to the 11-year solar cycle that includes a La Niña like pattern assigned to solar maximum conditions (Bal *et al., 2011*). The solar activity has obvious influence on some large scale climatic phenomena, such as ENSO. Kirov and Georgieva (2002) found

**Table 2.** Summary of wavelet coherence results.

| Relation. | Periodicity (Yr) | TSp | Phase |
|---|---|---|---|
| **DMS vs SST** | 0.4 ± 0.1 | 1987-1989 | OUT |
| | | 1994-1996 | IN |
| | | 1997-1999 | IN |
| | | 2003-2005 | IN |
| | | 2006-2008 | OUT |
| | 0.9 ± 0.2 | 1986-1989 | IN |
| | | 1992-1996 | IN |
| | | 1996-1999 | IN |
| | | 2004-2008 | IN |
| | 2 ± 0.1 | 1987-1991 | IN |
| | | 1999-2003 | CHP |
| | 4.4 ± 0.3 | 1990-1996 | IN |
| **DMS vs LCC-IR** | 0.4 ± 0.1 | 1986-1987 | OUT |
| | | 1988-1993 | ANTI |
| | | 2003-2004 | CHP |
| | | 2005-2007 | ANTI |
| | 0.8 ± 0.3 | 1987-1990 | ANTI |
| | | 1994-1996 | OUT |
| | | 2007-2009 | IN |
| | 1.9 ± 0.2 | 1987-1992 | ANTI |
| | | 1996-2000 | OUT |
| | 3.2 ± 0.1 | 1991-2004 | IN |
| | 5 ± 0.1 | 1994-2001 | ANTI |
| | 8 ± 3 | 1995-2000 | ANTI |
| **DMS vs LCCVIS-IR** | 0.5 ± 0.1 | 1994-1996 | IN |
| | | 1997-1998 | OUT |
| | 1 ± 0.2 | 1987-1992 | CHP |
| | | 1993-2000 | CHP |
| | | 2005-2008 | OUT |
| | 5 ± 1 | 1990-2004 | CHP |
| | 8 ± 3 | 1995-2000 | ANTI |
| **DMS vs UVA** | 0.5 ± 0.1 | 2001-2003 | ANTI |
| | | 2004-2007 | ANTI |
| | 1.3 ± 0.1 | 1991-1996 | ANTI |
| | | 1999-2003 | ANTI |
| | 3 ± 0.9 | 1989-1997 | ANTI |
| | 8 ± 3 | 1994-2003 | IN |
| **DMS vs TSI** | 0.4 ± 0.1 | | |
| | | 2002-2003 | OUT |
| | | 2003-2005 | OUT |
| | 0.7 ± 0.3 | 1992-1996 | OUT |
| | | 1997-1998 | OUT |
| | 1.7 ± 0.3 | 1986-1990 | OUT |
| | | 1991-1994 | IN |
| | | 1996-2003 | ANTI |
| | 8 ± 3 | 1994-2000 | IN |

The strongest periodicities appear in bold numbers. TSp= time span inside the COI.
IN= in phase; ANTI= in anti-phase; OUT= out of phase; CHP= changing phase.

that solar activity influenced both the intensity and occurrence frequency of the ENSO.

Mufti and Shah (2011) found a significant positive correlation between the SST anomalies and sunspot indices in both the 11-year and 22-year bands. Similar results showing correlation between solar activity and El Niño are also shown by Weng (2005). The influences of solar activity on the different natural processes are broad and extensive. However, large scale climatic phenomena, including ENSO, North Atlantic Oscillation (NAO), Atlantic Oscillation (AO), QBO) and Pacific Decadal Oscillation (PDO), present also periodicities that coincide with the solar activity cycles (Velasco and Mendoza, 2008), and also affect natural processes directly (Labat, 2010).

The periodicities ~5 years can be a harmonic of the 11-years solar cycle (Djurović and Páquet, 1996) and the periodicity ~8 years could be related to the 11-years sunspot cycle (taking into account the uncertainties). Summarizing, our results indicate a consistent correlation between DMS and SST and an anticorrelation between DMS-UVA. Between DMS-TSI we notice mainly an out of phase situation implying a nonlinear relationship. And the relation between DMS and LCCIR and LCCVIS-IR presents undefined phases indicating that the relation is also non-linear. The anticorrelation between UVA and DMS indicate a positive feedback, as discussed in other works (Larsen, 2005) or as implied by the findings of other papers (Mendoza and Velasco, 2009; Lockwood, 2005; Kristjánsson et al., 2002).

## Conclusions

We studied the relationship between DMS and SST, LCC-IR, LCCVIS-IR, UVA and TSI using the Wavelet Method. We found dominant periodicities that coincide with those of large scale atmospheric phenomena or solar activity, for instance, the periodicities ~2 years can be associated to the Quasi-Biennial Oscillation (QBO) in the stratosphere as this atmospheric phenomenon is related to solar activity, those periodicities ~3 and ~4 years could be associated to the El Niño-Southern Oscillation (ENSO) as large scale climatic phenomena seem also influenced by solar activity, and the periodicities ~5 years can be associated a harmonic of the 11-year solar cycle. The results of the wavelet analysis show an intermittent but sustained correlation (phase) between DMS-SST and an anticorrelation (anti-phase) between DMS-UVA, these two cases indicate a linear relationships because the coherence of the series is high. The relations between DMS and TSI and LCC imply nonlinear relationships. The time-span of the series allow us to study only periodicities shorter than 11years, then we limit our analysis to the possibility that solar radiation influences the Earth climate in periods shorter than the 11-year solar cycle. Our results also suggest a positive feedback interaction between DMS and UVA solar radiation.

## Bibliography

Andreae M.O., Crutzen P.J., 1997, Atmospheric aerosols: biogeochemical sources and role in atmospheric chemistry, *Science* 276, 1052–1058.

Bal S., Schimanke S., Spangehl T., Cubasch U., 2011, On the robustness of the solar cycle signal in the Pacific region, *Geophys. Res. Lett.*, 38, L14809.

Baldwin M.P., Gray L.J., Dunkerton T.J., Hamilton K., Haynes P.H., Randel W.J., Holton J.R., Alexander M.J., Hirota I., Horinouchi T., Jones D.B., Kinnersley J.S., Marquardt C., Sato K., Takahashi M., 2001, The Quasi-Biennial Oscillation, *Reviews of Geophysics*, 39, 2, 179-229.

Charlson R.J., Lovelock J.E., Andreae M.O., Warren S.G., 1987, Oceanic phytoplankton, atmospheric sulfur, cloud albedo and climate: a geophysiological feedback, *Nature*, 326, 655–661.

Chen T., Rossow B.W., Zhang Y., 1999, Radiative effects of Cloud-Type variations, *Journal of climate*, 13.

DeLand M.T., Cebula R.P., 2008, Creation of a composite solar ultraviolet irradiance data set. *J. Geophys. Res*. 113, A11103.

Djurovic D., Páquet P., 1996, The common oscillations of solar activity, the geomagnetic field, and the earth's rotation, *Solar Physics*, 167, 427-439.

Dunkerton T.J., 1997, The role of gravity waves in the quasi-biennial oscillation, *J. Geophys. Res*., 102, 26,053-26,076.

Farge M., 1992, Wavelet transforms and their applications to turbulence, Annual Review of Fluid Mechanics 24, 395-457.

Fröhlich C., 2009, Observational evidence of a long-term trend in total solar irradiance, *Astron. Astrophys*., 501, 27-30.

Gallego D., Ribera P., Garcia-Herrera R., Hernandez E., Gimeno L., 2005, A new look for the Southern Hemisphere jet stream, *Climate Dynamics*, 24, 6, 607-621.

Gilman D.L., Fugliste E.J., Mitchell J.R., 1963, On the power spectrum of Red Noise, *Atmospheric Sciences* 20, 182-184.

Gray L.J., Beer J., Geller M., Haigh J.D., Lockwood M., Matthes K., Cubasch U., Fleitmann D., Harrison G., Hood L., Luterbacher J., Meehl G.A., Shindell D., Van Geel B., White W., 2010, Solar Influences on Climate, *Reviews of Geophysics*, 48, RG4001, 53 PP.

Grinsted A., Moore J., Jevrejera S., 2004, Application of the cross wavelet transform and wavelet coherence to geophysical time series, *Nonlinear Processes in Geophysics* 11, 561-566.

Gunson J.R., Spall S.A., Anderson T.R., Jones A., Totterdell I.J., Woodage M.J., 2006, Climate sensitivity to ocean dimethylsulphide emissions, *Geophys. Res. Lett*. 33, L07701.

Häder D.P., Helbling E.W., Williamson C.E., Worrest R.C., 2011, Effects of UV radiation on aquatic ecosystems and interactions with climate change, *Photochem. Photobiol.Sci*., 242-260.

Häder D.P., Kumar R.C., Smith R.C., Worrest R.C., 2003, Aquatic ecosystems: effects of solar ultraviolet radiation and interactions with other climatic change factors, *Journal of the Royal Society of Chemistry*, 39-50.

Hardman-Mountford N., Hirata T., Richardson K., Aiken J., 2008, An objective methodology for the classification of ecological pattern into biomes and provinces for the pelagic ocean, *Remote Sens. Environ*., 112, 3341-3352.

Hefu Y., Kirst G.O., 1997, Effects of UV radiation on DMS content and DMS formation of Phaeocystis Antartica, *Polar Biol*., 18, 402-409.

Holton J.R., Lindzen R.S., 1972, An updated theory for the Quasi-Biennial cycle of the tropical stratosphere, *Journal of the Atmospheric Sciences*, 29, 1076-1080.

Holton J.R., Tan H.C., 1980, The influence of the equatorial Quasi-Biennial Oscillation on the global atmospheric circulation at 50mb, *Journal of Atmospheric Science*., 37, 2200-2208.

Kane R., 2005, Differences in the quasi-biennial oscillation and quasi-triennial oscillation characteristics of the solar, interplanetary, and terrestrial parameter, *Journal of Geophysical Research,* 110, 13.

Kettle A.J., Andreae M.O., Amouroux D., *et al*., 1999, A global data base of sea surface Dimethylsulfide (DMS) measurements and a procedure to predict sea surface DMS as a function of latitude, longitude and month, *Global Biogeochemical Cycles* 13, 399-444.

Fröhlich C., 2009, Observational evidence of a long-term trend in total solar irradiance, *Astron. Astrophys*., 501, 27-30.

Kirov B., Georgieva K., 2002, Long-term variations and interrelations of ENSO, NAO and solar activity, *Phys. Chem. Earth*, 27, 441-448.

Kniventon D.R., Todd M.C., Sciare J., Mihalopoulos N., 2003, Variability of atmospheric dimethylsulphide over the southern Indian Ocean due to changes in ultraviolet radiation, *Global Biogeochem. Cycles,* 17, 1096.

Kristjánsson J.E., Staple A., Kristiansen J., Kaas E., 2002, A new look at possible connection between solar activity, clouds and climate, *Geophys. Res. Lett.*, 29, 2107.

Labat D., 2010, Cross wavelet analysis of annual continental freshwater discharge and selected climate indices, *J. Hydrol.*, 385, 269–278.

Labitzke K., 1987, Sunspots, the QBO and the stratospheric temperature in the north polar region, *Geophys. Res. Lett.*, 14, 535-537.

Labitzke K., van Loon H., 1992, On the association between the QBO and the extratropical stratosphere, *J. Atmos. Terr. Phys.*, 54, 1453–1463.

Labitzke K., Kunze M., 2012, Interactions between the stratosphere, the sun and the QBO during the northern summer, *Journal of Atmospheric and Solar-Terrestrial Physics,* 141, 75-76.

Larsen S.H., 2005, Solar variability, dimethylsulphide, clouds and climate, *Global Biogeochem. Cycles*, 19, GB1014.

Lean J.R., Lee G.J., Woods H., Hickey T.N., Puga J., 1997, Detection and parameterization of variations in solar mid- and near-ultraviolet radiation (200–400 nm), *Geophys. Res. Lett.* 102, 939-956.

Lockwood M., 2005, Solar outputs, their variations and their effects on Earth, in The Sun, Solar Analogs and the Climate, Saas-Fee Advanced Course, 34, 109-306, Springer, the Netherlands.

Longhurst A., Sathyendranath S., Platt T., Caverhill C., 1995, An estimate of global primary production in the ocean from satellite radiometer data, *J. Plankton Res.*, 17, 1245-1271.

Mendoza B., García-Acosta V., Velasco V., Jáuregui E., Díaz-Sandoval R., 2007, Frequency and duration of historical droughts from the 16th to the 19th centuries in the Mexican Maya lands, Yucatan Peninsula. Climatic Change.

Mendoza B., Velasco V., 2009, High-Latitude Methane Sulphonic Acid Variability and Solar Activity. *J. Atm. and Solar-Terr. Phys.,* 71, 33-40.

Miller A.J., Alexander M.A., *et al*. 2003, Potential feedbacks between Pacific Ocean ecosystems and interdecadal climate variations, *Bull. Am. Meteorol. Soc.,* 84, 617-633.

Mufti S., Shah G.N., 2011, Solar-geomagnetic activity influence on Earth's climate, *J. Atmos. Solar Terr. Phys.,* 73, 13, 1607-1615.

Naujokat B., 1986, An update of the observed Quasi-Biennial Oscillation of stratospheric winds over the tropics, *Journal of the Atmospheric Sciences*, 43, 1873-1877.

Njau E.C., 2006, Solar activity, El Niño-Southern oscillation and rainfall in India, Pakistan *Journal of Meteorology*, 3.

Nuzhdina M.A., 2002, Connection between ENSO phenomena and solar and geomagnetic activity, *Natural Hazards and Earth System Sciences*, 83-89.

Pidwirny M., 2006, Upper Air Winds and the Jet Streams, Fundamentals of Physical Geography, 2nd Edition.

Polygiannakis J., Preka-Papadema P., Moussas X., 2003, On signal noise decomposition of time series using the continuous wavelet transform: application to sunspot index, Mon. Not. R. Astron. Soc., 343, 725–734.

Ricchiazzi P., Yang S., Gautier C., Sowle D., 1998, SBDART: A Research and teaching software tool for plane-parallel radiative transfer in the Earth's atmosphere, *Bull. Amer. Meteor. Soc.* 79, 2101-2114.

Roy I., Haigh D., 2011, The influence of solar variability and the quasi-biennial oscillation on sea level pressure, *Atmos. Chem. Phys. Discuss.*, 10, 30452-30471.

Rossow W.B., Schiffer R.A., 1999, Advances in understanding clouds from ISCCP, *Bull. Am. Meteor. Soc.* 80, 2261-2287.

Sarmiento J.L., Gruber N., Brzezinski M.A., Dunne J.P., 2004, High-latitude controls of thermocline nutrients and low latitude biological productivity, *Nature*, 427, 6969, 56-60.

Savitskiy G., Lessing, V., 1979, Tropospheric jet streams in the Antarctic, *Polar Geography*, 3, Iss. 3.

Shaw G.E., Benner R.L., Cantrell W., Veazey D., 1998, The regulation of climate: A sulfate particle feedback loop involving deep convection-An editorial essay, *Climate Change* 39, 23–33.

Simó R., 2001, Production of atmospheric sulfur by oceanic plankton: biogeochemical, ecological and evolutionary links, *Trends in Ecology and Evolution*, 16, 287–294.

Simó R., Dachs J., 2002, Global ocean emission of dymethylsulfide predicted from biogeophysical data, *Global Biogeochem. Cycles*, 16.

Simó R., Vallina S.M., 2007, Strong relationship between DMS and the solar radiation dose over the global surface ocean, *Science*, 315, 506-508.

Slezak D., Herndl G.J., 2003, Effects of ultraviolet and visible radiation on the cellular concentration of dimethylsulfoniopropionate (DMSP) in Emilianiahuxleyi (strain L), Mar. Ecol. Prog. Ser. 246, 61-71.

Toole D.A., Slezak D., Kiene R.P., Kieber D.J., 2006, *Effects of solar radiation on dimethylsulfide cycling in the western Atlantic Ocean*, Deep-Sea Res. I, 53, 136-153.

Toole D.A., Siegel D.A., 2004, *Light-driven cycling of Dimethylsulfide (DMS) in the Sargasso Sea: Closing the Loop*, Geophys. Res. Lett., 31-9.

Torrence C., Compo G.B., 1998, *A practical guide to wavelet analysis*, Amer. Meteor. Soc. 79, 61-78.

Valdés-Galicia J., Velasco V., 2008. *Variations of mid-term periodicities in solar activity physical phenomena*, Advances in Space Research 41, 297-305.

Vallina S.M., Simó R., Gassó S., DeBoyer-Montégut C.D., Jurado E., Dachs J., 2007,

Analysis of a potential "solar radiation dose-dimethylsulfide-cloud condensation nuclei" link from globally mapped seasonal correlations, *Global Biogeochem. Cycles,* 21.

Velasco V., Mendoza B., 2008, Assessing the relationship between solar activity and some large scale climatic phenomena, *Advances in Space Research,* 42, 866–878.

Weng H., 2005, The influence of the 11 yr solar cycle on the interannual-centennial climate variability, *J. Atmos. Solar Terr. Phys.*, 67, 793–805.

Weng H., 2012, Impacts of multi-scale solar activity on climate. Part II: Dominant timescales in decadal-centennial climate variability, *Advances in Atmospheric Sciences*, 29, 887-908.

# H/V spectral ratio analysis and Rayleigh modelization in Eastern Thuringia, Germany

Hortencia Flores[*], Peter Malischewsky and Gerhard Jentzsch

## Resumen

Usamos registros de algunas estaciones de la base de datos de la OTSN para caracterizar su respuesta de sitio y para analizar los límites y alcances del modelado de Rayleigh para los cocientes espectrales H/V.

Las estaciones que consideramos en este trabajo pueden ser agrupadas, según su respuesta sísmica, como sitios en roca dura y como sitios con algún efecto de sitio. A partir de estos resultados proponemos modelos de velocidades que están basados en el modelado de Rayleigh (cálculo de la elipticidad teórica).

Los resultados muestran que para los sitios con algún efecto de sitio los cocientes espectrales H/V pueden ser modelados a partir del cálculo de la elipticidad teórica de un modelo de velocidades. Sin embargo, para los sitios en roca dura, en los que los cocientes espectrales son bastante planos, el modelado a partir de la elipticidad teórica de ondas de Rayleigh no resuelve de manera satisfactoria. Esto puede deberse a que las condiciones generales para que los cocientes H/V proporcionen un pico definido, cercano a la frecuencia fundamental de resonancia de ondas S, y por tanto que este pico se pueda asociar con una medida de la elipticidad de las Ondas de Rayleigh no se cumple en sitios de roca dura.

Palabras clave: modelado de Ralyleigh, cocientes espectrales H/V.

## Abstract

We use records from the East Thuringian Seismic Network (OTSN, Ostthüringer Seismisches Netzwerk) to characterize the site response for each station, and to analyze the scope and limits of the Rayleigh modeling for H/V spectral ratio.

The stations considered in this work can be classified by their seismic response as hard rock sites or as sites with some site effect. From these results we propose velocity models based on Rayleigh modeling (theoretical Rayleigh wave ellipticity).

Our results show that for locations affected by site effects the H/V spectral ratio can be modeled by the theoretical ellipticity of layered velocity models. For hard rock sites the spectral ratio is rather flat and the modeling with the theoretical ellipticity was not very clear. This may be explained by the fact that for hard rock sites the conditions for a clear fundamental frequency associated with S-wave resonance, and therefore with Rayleigh wave ellipticity, are not fulfilled.

Key words: Rayleigh modeling, H/V spectral ratio.

H. Flores[*]
Institut für Geophysik und Geologie
Universität Leipzig
Talstrasse 35, 04103
Leipzig, Germany
*Corresponding author: hortencia.flores@uni-leipzig.de

P. Malischewsky
G. Jentzsch
Institut für Geowissenschaften
Friedrich-Schiller-Universität Jena

## Introduction

Seismic noise can be analyzed in different ways depending on the objective of the study (Chávez-García, 2009). A popular analysis method is the H/V spectral ratio method. This method was first proposed by Nogoshi and Iragashi (1971) and years later it was summarized by Nakamura (1989). During the decade of the 1990´s almost 80% of published works about seismic noise were using the H/V spectral ratio method (Bard, 1998; Bonnefoy-Claudet et al., 2006).

It is widely accepted that this method can provide reliable estimates of S wave resonant frequency, especially in places with large amplification and simple subsoil geology (Bard, 1998; Chavez-García, 2009; SESAME, 2004; Bonnefoy-Claudet et al., 2006; Malischewsky and Scherbaum, 2004). However, it is also accepted that a theoretical model for the interpretation of the H/V measurements from seismic noise still has to be developed and analyzed.

One way to interpret the H/V spectral ratios is to assume that the seismic field is diffuse and contains all types of elastic waves, therefore the H/V spectral ratio could be computed in terms of the imaginary part of the Green's Function (Kawase et al., 2011; Sánchez-Sesma et al., 2011a; Sánchez-Sesma et al., 2011b).

On the other hand, Malischewsky and Scherbaum (2004) proposed that H/V spectral ratios could be modeled as measurements of Rayleigh wave ellipticity, assuming that seismic noise is dominated by surface waves. They propose an exact formula to calculate the theoretical ellipticity for a given velocity model, which can be either a single layer over a half-space or a multilayered model (Malischewsky et al., 2010; Tran et al., 2011). The same authors have discussed the conditions required to model H/V spectral ratios in terms of theoretical ellipticity, with special emphasis on velocity contrast and values of the Poisson ratio v.

In this study, we use data from some stations of the East Thuringian Seismic Network, OTSN, and we discuss H/V spectral ratios modeling in terms of theoretical Rayleigh wave ellipticity. We show and discuss the results for noise records and for explosion events from the mining district of Western Silesia, Poland and from Thuringia, in Germany. The local seismic events from Thuringia cannot be used because they are deep and produce no surface waves.

As a first step we classify the stations from the OTSN according to their seismic response as defined by the H/V spectral ratios. Then we suggest some velocity models following Malischewsky and Scherbaum (2004), Malischewsky et al. (2010) and Tran et al. (2011), to discuss the possibilities of this modeling.
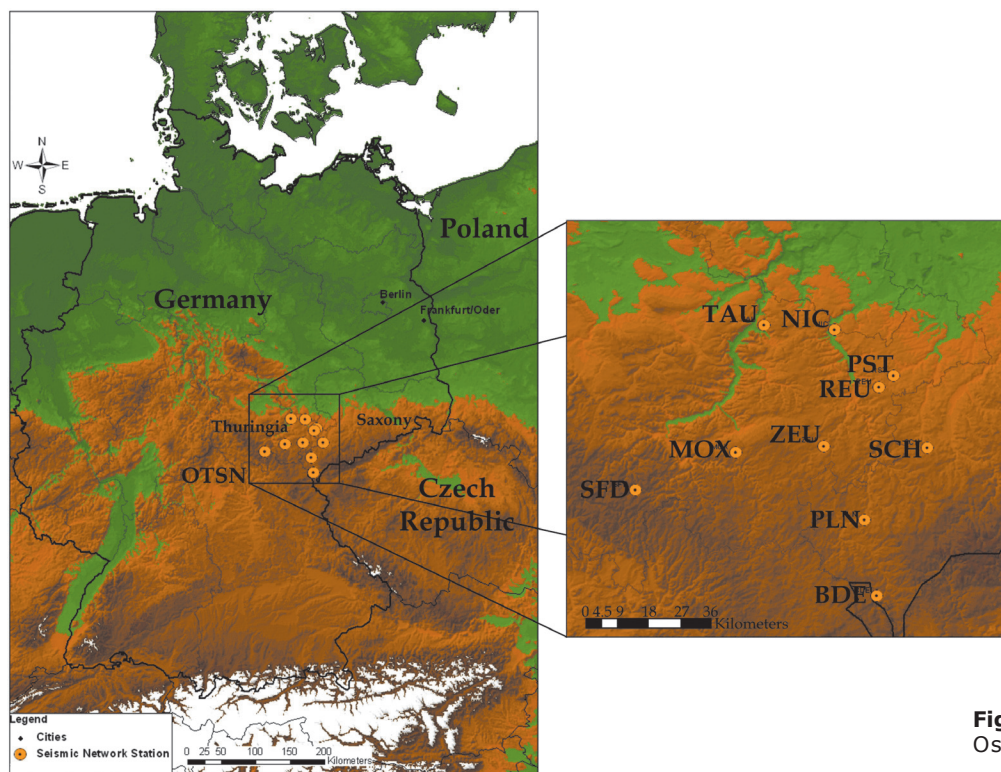


**Figure 1.** Location of the Ost Thuringian Seismic Network stations.

**Table 1.** Location of the OTSN stations.

| Station code | Town | Lat °N | Long °E | Altitude (m) |
|---|---|---|---|---|
| BDE | Bad Elster | 50.29 | 12.22 | 420 |
| MOX | Moxa | 50.65 | 11.62 | 455 |
| NIC | Nickelsdorf | 50.98 | 12.01 | 250 |
| PLN | Plauen | 50.49 | 12.16 | 432 |
| PST | Posterstein | 50.86 | 12.26 | 270 |
| REU | Reust | 50.83 | 12.19 | 454 |
| SCH | Schönfels | 50.68 | 12.40 | 435 |
| SFD/SCHD | Schmiedefeld | 50.54 | 11.21 | 761 |
| TAU | Tautenburg | 50.98 | 11.71 | 330 |
| ZEU | Zeulenroda | 50.67 | 11.98 | 331 |

**The East Thuringian Seismic Network (OTSN)**

The OTSN (Figure 1, Table 1) was installed in 1997 to investigate local seismicity and its relation with the stress field, recent tectonics and the local crustal structure, and to estimate seismic risk in Eastern Thuringia (Kracke *et al.,* 2000).

Most of the stations are located on rock outcrops, sometimes with a thin sedimentary layer. Therefore, some stations may have site effects which are not important in terms of motion amplification, but they yield a good opportunity to test H/V spectral ratio in terms of theoretical ellipticity.

We worked with the OTSN database in the period from 2000 to 2006. During this period the OTSN does not provide continuous records. In the first stage of the study we selected records which did not contain any seismic event but only seismic noise. In a second stage we used the software developed by Tran *et al.* (2011) to obtain Rayleigh wave theoretical ellipticity for a given velocity model and to compare this solution with the actual H/V spectral ratio. Finally, we present some preliminary results of H/V spectral ratio analysis for explosions from the mining district of Western Silesia (Poland) and from Thuringia (Germany).

We selected those stations with most stable behavior in terms of spectral ratios: BDE, MOX, PLN, NIC and REU.

*Noise analysis*

For each month of the analysis we selected those records with noise data. Figure 2 shows the number of records analyzed per year. For year 2005 we had the largest quantity of noise records, but the most representative of our analysis for the whole period are those for year 2004. In the next sections we show the results for this year, meaning that each of the spectral ratio curves corresponds to a monthly average during the year 2004.

For each selected file we used three 20 seconds windows considered from the beginning of the record with 20% overlap. This analysis section was done with Seisan (Ottemöller *et al.*, 2011).

*Noise H/V spectral ratio results*

From the results of the spectral ratio we may classify the OTSN stations according to their site response into two groups:

Group I. The spectral ratio amplitudes are close to one from 0.1 to 10 Hz. We propose that these amplitudes correspond to stations on bedrock. This group includes MOX, BDE and PLN (Figure 3).
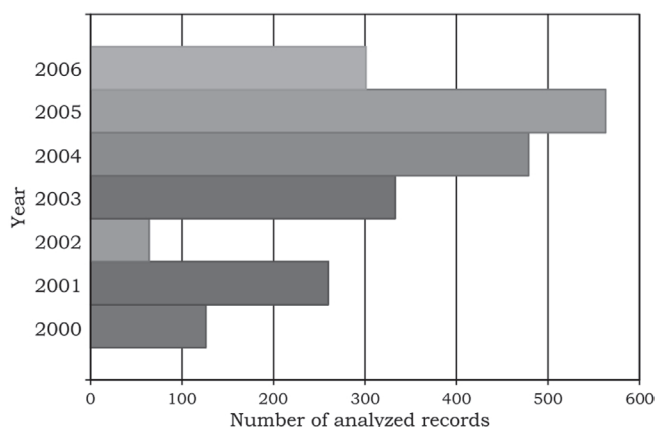


**Figure 2.** Number of records analyzed per year.

Group II. The spectral ratios show at least one well defined peak. The stations in this group are REU and NIC (Figure 4). These stations, though on bedrock have a thin sedimentary layer which causes a small site effect (low amplitude) in the seismic response. But it also implies a contrast on the physical properties.

In Figure 3 the spectral ratio at BDE is quite stable in both components; the amplitude is close to one for up to 1 Hz and then increases, reflecting anthropogenic activities. At MOX, although the amplitude is also close to one in most part of the spectrum, the H/V ratio has a small peak between 3 and 5 Hz, although the amplitude is not important. Finally, for PLN the spectral ratio amplitude is close to one up to 1 Hz and then it increases reflecting anthropogenic activity.

For stations in Group II (Figure 4), the station NIC shows a similar behavior in the spectral ratio of the two components: in both cases we found a fundamental frequency at 1.46 Hz with amplitude of 2.7, and then the spectral ratio display three peaks at: 2.82, 3.8 and about 5 Hz, with amplitudes between 1.5 and 1.8. As mentioned in Malischewsky *et al.* (2010), this may be due to the value of Poisson's ratio for the shallower layers of the velocity structure.

For station REU, it is not easy to define the fundamental frequency; rather we can define a plateau between 1 and 3 Hz, where the amplitude is close to 3. Later, between 6 and 7 Hz a peak is observed with amplitude of about 2.

*Theoretical Ellipticity*

Assuming that the noise wavefield is dominated by surface waves, the H/V spectral ratio would measure the Rayleigh wave ellipticity. Some conditions have to be fulfilled in order to have a good coincidence between the fundamental frequency of the H/V spectral ratio (main peak) and the singularity of the theoretical ellipticity.

Considering a layer over a half space model the velocity contrast must be higher than 3.5; and the ratio $d/\lambda_{\beta 1}$ must be fulfilled, where $d$ is the thickness of the layer and $\lambda_{\beta 1}$ is the wavelength in the layer (Scherbaum *et al.*, 2003; SESAME, 2004; Malischewsky and Scherbaum, 2004; Tran *et al.*, 2011).

Malischewsky and Scherbaum (2004) presented an exact formula to calculate the theoretical ellipticity of Rayleigh waves for a single layer over a half-space model. The theory for layered models was later proposed by Malischewsky *et al.* (2010) and Tran *et al.* (2011).
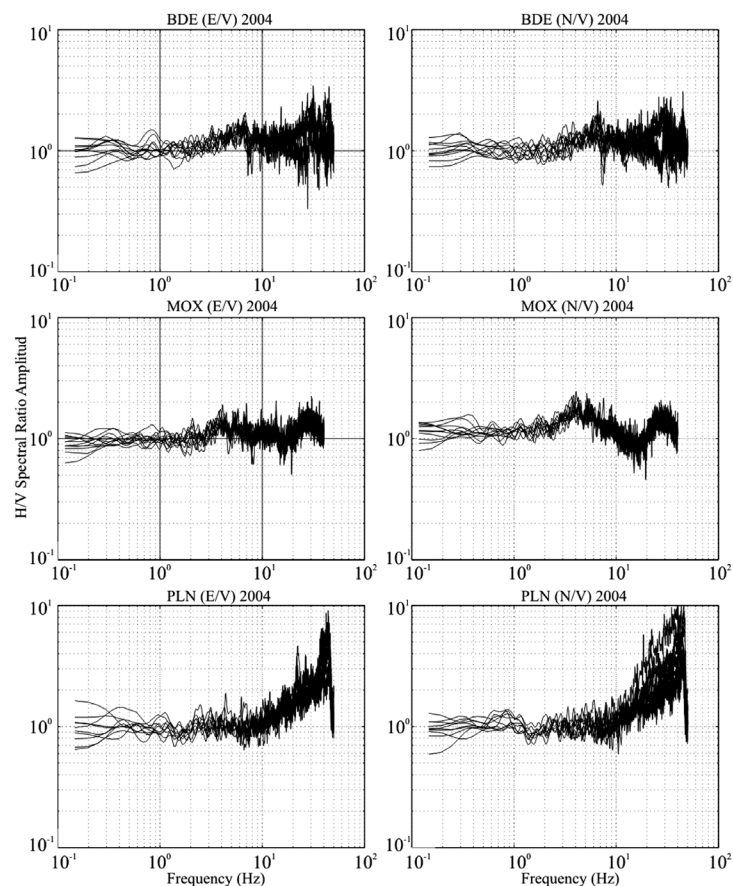


**Figure 3.** Noise H/V spectral ratio for the 12 months of 2004. Stations in Group I: BDE, MOX and PLN. Each line corresponds to the monthly average spectral ratio.

**Figure 4.** Noise H/V Spectral ratio for the 12 months of 2004. Stations in Group II: NIC and REU. Each line corresponds to the monthly average.
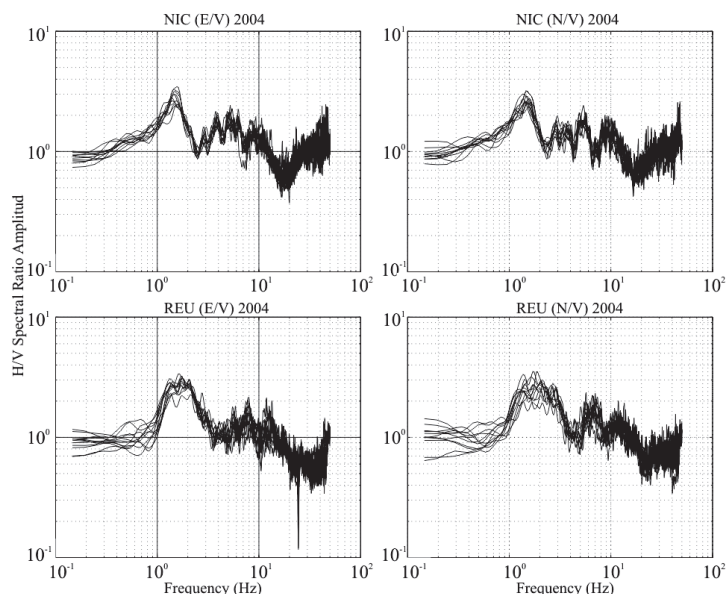


In some cases the H/V spectral ratio might show more than one peak after the main peak (as in NIC station, Figure 4). Malischewsky *et al.* (2010) propose that the following maximum may be associated with deeper layers resonance frequencies. In addition, Tran *et al.* (2011) report that for special Poisson's ratio two peaks of the theoretical ellipticity may exist for a model with a layer over a half-space.

Considering the conditions for the physical parameters described above and previous velocity models for the OTSN stations, obtained by the geological conditions and by the models used to locate the local earthquakes, we propose velocity models for the stations we worked with and in some cases modified them by trial and error to adjust the observed H/V spectral ratio. We show and discuss the results for the stations classified into the two groups previously defined.

In Table 2 we show the velocity profiles for the stations on Group I and on Figure 5 the H/V spectral ratio and with thick red line the theoretical ellipticity for the velocity models of each station from this group.

The stations in Group I are characterized by a quite flat seismic response within a large frequency interval. This implies that there might not be a large impedance contrast between the shallower layers and the basement.

However, on Figure 5 we can see that Rayleigh modeling fits well below 1 Hz. The difference between the ratios of the horizontal component may be due to directional noise sources that affect more one motion direction than the other. This problem could be solved using the combination of the horizontal motion components before calculating the H/V spectral ratio (SESAME, 2004). We still consider both horizontal components separately to characterize the differences in them.

For station PLN the behavior in high frequencies is probably due to anthropogenic activities and more exploration on this effect is beyond the scope of this work.

In Table 3 we show the velocity models for the stations NIC and REU in group 2. For station REU we propose a more detailed velocity model because the H/V spectral ratio is more like a

**Table 2.** Velocity models for the station in Group II.

| Station code | Thickness (m) | ρ (gr/cm3) | β (m/s) | ν |
|:---:|:---:|:---:|:---:|:---:|
| BDE | 12.86 | 2.2 | 350 | 0.22 |
|  | ∞ | 2.7 | 875 | 0.28 |
| MOX | 21 | 2.2 | 350 | 0.25 |
|  | ∞ | 2.7 | 875 | 0.3 |
| PLN | 30 | 2.2 | 600 | 0.2 |
|  | ∞ | 2.7 | 900 | 0.25 |
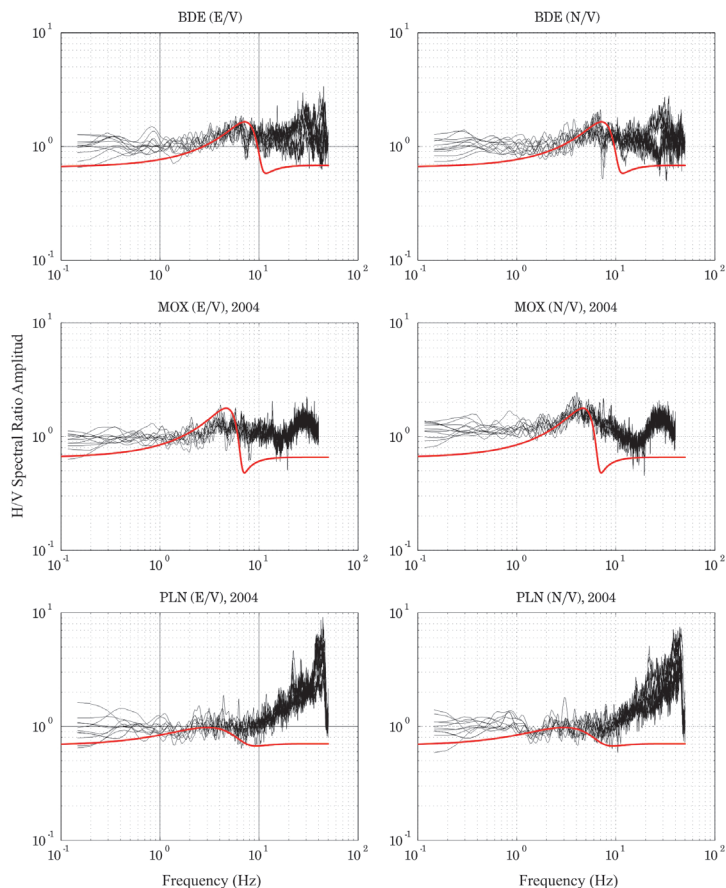
**Figure 5.** H/V spectral ratio for BDE, MOX and PLN for year 2004 and with thick red line the theoretical ellipticity of the models showed in table 1.

*plateau*. In Figure 6 we show the H/V spectral ratio for stations NIC and REU and with a thick red line the theoretical ellipticity for the velocity models in table 2. As we can see in Figure 6 the fit between the H/V spectral ratio and the theoretical ellipticity for the station NIC is good for the fundamental frequency, in terms of shape and amplitude. For station REU the fitting is also good considering the *plateau* shape and that there is not a single fundamental frequency.

The peaks in higher frequencies in both stations require more attention to be modeled as they can be related to higher propagation modes.

*Explosion events Coda H/V spectral ratio*

Explosion seismic events due to mining activities are quite superficial and rich on surface waves.

Therefore, we selected five of these events (Table 4): three coming from Western Silesia mining district, in Poland, and two coming from Thuringian mining area, in Germany. In Figure 7 we show the location of these events. In Figure 8 we show the record for event WPOL01 in the stations of the OTSN and the windows we used containing surface waves.

In Figure 9 we show a comparison between the H/V spectral ratio from noise data *vs.* the spectral ratio from explosion events for MOX and NIC stations. For MOX station we can see that the spectral ratios for explosion events are quite similar to those from noise data. For NIC station, though the behavior is also quite similar the fundamental frequency is not so clear, especially for those events coming from Western Silesia. For these events we can see that low frequencies are

**Table 3.** Velocity models for the stations in Group II.

| Station code | Thickness (m) | ρ (gr/cm3) | β(m/s) | ν |
|---|---|---|---|---|
| NIC | 58 | 2.2 | 300 | 0.25 |
| | ∞ | 2.7 | 1050 | 0.25 |
| REU | 28 | 1.7 | 250 | 0.26 |
| | 30 | 1.8 | 650 | 0.12 |
| | 120 | 1.9 | 900 | 0.1 |
| | ∞ | 2.2 | 1900 | 0.25 |

**Figure 6.** H/V Spectral ratio for NIC and REU for the year 2004 and with thick red line the theoretical ellipticity for the models showed in table 2.
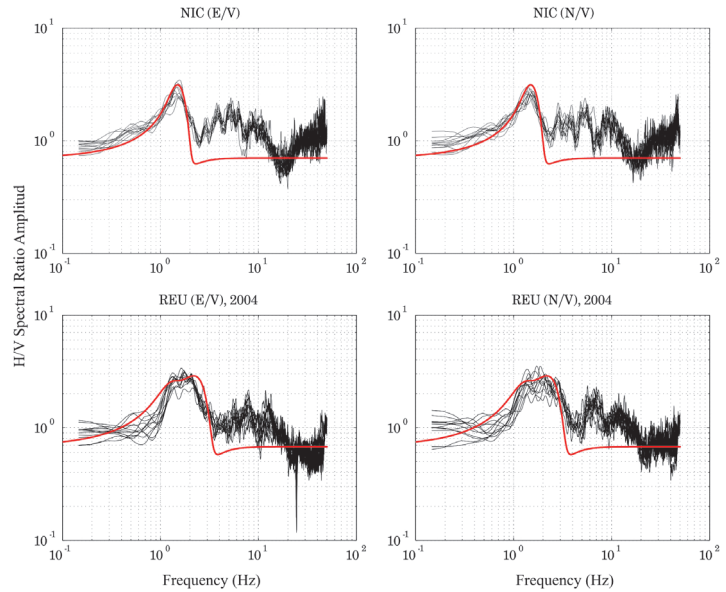


**Figure 7.** The stars show the locations of the events from Western Silesia, Poland (WPOL01 and WPOL02) and from Thuringia (THUR01-THUR05) as well as the location of the OTSN stations with yellow points.
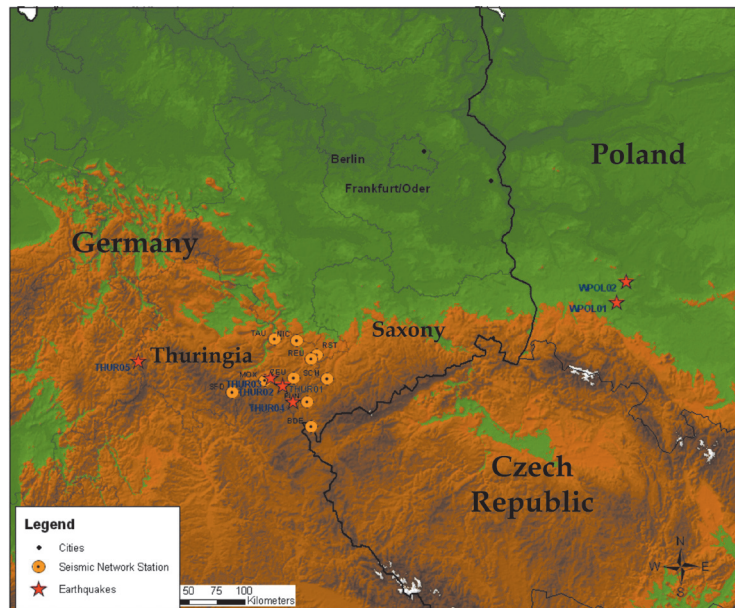


**Table 4.** Date, time and location for explosion events. WPOLXX refers to events from Western Silesia, Poland; and THURXX refers to events from Thuringia, Germany.

| Explosion events | Date (dd.mm.yyyy) | Time (hh:mm:ss) | Lat N | Lon E |
|---|---|---|---|---|
| WPOL01 | 25.09.2004 | 15:48:18 | 51.325 | 16.082 |
| WPOL02 | 26.09.2004 | 19:32:23 | 51.489 | 16.202 |
| THUR01 | 02.04.2004 | 12:22:04 | 50.617 | 11.843 |
| THUR02 | 06.05.2004 | 11:58:11 | 50.613 | 11.842 |
| THUR03 | 08.07.2004 | 12:06:02 | 50.673 | 11.683 |
| THUR04 | 30.11.2004 | 14:20:06 | 50.489 | 11.985 |
| THUR05 | 22.09.2005 | 04:00:00 | 50.750 | 10.007 |
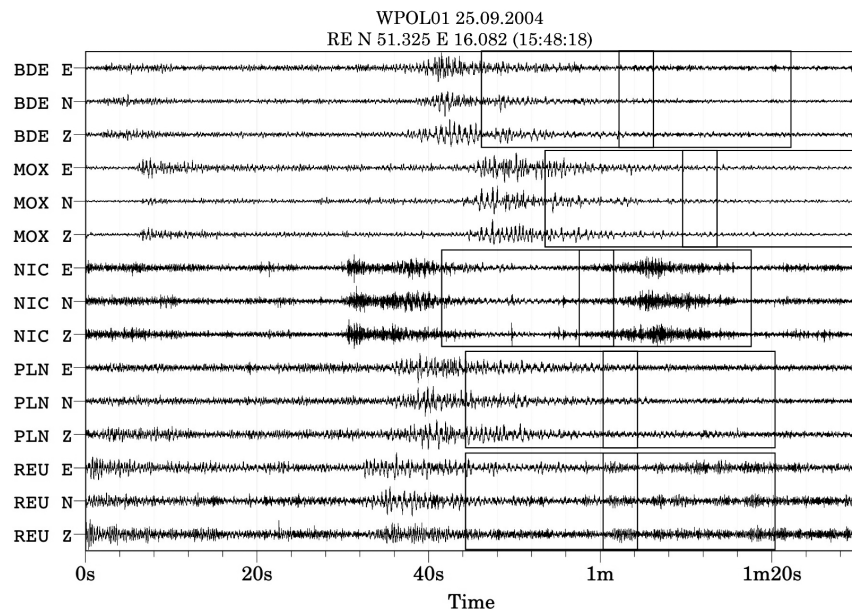
**Figure 8.** Time record for the event WPOL01. The dotted lines indicate the 20 sec windows considered for the H/V spectral ratios.
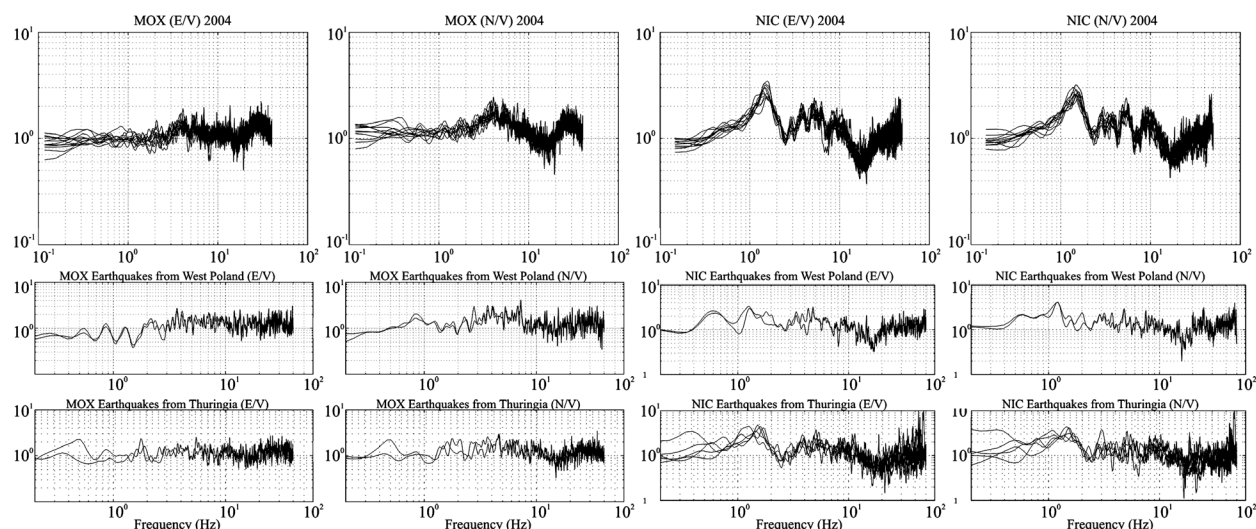


**Figure 9.** H/V spectral ratio results for the stations MOX and NIC for noise data (top), explosion events in West Poland (middle) and in Thuringia (bottom).

more excited. It would require analyzing more explosion events for these stations to find out if there is coincidence with noise H/V spectral ratio or not.

## Conclusions

From the analysis of the OTSN data base from 2000 to 2007, we obtained the seismic response for some of the stations. We defined two groups in terms of H/V spectral ratio results: group I formed by stations BDE, MOX and PLN, characterized by a flat spectral ratio in most of the frequency interval. For station PLN we interpret the amplitude

increase in frequencies higher than 1Hz as due to anthropogenic activities. Stations in group II, NIC and REU, are characterized by small site effects (motion amplification) either in a single frequency (NIC) or in a *plateau* (REU).

For stations in Group I there is not a big velocity contrast between the layer and the half space; therefore the H/V spectral ratio does not show a clear fundamental frequency. This also implies certain difficulties to model the spectral ratio in terms of theoretical ellipticity. However, we could model some part of them with acceptable results below 1 Hz.

On the other hand, for stations in Group II we have two different behaviors. First, the classic one with a well-marked fundamental frequency at station NIC; though it also shows some more maxima in higher frequencies that can be due to surface waves higher modes or also to Poisson's ratio conditions that could not be modeled. These maxima in higher frequencies were also found in the spectral ratio for station REU; however for this station the plateau shape of the spectral ratios shows also that the velocity contrast is not high.

The results for the spectral ratio from explosion events are quite similar to those from noise records. However, the possibility of using surface waves from explosion events has to be more explored and this would be a good opportunity to use the data from the actual Thuringian Seismic Network (TSN), which has continuous records.

The stations of the OTSN were installed to measure small regional and local earthquakes; therefore they were supposed not to show any site effect. Probably the same kind of analysis using data from places with a known and strong site effect (due to geological conditions) would enlighten more the scope of the H/V spectral ratio modeling in terms of theoretical ellipticity.

## Acknowledgements

## Bibliography

Bard P.Y., 1998, Microtremor Measurements: A Tool for site effect estimation?. The Effects of Surface Geology on Seismic Motion, Irikura, Kudo, Okada and Sasatani (eds), 1251-1279.

Bonnefoy-Claudet S., Cotton F., Bard P.Y., 2006, The nature of noise wavefield and its applications for site effects studies. A literature review. *Earth Science Reviews*, 79, 205-227.

Chávez-García F.J., 2009, Ambient noise and Site response: from estimation of site effects to determination of the subsoil structure, in Mucciarelli *et al*., eds., 2009, Increasing Seismic Safety by combining Engineering Technologies and Seismological Data, NATO Science for Peace and Security Series, Springer Science Business Media.

Kawase H., Sánchez-Sesma F.J., Matsushima S., 2011, The Optimal Use of Horizontal-to-Vertical Spectral Ratios of Earthquake Motions for Velocity Inversion Based on Diffuse-Field Theory for Plane Waves. *Bull. Seismo. Soc. Am*. 101, 5, 2001-2014.

Kracke D., Heinrich R., Hemmann G. Jentzsch A., Ziegert A., 2000, The East Thuringian Seismic Network, *Studia Geophysica et Geodaetica*, 44, 4, October 2000, 594-601, 8.

Malischewsky P., Scherbaum F., 2004, Love´s formula and H/V-ratio (ellipticity) of Rayleigh waves. *Wave Motion*, 40, 57-67.

Malischewsky P., Zaslavsky Y., Gorstein M., Pinsky V., Tran T.T., Scherbaum F., Flores-Estrella H., 2010, Some new theoretical considerations about the ellipticity of Rayleigh waves in the light of site effect studies in Israel and Mexico. *Geofísica Internacional*, 49, 141-152.

Nakamura Y., 1989, A Method for Dynamic Characteristics Estimation of Subsurface using Microtremors on Ground Surface. Quarterly Report of Railway Technical Research Institut (RTRI), 30, 1.

Nogoshi M., Igarashi T., 1971, On the Amplitude and Characteristics of Microtremor (Part 2). In Japanese with English Abstract, *Jour. Seism. Soc. Japan*, 24, 26-40.

Ottemöller L., Voss P., Havskov J., 2011, SEISAN Earthquake Analysis Software for Windows, Solaris, Linux and MacOSX.

Sánchez-Sesma F.J., Weaver R.L., Kawase H., Matsushima S., Luzón F., Campillo M., 2011a, Energy Partitions among Elastic Waves for Dynamic Surface Loads in a Semi-Infinte Solid. *Bull. Seismo. Soc. Am*. 101, 4, 1704-1709.

Sánchez-Sesma F.J., Rodríguez M., Iturrarán-Viveros U., Luzón F., Campillo M., Margerin L., García-Jerez A., Suárez M., Santoyo M.A., Rodríguez-Castellanos A., 2011b A theory for microtremor H/V spectral ratio: application for a layered medium. *Geophys. J. Int.* 186, 221-225.

SESAME, 2004, Guidelines for the implementation of the H/V spectral ratio technique on ambient vibrations. Measurements, processing and interpretation SESAME European research project, deliverable D23.12.

Scherbaum F., Hinzen K.G., Ohrnberger M., 2003, Determination of shallow shear wave

velocity profiles in the Cologne/Germany area using ambient vibrations, *Geophys. J. Int.*, 152, 597-612.

Tran T.T., Scherbaum F., Malischewsky P., 2011, On the relationship of peaks and troughs of the ellipticity (H/V) of Rayleigh waves and the transmission response of single layer over half space models, *Geophys. J. Int.*, 184, 793-800.

# A geostatistical re-interpretation of gravity surveys in the Yagoua, Cameroon region

Philippe Njandjock Nouck*, Chamberlin Kenfack, Ahmad Diab Diab, Kasi Njeudjang, Larissa Jorelle Meli'I and Rodrigue Kamseu

## Resumen

Desde 1960 se han realizado diversos estudios de gravedad en la región Yagoua del norte de Camerún. Se recabaron datos de gravedad en una área amplia que abarca aproximadamente 11.628 km². Estos datos son insuficientes, irregulares, dispersos y no permiten eficientemente continuaciones ascendentes y descendentes del campo gravitatorio, derivadas y otras operaciones que requieren datos reticulados regulares. Algunas anomalías en el mapa Collignon (1968) pueden correlacionarse con la estructura geológica que se conoce, pero no aparecen en los mapas de Louis (1970) y Poudjom et al. (1996). Para producir los datos de gravedad reticulares regulares y mejor control de las anomalías, derivadas de estructuras geológicas, se aplicó el método de Kriging a una línea de base de datos-188. Se ensayaron para este propósito varios modelos de variograma. Se encontró que un modelo esférico era la mejor opción; se ha elaborado un nuevo conjunto de datos Kriging con unos 10.100 resultados y un nuevo mapa con los datos Kriged Bouguer. Este mapa contiene anomalías positivas en las zonas Maroua-Mindif y Maga (1968) en el mapa Collignon, que no estaban presentes en los mapas de Louis (1970) y Poudjom et al. (1996). Las anomalías positivas de Guibi-Doukoula y Yagoua, que no se encuentran separados en los mapas de Louis (1970) y Poudjom et al. (1996), aparecen claramente distintas a como fueron previstas por Collignon (1968). Los nuevos resultados pueden ser utilizados para los estudios gravimétricos posteriores.

Palabras clave: Anomalía Bouguer, datos de gravedad, geoestadística, variograma, Kriging, Yagoua.

## Abstract

Since 1960, many gravity studies have been carried out in the Yagoua region of northern Cameroon. Gravity data was collected over a wide area of approximately 11628 km². These data are insufficient, irregular, scattered and do not efficiently permit gravity field downward and upward continuations, derivatives and other operations that might require regular gridded data. Some anomalies on the Collignon map (1968), may correlate with known geological structure but do not appear on maps by Louis (1970) and Poudjom et al. (1996). To produce regular gridded gravity data and better control anomalies due to geological structures, the kriging method was applied to a 188-data baseline. Several variogram models were tested for this purpose. It was found that a spherical variogram model is the best; it has produced a new kriging dataset of about 10,100 data and a new map of kriged Bouguer data. This map contains positive anomalies in the Maroua-Mindif and Maga areas on the Collignon (1968) map, which were not present on Louis (1970) and Poudjom et al. (1996) maps. The positive anomalies of Guibi-Doukoula and Yagoua, not separated on the Louis (1970) and Poudjom et al. (1996) maps, show up as clearly distinct as previewed by Collignon (1968).The new results can be used for subsequent gravimetric studies.

Key words: Bouguer anomaly, gravity data, geostatistics, variogram, kriging, Yagoua.

P. Njandjock Nouck*
Chamberlin Kenfack
Department of Physics
Faculty of Science
University of Yaoundé I
Cameroon
*Corresponding author:

A. Diab Diab
Department of Physics
Faculty of Science
University of Abeché
Chad

K. Njeudjang
Pecten oil and gas Company
Douala, Cameroon

L. Jorelle Meli'I
Departments of Physics
Advanced Teachers Training College of
Nkolnda-Nsimalen, Cameroon

R. Kamseu
Centre de Formation spécialisée
de Géostatistique MINES-Paris
France

P. Njandjock Nouck, C. Kenfack, A. Diab Diab, Kasi Njeudjang, L. Jorelle Meli'I and R. Kamseu

## Introduction

Geostatistics is applied in the Earth sciences as an interpolation procedure that uses an available dataset to obtain an optimal, linear and unbiased estimation of a property whose estimation error is minimized (Matheron, 1973). It operates on a random variable for which a set of possible values is known but whose final result requires a measurement. The objective of this study is to re-examine a gravity data set from irregular gridded data. For this operation known as kriging, we make a crucial choice of a variogram. This is a better choice, because more kriged values are closer to reality. The principal difficulty is to find a variogram model that fits the data to be interpolated. In this work, we calculate an experimental variogram from existing gravity data, we evaluate the RMS between the variogram and we use various cross-data validation criteria to ensure that the variogram model chosen is optimal in order to correlate with the experimental variogram. We also offer a new gravity dataset and we propose a new gravity map of the Yagoua region in northern Cameroon.

## Study area and Gravity data

### Presentation of the study area

Yagoua region (Figure 1), as others in Central-Africa, is the product of a complex period of continental disruption associated to plate tectonic fragmentation of Gondwana (Genik, 1992; Njandjock, 2004). It is characterised by polyphase rifting, separated by tectonic events that can be linked to regional deformation, hiatus of sedimentation and unconformities in seismic sections and outcrops. The region belonging to the Panafrican belt, is bounded to the South by the Doba basin, to the North by Lake Chad basin, to the East by Doseo and Salamat basins, and to the North West by the Mandara Mountains and the Southeast by the Kaele dome. The study area in Cameroon, covers an area of about 11628 km$^2$ and stretches from latitude 9°45 'N to 10°47'N to longitude 14°20' E to 15°30'E.

### Geological context

The Yagoua region is located in the southern part of the Logone Birni Basin (LBB) characterised by Quaternary sediments and belonging to the West and Central African Rift System. The geology of the region (Figure 1) is underlain by a large sedimentary formation and a Precambrian basement. The basement consists of acid and metamorphic formations. gneisses, migmatites, diorites, anatexites, syenites, syn-tectonic to post-tectonic granites, basalts and shales. Rare basalts are observed in the Kaélé region (Maurin, 2002). Among the bedrock outcrops, the Precambrian is dominant. It is characterized by migmatites and anatexites located southwest of the region in Maroua and Kaélé. Some remarkable features include the Mindif intrusion composed of syenites (Eno Belinga, 1984), the North Maroua gabbro hills and the Kaélé hills. The sedimentation in this
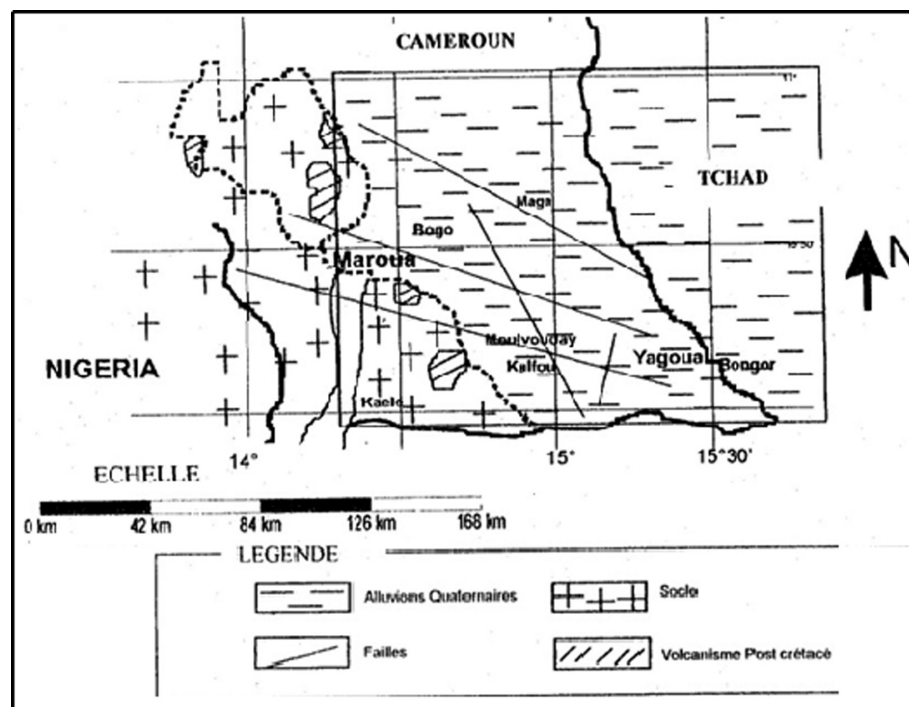


**Figure 1.** Simplied geology map of the study area.

area commenced during the Neocomian-Albian rifting period and consists of sandstones, clays and shales. The sedimentary formation is everywhere overlain by sandy alluvial formations and dunes attributable to the Pre-Bima formation (Louis, 1970; Genik, 1992).

*Gravity data*

Gravity data used in this study were acquired during surveys conducted by various organizations and researchers: Collignon (1968); Louis (1970); Elf-Serepca, 1980; Poudjoum *et al*., 1995-1996; Njandjock, 2002 to 2004 and Njandjock *et al*., 2006. Measurements were carried out along profiles to detect significant variations of geological facies. The station locations were obtained from topographic maps and compass traverses. The elevation of the stations was obtained from barometric readings, using Wallace and Tierman or Thomnen altimeters. Variations in the gravity field were measured using Worden, Lacoste & Romberg and North American gravimeters. The gravity data were converted to Cartesian coordinates and need to be interpolated. The conversion to kilometric distances was by UTM (Universal Transverse Mercator) on the Clarke's ellipsoid (1880) with the Prime Meridian. Bouguer anomaly maps by Collignon(1968), Louis (1970) and Poudjom (1996) are shwon on figures 2, 3, 4 and 5.

**Method**

The main purpose of a geostatistical study is to construct a mathematical model of the random function $Z(X)$, based on an experimental data set $Z_{exp}(X_i)$, a single realization of $Z(X)$, where $x$ and $x + h$ are two points separated by a distance $h$, and $z(x)$ and $z(x + h)$ are associated random variables. The variogram is known and the semi-variance of the difference $[z(x)-z(x + h)]$ is (Chiles and Delfiner, 1999; Kumar and Remadevi 2006):

$$\gamma(X+h) = 0,5 * Var\left[Z(X) - Z(X+h)\right] \quad (1)$$

Experimentally, it is calculated by the equation

$$\gamma(h) = \frac{1}{2N(h)}\sum_{i=1}^{n}(Z(i) - Z(i+h))^2 \quad (2)$$

Supposing that we want to estimate a block $V$ centered at $X_0$. $Z_V$ denote the true value (unknown) of this block and $Z_V^*$ the estimate that is obtained:

$$Z_V^* = \sum_{i=1}^{n}\lambda_i Z_i \quad (3)$$

$Z_i$ being the random variables corresponding to sample points. We want to minimize

$$\sigma_e^2 = Var\left[Z_V - Z_V^*\right] = Var\left[Z_V\right] + Var\left[Z_V^*\right] - 2CoV\left[Z_V, Z_V^*\right] \quad (4)$$

Substituting the expression of the estimated in this equation, we obtained

$$\sigma_e^2 = Var\left[Z_v\right] + \sum_{i=1}^{n}\sum_{j=1}^{n}\lambda_i\lambda_j CoV\left[Z_i, Z_j^*\right] - 2\sum_{i=1}^{n}\lambda_i CoV\left[Z_V, Z_i^*\right] \quad (5)$$
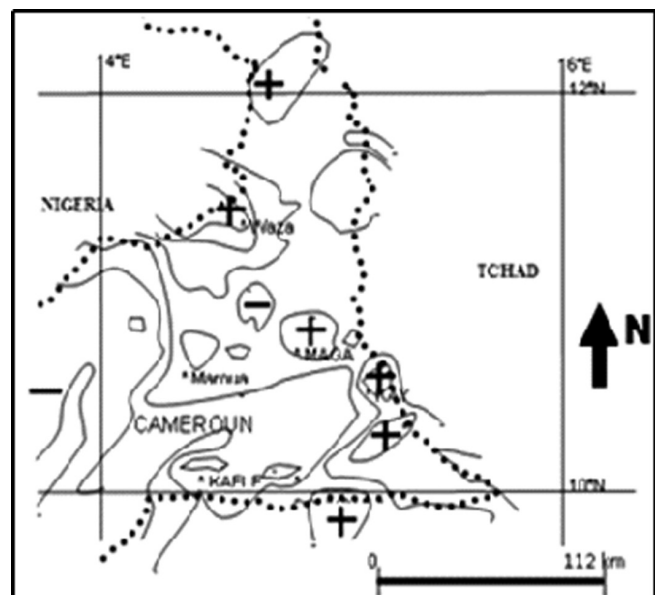


**Figure 2.** Bouguer anomaly map of Yagoua region (Collignon, 1968).
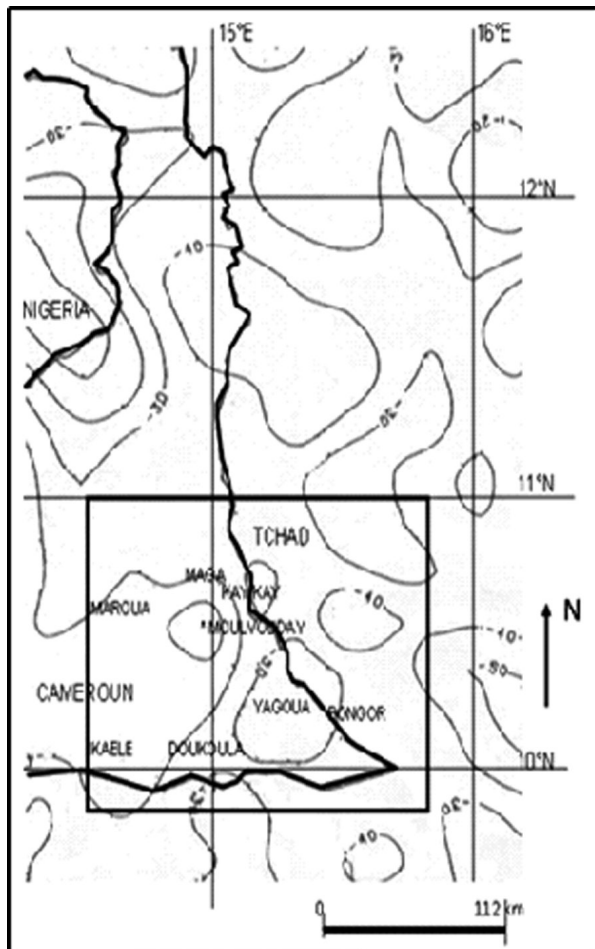
**Figure 3.** Bouguer anomaly map of Yagoua region. (Louis, 1970).
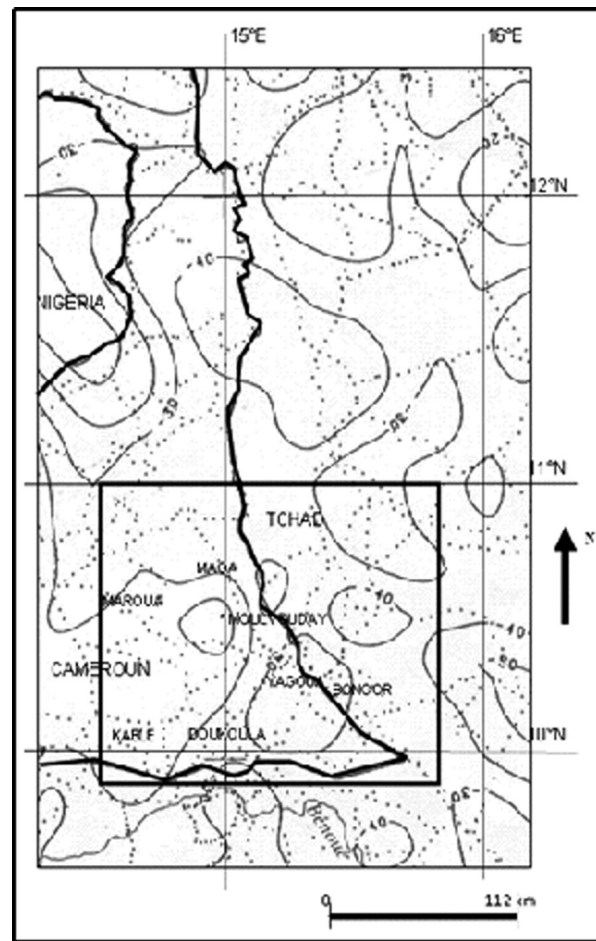


**Figure 4.** Bouguer anomaly map of Yagoua region. (Poudjom, 1996).
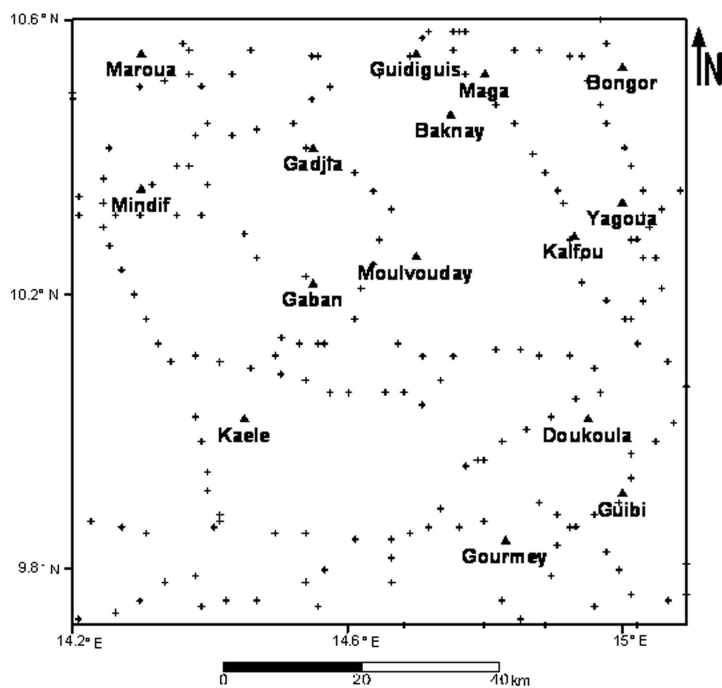


**Figure 5.** Distribution of gravity data in the study area.

Since the estimate is unbiased, we set

$$Z_V^* = \sum_{i=1}^{n} \lambda_i Z_i = 1 \qquad (6)$$

To minimize $\sigma_e^2$, we use Lagrange's method and we form the Lagrangian

$$L(\lambda,\mu) = \sigma_e^2 + 2\mu\left(\sum_{i=1}^{n} \lambda_i - 1\right) \qquad (7)$$

$$= Var[Z_V] + \sum_{i=1}^{n}\sum_{j=1}^{n} \lambda_i \lambda_j CoV[Z_i, Z_j]$$

$$- 2\sum_{i=1}^{n} \lambda_i CoV[Z_V, Z_i] + 2\mu\left(\sum_{i=1}^{n} \lambda_i - 1\right)$$

$$(8)$$

Where μ is the Lagrange multiplier. The minimum is reached when all the $\lambda_i$ and μ partial derivatives are canceled out. This leads to the following ordinary kriging system:

$$\begin{cases} \sum_{i=1}^{n} \lambda_j CoV[Z_i, Z_i] + \mu = CoV[Z_V, Z_j] \forall i = 1..n \\ \\ \sum_{j=1}^{n} \lambda_j = 1 \end{cases}$$

$$(9)$$

Minimum variance estimation called kriging variance is obtained by substituting the kriging equations in the general expression of the variance estimation.

$$\sigma_{KO}^2 = Var[Z_V] - \sum_{i=1}^{n} \lambda_i CoV[Z_V, Z_i] - \mu \qquad (10)$$

In the matrix form, these equations are written as

$$K_O \lambda_O = k_o \qquad \lambda_o = K_o^{-1} k_o \qquad (11)$$

$$\sigma_{KO}^2 = \sigma_V^2 - \lambda_o k_o \qquad (12)$$

$$\underbrace{\begin{bmatrix} \sigma^2 & CoV[Z_1,Z_2] & . & CoV[Z_1,Z_n] & 1 \\ CoV[Z_2,Z_1] & \sigma^2 & . & CoV[Z_2,Z_n] & 1 \\ . & . & . & . & . \\ CoV[Z_n,Z_1] & CoV[Z_n,Z_2] & . & \sigma^2 & 1 \\ 1 & 1 & . & 1 & 0 \end{bmatrix}}_{K_o} \underbrace{\begin{bmatrix} \lambda_1 \\ \lambda_2 \\ . \\ \lambda_n \\ \mu \end{bmatrix}}_{\lambda_o} = \underbrace{\begin{bmatrix} CoV[Z_1,Z_V] \\ CoV[Z_2,Z_V] \\ . \\ CoV[Z_n,Z_V] \\ 1 \end{bmatrix}}_{k_o}$$

$$(13)$$

## Results and Discussion

*Experimental variogram of the Yagoua region*

The experimental variogram is now calculated from equation (2). Results are ranked by increasing distance, and then grouped in intervals centered on increasing multiples of h= 5. The results shown in Table 1, are used to plot the variogram (Figure 6).

**Table1.** Experimental variogram values of Bouguer anomalies corresponding to the pitch h.

| h | Experimental variogram |
|---|---|
| 5 | 20.9 |
| 10 | 43.8 |
| 15 | 61.9 |
| 20 | 72.0 |
| 25 | 81.0 |
| 30 | 81.3 |
| 35 | 81.3 |
| 40 | 81.3 |

The variogram characteristics are: range a = 25; level $C + C_0 = 81$; nugget; $C_0 = 1$.

The known mathematical variogram models in the literature were used to calculate different models of variograms and compare them to the experimental one (Figures 6 and 7). The results are summarized in table 2. In these calculations, several models (for example the Gaussian model) not shown here have been eliminated. The superposition of curves giving the variogram as a function of h is given in Figure 7. The dark blue curve represents the experimental variogram of the Yagoua region. Our aim is to find among the other curves of this graph the one that best approximates the dark blue curve. The outer gray curve represents the gravity model whose elimination is visible; it is difficult to comment on the other curves. Indeed within this paragraph, it is difficult to say exactly which curve (red, green, purple, blue or orange) is closest to the dark blue curve. Qualitatively all these models are eligible. For this reason we will make a quantitative analysis using the equation

$$RMS = \sqrt{\sum_{i=1}^{n} (\gamma_{i\exp} - \gamma_{itheo})^2} \qquad (14)$$
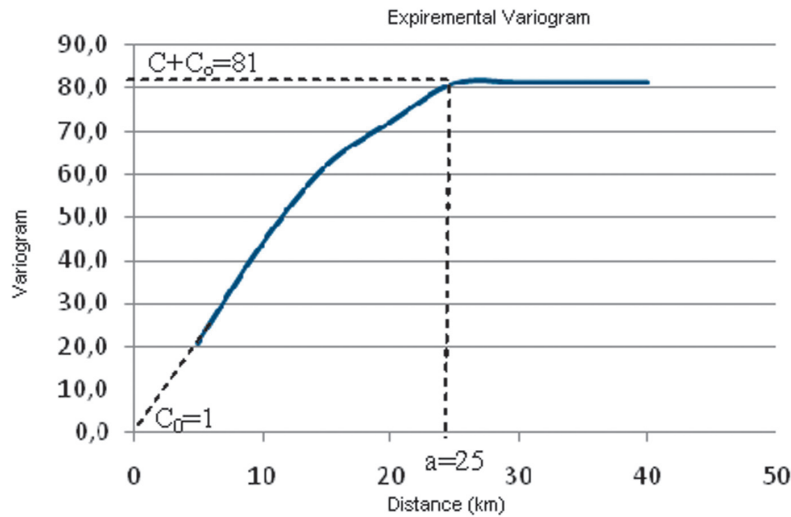
**Figure 6.** Experimental variogram of gravity data from the Yagoua region.
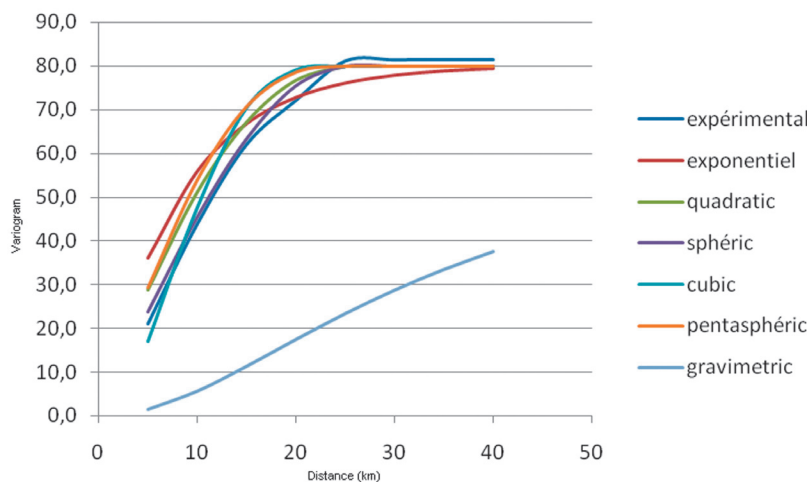


**Figure 7.** Superposition of the curves giving the variogram according to the pitch h.

**Table 2.** Variograms of different models and compare the experimental variogram.

| h | experimental | exponential | quadratic | spheric | cubic | pentaspheric | gravimetric | gaussian |
|---|---|---|---|---|---|---|---|---|
| 5 | 20.9 | 36.1 | 28.8 | 23.7 | 16.9 | 29.2 | 1.6 | 80 |
| 10 | 43.8 | 55.9 | 51.2 | 45.4 | 47.6 | 53.9 | 5.7 | 80 |
| 15 | 61.9 | 66.8 | 67.2 | 63.4 | 70.5 | 70.7 | 11.4 | 80 |
| 20 | 72.0 | 72.7 | 76.8 | 75.5 | 79.2 | 78.6 | 17.5 | 80 |
| 25 | 81.0 | 76.0 | 80.0 | 80.0 | 80.0 | 80.0 | 23.4 | 80 |
| 30 | 81.3 | 77.8 | | 80.0 | 80.0 | 80.0 | 28.8 | 80 |
| 35 | 81.3 | 78.8 | | 80.0 | 80.0 | 80.0 | 33.5 | 80 |
| 40 | 81.3 | 79.3 | | 80.0 | 80.0 | 80.0 | 37.6 | 80 |

to calculate the relative changes, and standard deviation of these relative changes between each variogram model and the experimental variogram.

Changes between experimental variogram values and those of different models are reported in table 3. The standard deviation values between the experimental variogram and the different model is 2.0 for spherical, 3.3 for quadratic, 5.2 for pentaspherical, 7.5 for exponential and 13.2 for Gaussian (table 3). It is clear that the model giving the best variogram model are the spherical, tracking quadratic and pentaspherical models. In order to confirm or invalidate this result, we made

**Table 3.** First standard derivation of different models.

| | Δexponential | Δquadratic | Δspheric | Δcubic | Δpentaspheric | Δgravimetric | Δgaussian |
|---|---|---|---|---|---|---|---|
| | 15.3 | 8.3 | 2.8 | -1.3 | 8.4 | -19.4 | 79.4 |
| | 12.4 | 8.3 | 1.8 | 11.5 | 10.3 | -38.0 | 75.3 |
| | 5.1 | 6.4 | 1.7 | 31.1 | 9.1 | -50.5 | 69.6 |
| | 1.0 | 6.0 | 3.8 | 21.0 | 6.9 | -54.4 | 63.4 |
| | -4.7 | 0.3 | -0.7 | 12.0 | -0.7 | -57.5 | 57.5 |
| | -3.2 | -81.3 | -1.0 | 11.7 | -1.0 | -52.4 | 52.1 |
| | -2.2 | -81.3 | -1.0 | 11.7 | -1.0 | -47.7 | 47.4 |
| | -1.7 | -81.3 | -1.0 | 11.7 | -1.0 | -43.6 | 43.3 |
| Standard deviation | 7.5 | 3.3 | 2.0 | 9.3 | 5.2 | 12.2 | 13.2 |

kriged maps using several models. The goal is to determine which variogram model reproduces the experimental values. For this purpose, we have omitted 15 of the 188 baseline. Then we realized the kriged map of spherical, square, pentaspherical, exponential, cubic, Gaussian, rational quadratic and power models with the 173 remaining data. On these kriged maps, we reported values of anomalies the hidden points. Abnormal values obtained by kriging with different variogram models are shown in table 4. The relative differences between the anomalies from various models and the current anomalies are contained in table 5.

The lowest standard deviation 2.69 is obtained with the spherical model, followed by 2.86 for the exponential model and 2.87 for the pentaspherical model. The spherical model is the one that is best reproduced by kriged data or field values. In both approaches, the first four eligible models are the same (spherical, pentaspherical, quadratic and exponential) but in a different ranking than the second, the first being the spherical model. The differences between the values of standard deviation from one model to another are not great. This was predictable because curves in Figure 7 are all very close to the experimental variogram curve.

**Table 4.** Variograms of different models and the experimental values.

| x | y | Experimental values | spherical | quadratic | pentaspherical | exponential | cubic | gaussian | power | Rational quadratic |
|---|---|---|---|---|---|---|---|---|---|---|
| 0 | 116 | -32 | -38.11 | -38.32 | -38.35 | -38.22 | -38.25 | -21.67 | -37.71 | -38.19 |
| 7 | 32 | -32 | -37.14 | -38.43 | -38.31 | -38.49 | -37.73 | -27.96 | -39.25 | -32.38 |
| 11 | 97 | -30 | -32.05 | -32.23 | -32.08 | -31.86 | -30.7 | -30.83 | -32.91 | -30.65 |
| 13 | 102 | -31 | -31.09 | -31.55 | -31.35 | -30.65 | -31.8 | -31.79 | -31.78 | -33.56 |
| 19 | 105 | -33 | -32.91 | -32.54 | -32.54 | -32.73 | -32.35 | -28.68 | -32.88 | -30.94 |
| 21 | 118 | -35 | -35.22 | -34.66 | -34.67 | -35.28 | -35.5 | -37.45 | -35.02 | -36.52 |
| 28 | 94 | -40 | -40.54 | -41.61 | -41.81 | -40.96 | -42.76 | -48.61 | -40.84 | -47.32 |
| 38 | 70 | -49 | -48.41 | -48.18 | -48.33 | -48.64 | -48.54 | -46.1 | -48.28 | -48.3 |
| 52 | 41 | -41 | -41.75 | -41.74 | -41.75 | -41.67 | -42.11 | -60.09 | -41.55 | -42.28 |
| 67 | 47 | -38 | -39.36 | -39.29 | -39.37 | -39.34 | -40.22 | -32.33 | -39.3 | -39.36 |
| 78 | 64 | -45 | -40.88 | -41.89 | -41.99 | -41.26 | -42.1 | -29.82 | -40.93 | 39.39 |
| 87 | 83 | -37 | -36.42 | -34.06 | -34.21 | -35.62 | -26.02 | -11.62 | -35.75 | -16.23 |
| 91 | 93 | -13 | -15.57 | -15.24 | -15.1 | -16.07 | -13.97 | -14.12 | -17.49 | -15.64 |
| 100 | 35 | -30 | -32.19 | -31.84 | -31.81 | -30.96 | -30.93 | -27.75 | -30.25 | -30.45 |
| 45 | 68 | -52 | -48.58 | -48.69 | -48.8 | -48.69 | -50.57 | -53.93 | -48.6 | -49.75 |

**Table 5.** Second standard derivation of different models.

| Δspherical | Δquadratical | Δpentaspherical | Δexponential | Δcubic | Δgaussian | Δpower | Δrational quadratic |
|---|---|---|---|---|---|---|---|
| 6.11 | 6.32 | 6.35 | 6.22 | 6.25 | -10.33 | 5.71 | 6.19 |
| 5.14 | 6.43 | 6.31 | 6.49 | 5.73 | -4.04 | 7.25 | 0.38 |
| 2.05 | 2.23 | 2.08 | 1.86 | 0.7 | 0.83 | 2.91 | 0.65 |
| 0.09 | 0.55 | 0.35 | -0.35 | 0.8 | 0.79 | 0.78 | 2.56 |
| -0.09 | -0.46 | -0.46 | -0.27 | -0.65 | -4.32 | -0.12 | -2.06 |
| 0.22 | -0.34 | -0.33 | 0.28 | 0.5 | 2.45 | 0.02 | 1.52 |
| 0.54 | 1.61 | 1.81 | 0.96 | 2.76 | 8.61 | 0.84 | 7.32 |
| -0.59 | -0.82 | -0.67 | -0.36 | -0.46 | -2.9 | -0.72 | -0.7 |
| 0.75 | 0.74 | 0.75 | 0.67 | 1.11 | 19.09 | 0.55 | 1.28 |
| 1.36 | 1.29 | 1.37 | 1.34 | 2.22 | -5.67 | 1.3 | 1.36 |
| -4.12 | -3.11 | -3.01 | -3.74 | -2.9 | -15.18 | -4.07 | -84.39 |
| -0.58 | -2.94 | -2.79 | -1.38 | -10.98 | -25.38 | -1.25 | -20.77 |
| 2.57 | 2.24 | 2.1 | 3.07 | 0.97 | 1.12 | 4.49 | 2.64 |
| 2.19 | 1.84 | 1.81 | 0.96 | 0.93 | -2.25 | 0.25 | 0.45 |
| -3.42 | -3.31 | -3.2 | -3.31 | -1.43 | 1.93 | -3.4 | -2.25 |
| **Standard deviation** 2.693 | 2.9278 | 2.872 | 2.863 | 3.9502 | 10.106 | 3.0856 | 22.652 |

## A new Bouguer map of Yagoua region

The new Bouguer anomaly map (Figure 8) obtained by the kriging method reveals several anomalies which can be grouped into two major families: a family of negative anomalies and a family of positive anomalies. The positive anomalies are located south of Kaele, at Guibi-Doukoula, Yagoua, Guidiguis and at Maroua-Mindif. The positive anomalies of Guibi-Doukoula and Yagoua, observed on the new map, also appear in other documents. They appeared separated on
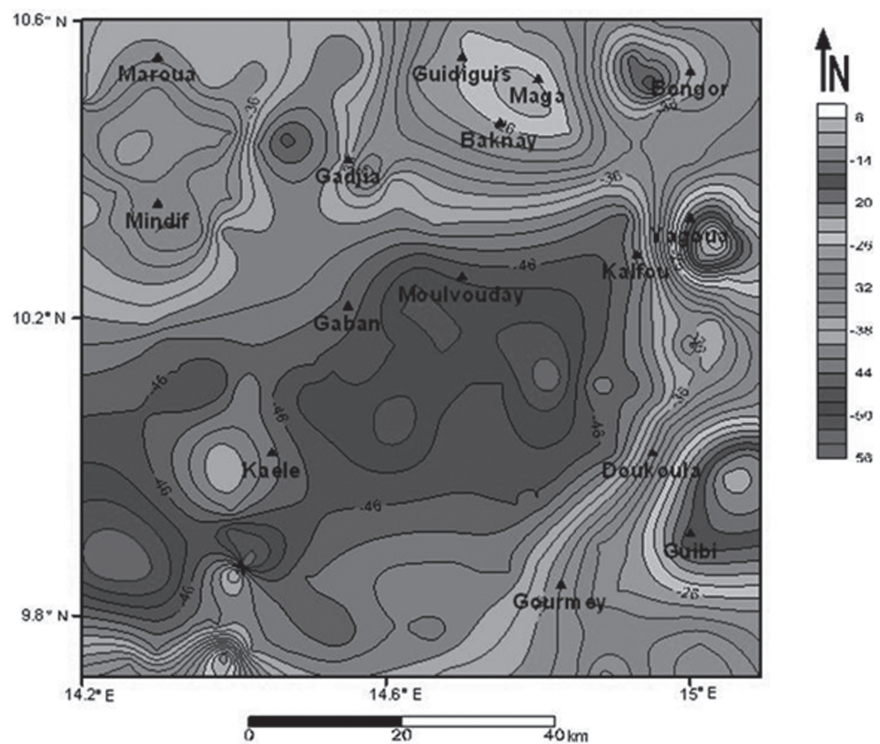


**Figure 8.** New anomaly Bouguer map of Yagoua region, 2012.

Collignon (1968) but are absent on Louis (1970) and Poudjom *et al*. (1996) maps. The reappear clearly separated on the new map proposed by the current study. In addition, this map brings out the positive anomalies of Maga and Maroua-Mindif formerly reported by Collignon (1968) and absent on Louis (1970) and Poudjom *et al*. (1996) maps. By comparing these results (Figure 9) with the geological map (Figure 1) and, according to Manga *et al*. (2001), Njandjock (2004) and Njandjock *et al*. (2006), the positive anomalies of Guibi-Doukoula, Yagoua and Guididuis correlate with an uplift of gneissic-granite type dense materials. The positive anomaly of Maroua-Mindif correlates with Mindif's "tooth" syenite block. The negative anomaly directed NE-SW extends from west Kaele to north Moulvouday and occupies the center of the study area. This negative anomaly is surrounded by positive anomalies and may coincide with a Quaternary sedimentary cover at Moulvouday. Compared to Manga *et al*. (2001) and Njandjock *et al*. (2006), this large anomaly may be the gravity signature of the Moulvouday-Yagoua sedimentary basin.

## Conclusion

In this study, the experimental variogram was calculated from the existing gravity data. The RMS and the hindered points technique showed that the best theoretical variogram for these data were spherical. This variogram was therefore used to produce a new regular gravity data base and a new gravity map of the Yagoua region which can be used in further researches. This study includes mapping of the Moulvouday negative anomaly which may correlate with sedimentary thickening, while positive anomalies of Guibi-Doukoula and Yagoua may correspond to granite-gneiss dense basement material uplift. In addition, we confirm the positive anomalies of Maga and Maroua-Mindif which no longer appeared on Louis (1970) and Poudjom *et al*. (1996) but were reported by Collignon (1968). In addition, positive anomalies of Guibi-Doukoula and Yagoua that appeared separated on the Collignon map (1968), and which were present on the Louis (1970) and Poudjom *et al*. (1996) maps, reappear clearly separated.

## Acknowledgements

## Bibliography

Bessoles B., Trompette R., 1980, The Pan-African chain, mobile zone of Central Africa mobile zone and sudden, BRGM. Memory 92.

Chiles and Delfiner, 1999, Geostatistics, Modeling spatial uncertainty. Wiley series on probability and statistics.

Collignon F., 1968, Gravimétrie de reconnaissance du Cameroun. *Orstom*, 37p.

Elf-Serepca, 1981, Geological Map of Garoua basin's, Operating service.

Eno Belinga S.M, 1984, *Geology of Cameroon*. University Bookstore in Yaoundé, p.307.

Genik G.J, 1992, Regional structural gravimetry and petroleum aspects of basins in Niger, Chad and Central African Republic (CAR), *Tectonophysic*, 313, 169-185.

Kumar V., Remadevi, 2006, Kriging of Groundwater Levels – A case Study. J*ournal of Spatial Hydrology*, 6, 1, 81-94.

Louis P., 1970, Contribution géophysique à la connaissance géologique du bassin du lac Tchad. *Orstom*, 42, Paris 311p.

Manga S.C., Loule J.P., Koum J.J., 2001, Tectonostratigraphic evolution and prospectivity of Logone Birni Basin, North-Cameroon-Central Africa. *AAPG Extended Abstracts*, 124.

Matheron G., 1973, The intrinsic random functions and their applications. *Advances in applied probability*, 5, 439-468p.

Maurin S., 2002, Geomorphology, atlas of the province of the far North Cameroon. Plate 04, MINRESI-INC-Cameroon.

Njandjock Nouck P., 2004, Gravimetric investigation and mapping of geological structures in the superficial and deep-Cameroon region Yagoua Ph.D Thesis in Physics. University of Yaounde I.

Njandjock Nouck P., 2007, Note on geostatistical courses, University of Yaounde I.

Poudjom-Djomani Y.H., Legeley-Padovani A., Boukele D.B., Nnange J.M., Ateba-Bekoa, Alboul Y., Fairhead J.D., 1996, Levés gravimétriques de reconnaissance-Cameroun. *Orstom*, France, 30p.

Vicat J.P., Bilong P., 1998, Geology and environment in Cameroon. University Press of Yaounde.

# Relationship between age of waste and natural electric potential generation in Sanitary Landfill

César Augusto Moreira*, Antonio Celso de Oliveira Braga, Letícia Hirata Godoy and Diego de Sousa Sardinha

## Resumen

Los métodos geofísicos constituyen una herramienta efectiva para determinar alteraciones en las propiedades físicas de los ambientes geológicos, como son los suelos y aguas subterraneas influenciados por contaminantes. Este trabajo consistió en el análisis del potencial eléctrico natural obtenido en zanjas que contienedesechos sólidos con tiempo de confinamiento controlado. La interpretación de los resultados indica una correlación entre el tiempo de confinamiento de los residuos y el aumento de las variaciones de voltaje. Los datos sugieren que el potencial eléctrico resulta predominantemente de el fenómeno de potencial de oxidación/reducción, siendo el potencial del flujo insignificante. A través del análisis estadístico de los datos se estimó ocho años para volver a las características de una zona ausente de residuo, tiempo estimado para la descomposición de la mayor parte de la materia orgánica contenida en los residuos enterrados.

Palabras clave: zanja, potencial espontáneo, materia orgánica, descomposición, oxidación.

## Abstract

The geophysical methods are effective tools for determining changes in physical parameters of the geological environment, as soil or groundwater in the presence of contamination. This work consisted on analyzing the natural electric potential obtained over domestic solid waste ditches with controlled closure dates. The interpretation data suggest the generation of electric potential predominantly through the redox phenomenon, as opposed to the flow potential phenomenon. The statistical data analysis indicates a correlation between residence time of the waste and growing variations of voltage. In addition highlights that eight years are required to achieve the reported values for the area with absence of waste, time estimated for decomposition of most organic matter contained in the buried waste.

Key words: ditch, self-potential, organic matter, decomposition, oxidation.

C. Augusto Moreira*
A. Celso de Oliveira Braga
Departamento de Geologia Aplicada (DGA)
Instituto de Geociências e Ciências Exatas (IGCE)
Universidade Estadual Paulista (UNESP)
Rio Claro, São Paulo State, Brazil
Av. 24-A, 1515, Bela Vista
CEP 13506-900, Rio Claro
São Paulo, State, Brazil
*Corresponding author: moreirac@rc.unesp.br

Letícia Hirata Godoy
Instituto de Geociências e Ciências Exatas (IGCE)
Universidade Estadual Paulista (UNESP)
Av. 24-A, 1515, Bela Vista. CEP 13506-900, Rio Claro,
São Paulo State, Brazil

Diego de Sousa Sardinha
Instituto de Ciência e Tecnologia (ICT)
Universidade Federal de Alfenas (UNIFAL)
Poços de Caldas, Minas Gerais State, Brazil
Rodovia  BR 267, Km 533  - CEP 37701-970
Poços de Caldas, Minas Gerais State, Brazil

## Introduction

There is a growing need to adapt the application of direct and indirect investigative techniques for use in environmental studies, due to the large amount of synthetic compounds or petroleum products for final use or as raw materials for other industries, spillage or leakage risk during transport and manipulation of these compounds, in addition to undue leaks or discharges of effluents and solid or liquid waste generated during industrial processes, domestic and urban activities.

Detection of changes in physical properties caused by the percolation and residence of contaminants in soils and rocks is the object of study of geophysics applied to environmental studies. The contrast between assessed areas and surrounding areas with natural characteristics to the physical parameter measured, allows 2D and 3D delimitation of potentially contaminated areas.

Studies aimed at analyzing and understanding the behavior of these compounds in the geological environment are necessary and essential, from the perspective of physical and chemical changes due to the presence and interaction with the environment, climatic seasonality, oxygen availability, physical-chemical conditions and others. These changes result in the reduction of compounds toxicity in many cases.

However, in some cases, the release of metals possibly contained in mineral constituents or compounds may occur, as well as a possible increase of toxicity by compounds generated from the degradation of initial contaminants.

Understanding the modifications of physical properties as for the presence of contaminants in geological environment is essential to geophysics application and interpretation in environmental studies.

Measures of self-potential (SP) can promote means of detection and relative quantification of contaminants in groundwater. Baker and Cull (2004) applied the method in the valley of King river – Tasmania, to evaluate the presence of metals from tailings of the Mt. Lyell sulphide mine located nearby. The contours of electric potential were consistent with hydraulic potential estimated by piezometers, factor that assisted on the refinement of groundwater flow model and understanding the pressure gradients observed in drillings.

In Mota *et al*. (2004) study, self-potential and electro resistivity methods were applied to evaluate the granitic massif structure underlying Póvoa de Lanhoso – Portugal landfill. The results allowed the definition of low resistivity zones correlated with negative values of self-potential, which indicates impacted areas by contaminants from the landfill.

In this research line, Nimmer and Osiensky (2002) made self-potential and resistivity measurements in surface and in drilling holes to assess the flow of a salt plume in a partially fractured basalt in Idaho – United States. The results indicate that self-potential allows additional details about the plume dynamics in a complex environment, in relation to artificial electric field techniques, which in some surveys were insensitive to contaminants presence.

These cases quoted above corroborate the hypothesis of self-potential generation by the flow of electrolyte solutions in porous and fractured aquifers, represented in these cases by contaminants from the landfill and saline solution.

Measures of self potential and redox potential (Eh) were used in the works of Naudet *et al*. (2003) and Naudet *et al*. (2004) to study the evolution of a contaminant plume from a landfill. The results show that the electric potential progressively decreases in the aerobic zone, increases dramatically in the redox front and finally reaches the standard of the study area when achieve the oxidation zone. There is a high correlation between measurements of self-potential and redox potential in the profile.

The previously mentioned works, in contrast, indicate the possible generation of natural electric potential by degradation processes of the organic compounds accumulated in solid waste landfills.

This study evaluates the results of applying self-potential method at a domestic organic waste landfill, arranged in trenches with different closing dates. The relationship between time of closing trenches, decomposition of organic waste and variations of voltage measured by geophysical method, allow estimating the time necessary to geochemical stabilization of the area.

## Methodology

The self-potential method is characterized by natural electric field accuracy readings, without any electric current injection circuit or generation of electromagnetic field (Orellana 1972). The advantage lies in the simplicity of involved instrument and versatility of data acquisition into small areas, in addition to the variability of the physical parameter as measured in the geological environment. The main disadvantages associated with the method are the need of connecting cables between reading sensors and the equipment, use of non-polarizable electrodes, besides the high susceptibility to noises produced by electrical systems such as transformers, grounding and

engines, elements that may hinder tests in large or urban areas.

Contrasts of self-potential results in variations of temperature, pressure gradient, porosity, fluid migration, variation of resistivity and soil humidity (Corwin 1990). As for the generation process, self-potential can be classified as electrochemical potential, electrolytic and mineral. The mineral potential arises due to geochemical redox reactions in an ore body, corresponding to the galvanic cell defined by Electrochemistry.

From the analysis of the main current theories, Sato and Mooney (1960) proposed a mechanism for the origin of self-potential, within the phenomenon of mineral potential. This mechanism involves a reaction between two electrochemical cells, present simultaneously in two different locations in an ore body. Normally, one cell is above and another below the phreatic level and are interconnected by ore body. These two cells are opposite in nature, an anode and a cathode, with reactions involving gain and loss of electrons. Above the phreatic level oxidation reactions occur, while below reduction takes place.

The potential differences generate natural currents that arise due to redox potential differences of the surrounding solution through contact between the edges of the ore body. The dissolved substances around the upper body are in relative state of oxidation and reduction below the phreatic level, these relative differences in the degree of oxidation are revealed in different Eh values and result in electric current flow in the presence of an electronic conductor, in this case represented by the ore body.

The reduced electrons from the lower portion are conducted to the oxidized upper portion through the ore body, in this way the lower portion is relatively oxidized opposite to the upper, relatively reduced. In this mechanism, the ore body does not participate directly in the electrochemical reactions, otherwise, would be consumed during the process. This acts only as a mean of transporting electrons chemically inert.

Corry (1985) and Nyquist and Corry (2002) works analyzed Sato and Mooney (1960) proposal and raised some incongruent questions in the proposed model:

*Width:* according to this model, values greater than 800mV are not possible based on the Eh potential of sulfides, whose maximum amplitude of the anomaly generated between the poles of geobattery in relation to the reference electrode is only 400mV. However, several studies of sulfide bodies have reported values of 1000mV or more (Gay 1967).

*Loss of the positive pole:* This model requires positive and negative poles. Measures of self-potential in surface, subsurface and drill hole in ore bodies show negative anomalies relative to the reference electrode located near the body.

*Groundwater level:* There are no references in this model regarding anomalies of self-potential in ore bodies completed dry or wet or over sulfides, characterized by central conductor not inert.

*Stability:* direct measures of self-potential anomalies associated with sulfide bodies are stable for decades and, presumably, during geologic time. However, the model does not explain how the geobattery does not discharge or values do not fluctuate in the face of seasonal fluctuations of the phreatic level and the consequent seasonal variations in chemical composition of groundwater.

Such authors suggest that the arrangement of pairs of electrodes only measure the difference of potential between the electrode on the anomaly and the reference electrode.

In a galvanic cell electric current flow doesn't occur unless the electrodes are set in environments with potential differences. This way self-potential would be generated between electrodes connected by a cable and not by an ore body, from the closed circuit between a relatively more oxidized zone and another more reduced.

The electrochemical potential can be originated by biodegradation processes in soil or rock context with organic matter, present in landfill. These materials are frequently recovery by successive layers of soils after filling dispositions cells. Such context allows the predominance of physical and chemical reduction conditions in waste, responsible for stimulating a proliferation of anaerobic microorganism colonies.

The action of microorganism in organic matter occurs by three successive stages (Themelis & Ulloa, 2007; Barlaz *et al*., 2002). In principle, fermentative bacteria hydrolyze the complex organic matter into soluble molecules, which in turn are converted by acid forming bacteria to simple organic acids, carbon dioxide and hydrogen; the principal acids produced are acetic acid, propionic acid, butyric acid and ethanol. In the third stage, methane is formed by methanogenic bacteria, either by breaking down the acids to methane and carbon dioxide, or by reducing carbon dioxide with hydrogen.

The contrast between reduction in waste and oxidation in geologic substratum results in similar conditions to electrochemical cell, in intensity measurable by geophysical instruments.

## Study area

The Cordeirópolis landfill is located at km 4.5 of Cássio Freitas Levy highway (Cordeirópolis-Limeira highway), Cordeirópolis city, São Paulo State, Brazil (Figure 1). The city has about 17,000 inhabitants, with an economy based on the production of ceramic tiles and the cultivation of sugar cane. The daily production of domestic solid waste is approximately 6m$^3$.

The study area is a trench-type controlled landfill, for disposal of domestic solid waste only. The operating system consists in 5 m deep trenches, 4m wide and 80m long, for directly disposal of waste on the soil and subsequent coating with a soil layer of 1m.

This area has 48.400 m$^2$ available for waste disposal, starting with activities in 11/2001 and life expectancy to 20 years. The physical structure of the landfill is devoid of electric power distribution systems.

The topography of the area is fairly flat, with average slope of 0.5 % in southeast direction and altitude between 660m and 659m. The landfill is surrounded by sugar cane cultivation.

The substrate is constituted by clay soil with 10m thick, and above by a body of diabase with 15m thick. Below there are fine sandstones and siltstones belonging to Tatuí Formation. Groundwater level is located at an average depth of 50m, with flow direction to the southeast, both determined using vertical electrical sounding (Moreira *et al*, 2009). Field tests of saturated hydraulic conductivity revealed average values of 10$^{-4}$cm/s for the soil. There are no wells installed in the area or any other environmental monitoring systems.

In this area 241 readings of self-potential were made through the fixed base arrangement, distributed in regular mesh of the acquisition, with start of recent ditch (extreme NW) from oldest ditch (extreme SE). The base electrode was fixed upstream of groundwater flow, precisely at the landfill access gate (Figure 1).

The acquisition was performed in two steps:

- First step: voltage readings in square mesh of 20m x 20m, for a broad characterization of the area.

- Second step: readings taken just about the ditches with closing date in December, between 2001 and 2007, with 5m spacing between readings. This step objective was to determine a possible relationship between the decomposition of buried waste and voltage variations over time.
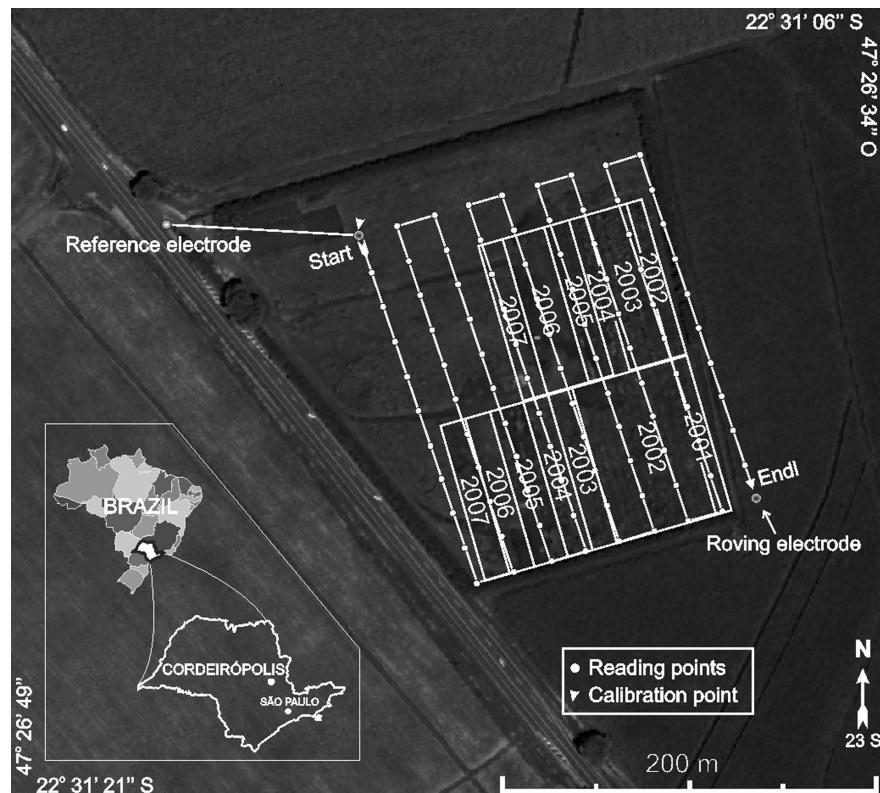


**Figure 1.** Area of study.

This study used non-polarizable Pb-PbCl$_2$ electrodes characterized by high stability over time (Petiau 2000). The data reduction involved the following proceedings: acquisition of absolute voltage, drift correction between initial and final lines and base tie-in correction, according Corry (1985) and Telford *et al*. (1990).

The obtained data after reduction are presented graphically. The measurements obtained in regular mesh were georeferenced and interpolated in the program Surfer 8.0, by the neighborhood method.

In the neighborhood method, initial groups are established by the highest coefficients of mutual association, for the admission of new members is sufficient to determine which represent the highest association with the elements of a given group (Landim 2004). Hence, the choice of the interpolation method was based in fidelity to the interpolated values and limitations of the surface to the extreme input values.

## Results

The self-potential measurements in regular mesh are presented in map, below closure ages of waste ditches (Figure 2).

The acquired data indicate more negative values in the ditches closed between 2007 and 2006 (0mV to 10mV), and widespread occurrence of values between 10mV and 30mV in ditches closed between 2005 and 2004. Measures between 30mV and 70mV occur in ditches closed between 2003 and 2001.

The position of the groundwater level around 50m deep, waste ditches dug up to 5 m deep in clay soil, suggest that the values of self-potential are produced by geochemical activity. The relationship between voltages values increasing positively with increasing time of organic waste degradation contributes to this effect.

Measures below 20mV are practically contained in the ditches limits closed between 2007 and 2006. The trend of increasing positive values in the oldest ditches may be associated with the decrease of available organic matter and consequent geochemical stability. The elevated measurements obtained in the ditches closed between 2003 and 2001 may indicate an advanced stage of degradation.

The generation of leachate and its chemical, physical and microbiological characteristics are related to the decomposition of organic matter present in the solid waste stored in landfills.

The fluids produced in landfills are often acidic, with variations associated with substrate type, climate, waste type, and seasonal variations, among others. From the production of leachate



**Figure 2.** Self-potential map with closure ages of the ditches.

several changes occur that involve aerobic stages - acetogenic, and anaerobic - methanogenic (Bagchi, 1987; Fang 1995). The pH tends to increase with time since initial acid forms tend to neutralized states, with decrease of chemical oxygen demand (COD) and biological oxygen demand (BOD) (Farquhar 1989; Moreira *et al*, 2009). The total organic carbon content, total fatty acids or ketones and total dissolved solids are high during acetonagenesis and low for methanogenesis, ie decrease with residence time of organic matter (Birks & Eyles, 1997; Meju, 2000).

The self-potential data acquired during the second stage surveys confirm the trend of increased self-potential for recent ditches to old ones (Figures 3 and 4). This increase is possibly associated with increased geochemical stability over the period of organic waste degradation.

Large amounts of water can permeate the bit compressed waste in old landfills, when compared to landfills recently compressed, resulting in a relative low concentration of chemical constituents in leachate of old landfills, with high porosity and permeability (Radnoff *et al*. 1992).

The study area is located in a context of clay soils and low hydraulic conductivity, also associated with the fact of the occurrence of a profound groundwater. In this case, it is likely that the oxygen supply in the ditches of waste occurs by percolation of rainwater in all the ditches, with an increase of atmospheric oxygen, especially in the oldest graves, where the compaction of waste results in the fracturing of the soil cover.

Even further incursions of oxygen result in little geochemical activity due to drastic reduction in the supply of organic matter consumed over the years of the waste residence.

The obtained values on the reference line are relatively less variable and higher than those acquired on the waste ditches. In contrast, the values obtained on the ditches have a tendency of increase or decrease towards the end of the line, respectively referring to the ditches in 2007 and 2003. Relatively higher values in the central portion of the lines are presented by the measurements obtained on the ditches in 2002 and 2001.

The measurements on the 2007 ditch present relative lower values, with extreme measures between -1mV to 28mV. The ditches in 2006, 2005 and 2004 present higher values, with extremes measures between 20mV and 48mV.

Statistical analysis of self-potential average values measured on the waste ditches indicates the period of 8 years to return to the natural values, from the first year of closure (Figure 5).

Due to the low permeability of the landfill soil, it is likely that the electrical potential measured reflects almost exclusively the redox potential of the organic matter contained in the buried waste, as described in papers by Naudet *et al*. (2003), Naudet *et al*. (2004) and Moreira *et al*. (2011), to the detriment of electrical potential generated by the flow of inorganic solutions in porous and fractured aquifers, such as the work of Baker and Cull (2004), Mota *et al*. (2004), Nimmer and Osiensky (2002).

In this sense, the estimated period for return to the natural values of electric potential must indicate the time required for consumption of organic material from rapid decomposition. In a context of domestic solid waste, this organic material is represented mainly by food debris, oils and vegetal and animal residues, in addition to oil derived products and greases on a smaller scale.
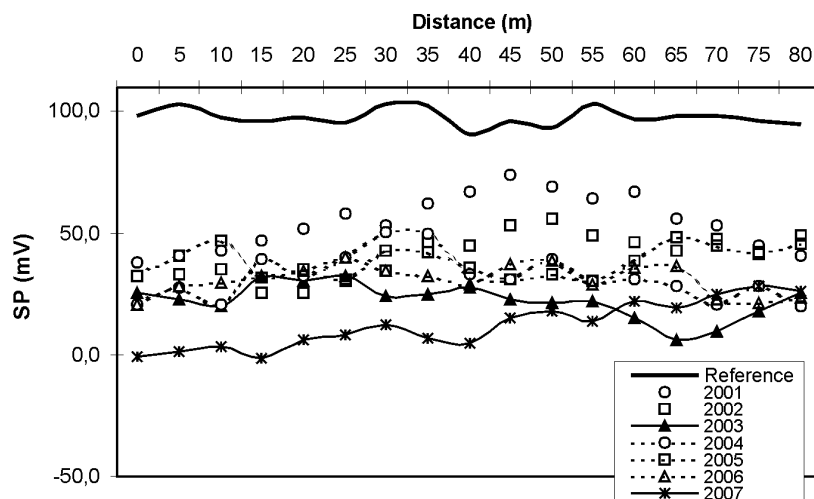


**Figure 3.** SP measures obtained over the ditches.

**Figure 4.** Mean and extreme values of SP for the second stage surveys.
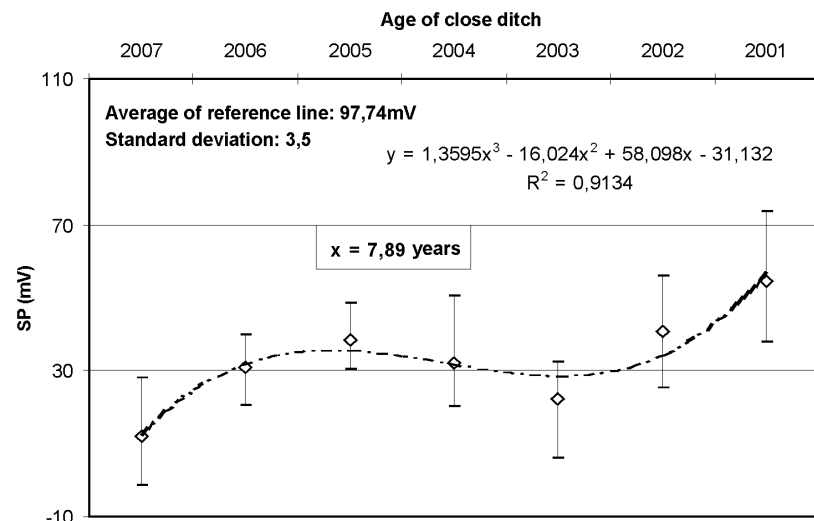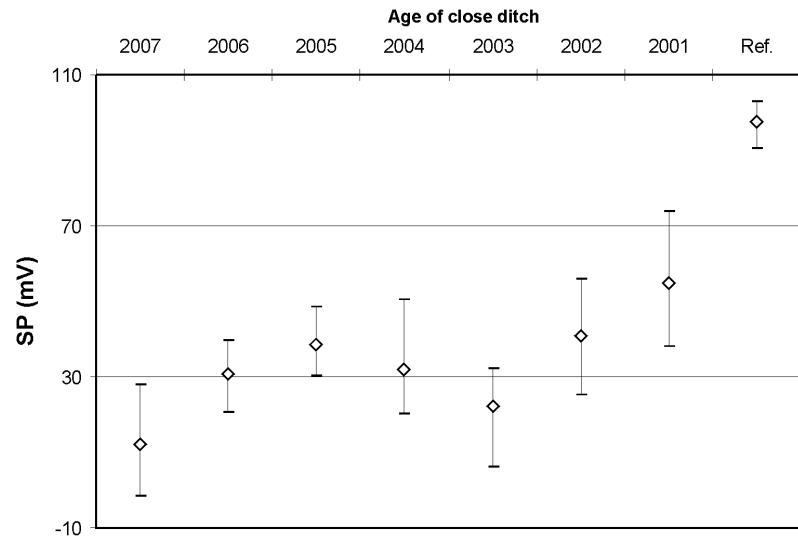


**Figure 5.** Statistical analysis of the second stage data.



## Conclusion

The results show the possibility of applying the self-potential geophysical method in studies of domestic solid waste disposal areas, whether as preliminary studies in areas under the absence of environmental monitoring devices, or as a complementary technique of investigation.

However, the applicability of the self-potential method and the results obtained in this work were made possible due to absence of electrical noise and the small area covered during the survey. The application of this method for studies in urban areas is severely impaired due to the frequent presence of electrical systems in this environment, which generate interference during measurements.

The natural electrical potential measurements indicated a relationship with the decomposition period of the waste, ie gradual increase in the electrical potential concomitant with the increase in the residence period of the waste. The occurrence of values close to zero in the ditch in 2007 and positive values and rising towards the older ditches indicates that the decomposition of organic waste produces electric potential that can be measured by geophysicist instrumental.

Decomposition processes of organic matter described in landfills involve the consumption of organic matter in aerobic and anaerobic stages, with oxygen consumption and generation of sub products such as $CH_4$ and $CO_2$. The high oxygen consumption in latest ditches rich in organic matter results in a reducing environment, characterized by values that tend to negative. The decreasing availability of this material produces progressively less reducing conditions, reflected in increasingly positive electrical potential.

The progressive increase of the electric potential values enabled a statistical analysis that revealed the need for about 8 years so that the values measured on the waste ditches are similar to the electric potential of the uncontaminated adjacent area.

This result is indicative of the average period for much of the organic matter consumption contained in domestic waste. However, the decomposition of waste such as paper, plastics and metals require tens to hundreds of years. The possibility of electric potential generation in this case is open to somewhat uncertain future studies.

The predominance of organic matter in the buried waste, existence of a deep groundwater and lack of metallic conductor ore body are elements that do not favor the application of the geobattery model in an attempt to understand the factors that are responsible for the generation of electric potential contrast measured in the study area.

Fixing the reference electrode in the external and topographically elevated area, different of the reading electrode moved to 241 measurement points and preferably fixed over waste ditches submitted to the action of organic matter decomposition processes, are elements that contribute to the understanding of the generation mechanism of natural electric potential in the study area, based on the proposed Nyquist and Corry (2002). In this case, the contrast is generated by the potential difference between the reference electrode and the movable electrode.

The likely predominance of the redox potential in the values generated by the decomposition of organic waste is indicative of the possibility of applying this geophysical method for monitoring areas contaminated by petroleum products.

Even though involving relatively high complexity processes, the decomposition of oil in soils also requires the consumption of oxygen in several degrees, which depend on concentrations of contaminants within a plume of contamination, as suggested by the works of Rabus and Heider (1998) and Thomas and Ward (1989). Therefore, similar results obtained in this work can also be achieved in areas contaminated by petroleum products.

## Acknowledgements

## Bibliography

Bagchi A., 1987, Natural attenuation mechanisms of landfill leachate and effects of various factors on the mechanism. *Waste Management Research*, 5, 453-464.

Baker S.S., Cull J.P., 2004, Streaming potential and groundwater contamination. *Exploration Geophysics*, 35, 41-44.

Barlaz M.A., Rooker A.P., Kjeldsen P., Gabr M.A., Borden R.C., 2002, A critical evaluation of factors required to terminate the post-closure monitoring period at solid waste landfills. *Environment Science & Technology*, 36, 16, 3457–64.

Birks J., Eyles C.A., 1997, Leachate from landfill along the Niagara Escarpment, in Environmental Geology of Urban Areas, Geological Association of Canada, Canada, 347-363.

Corry C.E., 1985, Spontaneous polarization associated with porphyry sulfide mineralization. *Geophysics*, 50, 6, 1020-1034.

Corwin R.F., 1990, The self-potential for environmental and engineering applications. In: Geotechnical and Environmental Geophysics, Tulsa: Society of Exploration Geophysics, *Investigations in Geophysics*, 5, 127-145.

Fang H.Y., 1995, Bacteria and tree root attack on landfill liners. In. Sarsby, R. W. (Ed.), Waste Disposal Landfill – GREEN'93. Rotterdam: A. A. Balkema, 419-426.

Farquhar G.J., 1989, Leachate: production and caracterization. *Canadian Journal of Civil Engineering*, 16, 317-325.

Gay S.P., 1967, A 1,800 millivolts self-potential anomaly near Hualgayoc, Peru. *Geophysics Prospecting*, 15, 236-245.

Landim P.M.B., 2004, Análise estatística de dados geológicos. Edunesp, São Paulo, 253 pp.

Meju M.A., 2000, Geoelectrical investigation of old/abandoned, covered landfill sites in urban areas: model development with a genetic diagnosis approach. *Journal of Applied Geophysics*, 44, 115-150.

Moreira C.A., Braga A.C.O, Fries M., 2009, Degradação de resíduos e alterações na resistividade elétrica, pH e Eh. Brasilian Geophysical Review, 27, 2, 283-293.

Moreira C.A., Braga A.C.O, Hansen M.A.F., 2011, Estimativa do tempo de produção de chorume em aterro controlado por meio de medidas de resistividade elétrica. *Brasilian Geoscience Review*, 44, 3, 549-557.

Mota R., Monteiro Santos F.A., Mateus A., Marques F.O., Gonçalves M.A., Figueiras J., Amaral H., 2004, Granite fracturing and incipient pollution beneath a recent landfill facility as detected by geoelectrical surveys. *Journal of Applied Geophysics*, 57, 11-22.

Naudet V., Revil A., Bottero J.Y., Bégassat P., 2003, Relationship between self-potential (SP) signals and redox conditions in contaminated groundwater. *Geophysical Research Letters*, 30, 21, 1-4.

Naudet V., Revil A., Rizzo E., Bottero J.Y., Bégassat P., 2004, Groundwater redox conditions in a contaminant plume from geoelectrical investigations. *Hydrogeology and Earth System Sciences*, 8, 1, 8-22.

Nimmer R. E., Osiensky J.L., 2002, Direct current and self-potential monitoring of an evolving plume in partially saturated fractured rock. *Journal of Hydrogeology*, 267, 258-272.

Nyquist J.E., Corry C.E., 2002, Self-potential: The ugly ducking of environmental geophysics. T*he Leading Edge*, 1, 446-451.

Rabus R., Heider J., 1998, Initial reactions of anaerobic metabolism of alkylbenzenes in denitrifying and sulfate-reducing bacteria. *Archives of Microbiology*, 170, 377-384.

Randnoff D., Hollingshead S., Anderson G., 1992, What legacy are we leaving with future landfill leachates? *Environmental Science & Technology*, 26, 58-60.

Sato M., Mooney H.D., 1960, The electrochemical mechanism of sulfide self-potential. *Geophysics*, 25, 1, 226-249.

Orellana E., 1972, Prospeccion Geoelectrica en Corriente Continua, Biblioteca Técnica Philips, Madrid: Paraninfo.

Petiau G., 2000, Second generation of Lead-Lead Chloride Electrodes for Geophysical applications. *Pure and Applied Geophysics*, 157, 357-382.

Themelis N.J., Ulloa P.A., 2007, Methane generation in landfills. *Renewable Energy*, 32, p. 1243-1257.

Thomas J.M., Ward C.H., 1989, In situ biorestoration of organic contaminants in the subsurface. *Environmental Science & Technology*, 23, 7, 760-766.

Telford W.M., Geldart L.P., Sheriff R.E., 1990, *Applied Geophysics*, 2º ed., Cambridge University Press: Cambridge.

# Measurements of upper mantle shear wave anisotropy from a permanent network in southern Mexico

Steven A. C. van Benthem, Raúl W. Valenzuela* and Gustavo J. Ponce

## Resumen

Se midió la anisotropía para las ondas de cortante en el manto superior por debajo de estaciones en el sur de México usando fases *SKS.* Las direcciones de polarización rápida donde la placa de Cocos se subduce subhorizontalmente están orientadas aproximadamente paralelas con el movimiento relativo entre las placas de Cocos y América del Norte y además son perpendiculares a la trinchera. Por lo tanto, se infiere que la placa subducida arrastra el manto que se encuentra por debajo y lo hace fluir (entrained flow). Una situación similar existe en la zona de subducción de Cascadia. Estudios previos han señalado que estas dos regiones tienen en común la subducción de litosfera joven. En aquellos lugares donde las placas subducidas muestran un cambio en el buzamiento o bien están rotas, se observa un cambio en la orientación de los ejes rápidos. Dichos cambios sugieren que se produce un flujo tridimensional alrededor de las orillas de las placas subducidas, el cual es consistente con el retroceso de la placa subducida (slab retreat or rollback), como ya se había observado en algunos trabajos anteriores. En algunas de las estaciones instaladas lejos de los límites de placa el movimiento absoluto de la placa de América del Norte controla las direcciones rápidas. El eje rápido de una estación ubicada en la Mesa Central se orienta ONO-ESE y es diferente de todas las demás mediciones en este estudio.

Palabras clave: Partición de ondas *SKS,* anisotropía del manto superior, flujo del manto, zonas de subducción, Fosa Mesoamericana, placas de Cocos, Rivera y América del Norte.

## Abstract

Upper mantle shear wave anisotropy under stations in southern Mexico was measured using records of *SKS* phases. Fast polarization directions where the Cocos plate subducts subhorizontally are oriented in the direction of the relative motion between the Cocos and North American plates, and are trench-perpendicular. This pattern is interpreted as subslab entrained flow, and is similar to that observed at the Cascadia subduction zone. Earlier studies have pointed out that both regions have in common the young age of the subducting lithosphere. Changes in the orientation of the fast axes are observed where the subducting plates change dip and/or are torn, and are thus indicative of 3-D flow around the slab edges. They are consistent with slab rollback, as previously shown by other authors. Some stations located away from the plate boundaries have their fast directions controlled by the absolute motion of the North American plate. The fast axis for station ZAIG, located in the Mesa Central, is oriented WNW-ESE and is different from all the other measurements in this study.

Key words: *SKS* splitting, upper mantle anisotropy, mantle flow, subduction zones, Middle America Trench, Cocos, Rivera, and North American plates.

G. J. Ponce
Departamento de Sismología
Instituto de Geofísica
Universidad Nacional Autónoma de México
Circuito de la Investigación S/N
Cd. Universitaria
Del. Coyoacán
04510. México, D.F., México

Also at Departamento de Geofísica
Facultad de Ingeniería
Universidad Nacional Autónoma de México
Mexico D.F., México

R. W. Valenzuela*
Departamento de Sismología
Instituto de Geofísica
Universidad Nacional Autónoma de México
Circuito de la Investigación S/N
Cd. Universitaria
Del. Coyoacán
04510. México, D.F., México
*Corresponding author: raul@ollin.igeofcu.unam.mx

S. A. C. van Benthem
Department of Earth Sciences
Utrecht University
Budapestlaan 4, 3584 CD Utrecht
The Netherlands

Formerly at Departamento de Sismología
Instituto de Geofísica
Universidad Nacional Autónoma de México
Mexico D.F., México

## Introduction

The use of the teleseismic phase *SKS* to study upper mantle anisotropy in both seismically quiet and seismically active regions has become a standard tool (Silver, 1996; Savage, 1999; Park and Levin, 2002). The method is based on the intrinsic anisotropy of the seismic velocity of the mineral olivine, which is one of the major components of the upper mantle. Olivine crystals become oriented as they are subjected to strain, usually caused by mantle flow. As the *SKS* phase travels through an anisotropic medium it becomes split, i. e. a fast and a slow wave are produced. Measurements of shear wave splitting yield two parameters: the fast polarization direction, $\phi$, usually referred to geographic north, and the delay time, $\delta t$. Laboratory experiments are essential to establish the relationship between the direction of mantle flow and the fast polarization direction in olivine. In general, these experiments have shown that the fast axis becomes oriented in the direction of mantle flow (Jung *et al.*, 2006). There is one notable exception, for type-B olivine the fast axis aligns perpendicular to the direction of mantle flow. From these results it is possible to infer the direction of mantle flow using seismic measurements. Connections between seismic anisotropy and the tectonic environment, whether it be active margins or stable continental interiors, have been made in the past (e. g., Silver, 1996; Savage, 1999; Park and Levin, 2002). Particularly, subduction zones have come under intense scrutiny; see Long and Silver (2008, 2009) for a review. Previous work in the case of Mexico has relied mostly on data from temporary deployments and has focused around the Gulf of California (Obrebski *et al.*, 2006; Obrebski and Castro, 2008; van Benthem *et al.*, 2008; Long, 2010), and on subduction of the Rivera and Cocos plates at the Middle America Trench (Stubailo and Davis, 2007, 2012a, 2012b; Bernal-Díaz *et al.*, 2008; Soto *et al.*, 2009; Rojo-Garibaldi, 2012). In the present article, data from a permanent broadband network has been used, thus covering a large area of the country with widely spaced stations. This approach stands in contrast to temporary deployments which usually cover smaller areas with a dense array.

## Data and Procedure

Most of the anisotropy measurements in this study used the *SKS* phase at epicentral distances greater than 90°. Additionally, other core-transmitted phases such as *sSKS, SKKS,* and *PKS* were used as available. Clear *SKS* readings at these distances required a minimum magnitude of 6.0, although occasionally smaller events proved useful. The records were provided by Mexico's Servicio Sismológico Nacional (SSN) broadband network (Singh *et al.*, 1997). The SSN database

was searched in the period from May 1998 to early January 2004. It provided a total of 359 earthquakes within the distance and magnitude criteria. Local problems with the equipment precluded the simultaneous recording of some events by all stations. The data were sampled 20 times per second using Streckeisen STS-2 broadband, three-component velocity sensors, except at station TEIG, where a Geotech KS36000 borehole seismometer was installed. Figure 1 shows the study area and the location of the 20 stations used.

The procedure used to measure anisotropy was explained by Silver and Chan (1991) and is presented here only briefly. The split *SKS* waves are observed in the fast and slow horizontal components, which are orthogonal. In general, these are different from the radial and transverse components, which are also orthogonal. In order to obtain $\phi$ and $\delta t$, a time segment containing the *SKS* arrival, or another *P* to *S* conversion at the core-mantle boundary (CMB), is selected from the north-south and east-west horizontal components. The two components are rotated by one degree at a time, with $\phi$ ranging between -90 and 90°. For each value of $\phi$, the components are time shifted relative to each other using increments of 0.05 s, with $\delta t$ ranging from 0 to 8 s. For each combination of $\phi$ and $\delta t$, the eigenvalues $\lambda_1$ and $\lambda_2$ of the covariance matrix between the two orthogonal components are evaluated. For an anisotropic medium, $\lambda_1$ and $\lambda_2$ will be different from zero. In the presence of noise, the desired solution will be given by the matrix which is most nearly singular. A grid search is then run through all combinations of ($\phi$, $\delta t$) within the space of possible solutions in order to choose the minimum eigenvalue, $\lambda_2^{min}$. The actual values of ($\phi$, $\delta t$) associated to $\lambda_2^{min}$ characterize the anisotropy because the highest cross-correlation within the given space occurs for the fast and slow waveforms. Sometimes the measurement returns a null value and splitting of the shear wave cannot be detected, as is the case for any of the three following situations. (1) $\delta t = 0$ s indicates the absence of anisotropy. (2) $\phi = \phi_b$ means that the fast axis, $\phi$, is oriented with the back azimuth, $\phi_b$. (3) $\phi = \phi_b + 90°$ means that the fast axis is perpendicular to the back azimuth.

Figure 2a shows the *SKS* arrival on the radial and transverse components at SSN station OXIG for the earthquake of May 16, 1998 south of the Fiji Islands. The hypocenter was located at 586 km depth and the epicentral distance was 90.10°. Table 1 lists the events used in this study to quantify upper mantle anisotropy. Each *SKS* waveform was chosen by visual inspection and a first order, bandpass Butterworth filter was applied. In every case an attempt was made to retain the broadest bandpass possible, but the actual corner frequencies were determined
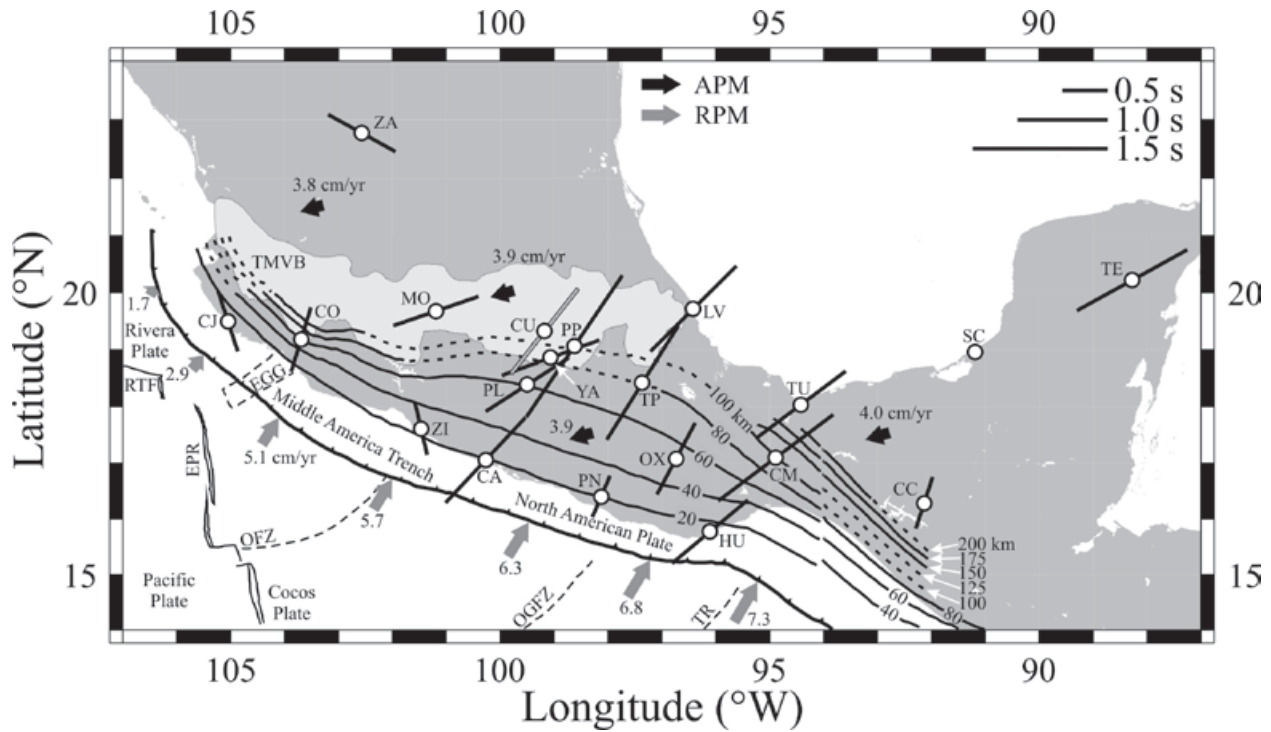
**Figure 1.** Average measurements of $\phi$ and $\delta t$ for stations in southern Mexico. The length of the black bars is proportional to $\delta t$, as indicated in the legend. The gray bar at CUIG represents a poorly constrained measurement. Black arrows indicate the direction of absolute motion for the North American plate. Gray arrows show the direction of the relative plate motions for either the small Rivera (northwest) or the larger Cocos (southeast) plate relative to North America. Velocities are given in cm/yr for both the APM and the RPM. The Middle America Trench is represented by the line with small triangles. The Trans-Mexican Volcanic Belt (TMVB) is indicated by the light shading. Solid lines represent the isodepth contours of hypocenters within the subducting Rivera and Cocos plates. Lines are dashed where no hypocenters were available. Contours west of 94°W are from Pardo and Suárez (1995) while contours east of 94°W are from Rodríguez-Pérez (2007). In all cases, contours deeper than 100 km are from Rodríguez-Pérez (2007). Also shown are the Rivera Transform Fault (RTF), East Pacific Rise (EPR), El Gordo Graben (EGG), Orozco Fracture Zone (OFZ), O'Gorman Fracture Zone (OGFZ), and Tehuantepec Ridge (TR). Four-letter station codes were shortened by dropping the -IG ending common to all of them.

based on the frequency of the noise affecting each record. The low frequency corner was chosen in the range from 0.01 to 0.04 Hz (periods between 100 and 25 s) while the high frequency corner varied between 1.0 and 1.5 Hz (from 1 to 0.67 s), which is appropriate for the phases used and the expected delay times (Wolfe and Silver, 1998). A time segment including only the selected phase was cut from the seismogram. In Figure 2 the time series is 33 s long and is typical of the record lengths used throughout this work. Figure 3 shows the combination of $(\phi, \delta t)$ producing the minimum eigenvalue, $\lambda_2^{min}$. The black dot means that the delay time, $\delta t$, is 1.05 s and the fast axis, $\phi$, is 8° east of north. The first contour around the dot bounds the 95% confidence interval for the measurement. All the



**Figure 2.** *SKS* wave from the event of May 16, 1998 south of the Fiji Islands (22.14°S, 179.70°W, h = 586 km, M = 5.9) recorded at broadband station Oaxaca (OXIG). The epicentral distance is 90.10°. (a) The radial and transverse velocity components are shown. (b) The radial and transverse components are shown after correcting for splitting using the values that were measured.

**Table 1.** Source parameters of the earthquakes used to measure upper mantle anisotropy.

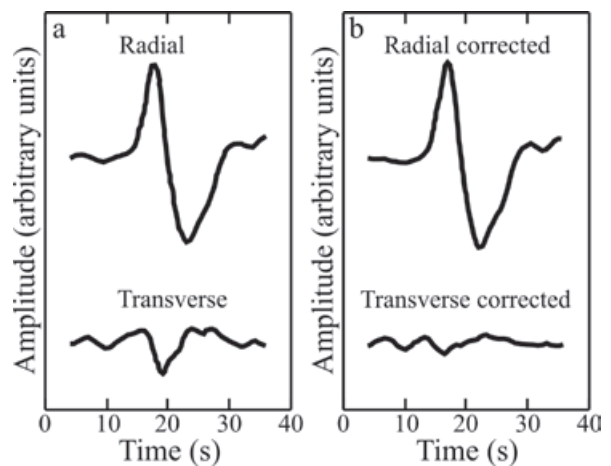| Date Y/M/D | Origin time H:M:S | Lat. (°N) | Long. (°E) | Depth (km) | Mag. | Location |
|---|---|---|---|---|---|---|
| 1998/05/16 | 02:22:03 | -22.14 | -179.70 | 586 | 5.9 | South of Fiji Islands |
| 1998/08/20 | 06:40:52 | 28.97 | 139.40 | 400 | 6.2 | Bonin Islands region |
| 1998/11/08 | 07:25:49 | -8.90 | 121.43 | 10 | 6.3 | Flores region, Indonesia |
| 1999/02/22 | 01:00:32 | -21.52 | 169.66 | 10 | 6.4 | Loyalty Islands region |
| 1999/04/05 | 11:07:52 | -5.31 | 149.84 | 10 | 7.4 | New Britain region, Papua New Guinea |
| 1999/04/08 | 13:10:34 | 43.60 | 130.53 | 560 | 7.2 | Eastern Russia-northeastern China |
| 1999/04/13 | 10:38:47 | -21.38 | -176.54 | 163 | 6.6 | Fiji Islands region |
| 1999/04/20 | 19:04:08 | -31.83 | -179.07 | 96 | 6.5 | Kermadec Islands |
| 1999/05/12 | 17:59:21 | 43.02 | 143.84 | 98 | 6.2 | Hokkaido region, Japan |
| 1999/05/17 | 10:07:59 | -4.56 | 152.96 | 10 | 6.9 | New Ireland region, Papua New Guinea |
| 1999/07/07 | 18:52:57 | 49.25 | 155.54 | 10 | 6.2 | Kuril Islands |
| 1999/07/28 | 10:08:21 | -30.24 | -177.98 | 10 | 6.2 | Kermadec Islands |
| 1999/08/01 | 08:39:08 | -30.44 | -177.84 | 10 | 6.4 | Kermadec Islands |
| 1999/10/18 | 02:43:24 | -56.00 | -26.50 | 10 | 6.1 | South Sandwich Islands region |
| 1999/11/12 | 16:57:20 | 40.77 | 31.15 | 10 | 7.2 | Turkey |
| 1999/11/26 | 13:21:15 | -16.45 | 168.18 | 10 | 7.1 | Vanuatu Islands |
| 2000/01/08 | 01:19:46 | -9.93 | 160.05 | 10 | 6.4 | Solomon Islands |
| 2000/03/28 | 11:00:20 | 22.41 | 143.59 | 116 | 7.7 | Volcano Islands region, Japan |
| 2000/05/06 | 13:44:17 | -11.26 | 165.41 | 10 | 6.3 | Santa Cruz Islands |
| 2000/06/06 | 14:57:02 | 29.47 | 131.41 | 10 | 6.0 | Southeast of Ryukyu Islands |
| 2000/06/14 | 02:15:25 | -25.57 | 177.97 | 604 | 6.4 | South of Fiji Islands |
| 2000/08/15 | 04:30:09 | -31.52 | 179.68 | 358 | 6.6 | Kermadec Islands region |
| 2000/08/21 | 09:16:25 | -53.08 | -46.32 | 10 | 6.1 | South Atlantic Ocean |
| 2000/08/28 | 19:29:26 | -4.15 | 127.21 | 48 | 6.4 | Banda Sea |
| 2000/10/29 | 08:37:03 | -5.18 | 154.00 | 100 | 6.3 | Solomon Islands |
| 2000/11/07 | 00:18:06 | -55.25 | -29.18 | 10 | 6.8 | South Sandwich Islands region |
| 2000/11/17 | 21:01:56 | -5.49 | 151.66 | 10 | 7.5 | New Britain region, Papua New Guinea |
| 2001/01/26 | 03:16:41 | 23.40 | 70.32 | 24 | 7.9 | Southern India |
| 2002/04/26 | 16:06:06 | 13.11 | 144.56 | 85 | 7.1 | Mariana Islands |
| 2002/05/08 | 05:26:00 | -17.94 | -174.65 | 131 | 6.3 | Tonga Islands |
| 2002/06/06 | 23:53:51 | -0.88 | 148.20 | 10 | 6.3 | Admiralty Islands, Papua New Guinea |
| 2002/06/22 | 02:58:20 | 35.63 | 48.95 | 10 | 6.5 | Western Iran |
| 2002/06/28 | 17:19:30 | 43.77 | 130.72 | 564 | 7.3 | Eastern Russia-northeastern China |
| 2002/08/02 | 23:11:39 | 29.32 | 139.04 | 425 | 6.2 | Southeast of Honshu, Japan |
| 2002/08/15 | 05:30:29 | -1.25 | 121.36 | 10 | 6.2 | Sulawesi, Indonesia |
| 2002/08/19 | 11:01:01 | -21.80 | -179.49 | 587 | 7.6 | Fiji Islands region |
| 2002/09/08 | 18:44:26 | -3.24 | 142.89 | 10 | 7.6 | New Guinea, Papua New Guinea |
| 2002/09/15 | 08:39:31 | 44.86 | 130.08 | 578 | 6.5 | Northeastern China |
| 2002/10/04 | 19:05:50 | -20.82 | -179.00 | 627 | 6.4 | Fiji Islands region |
| 2002/10/14 | 14:12:43 | 41.34 | 142.06 | 58 | 6.1 | Hokkaido region, Japan |
| 2002/10/22 | 11:39:04 | -20.47 | -178.62 | 552 | 6.2 | Fiji Islands region |
| 2003/01/20 | 08:43:06 | -10.42 | 160.70 | 10 | 7.3 | Solomon Islands |
| 2003/02/10 | 04:49:30 | -6.02 | 149.82 | 10 | 6.3 | New Britain region, Papua New Guinea |
| 2003/03/02 | 16:42:56 | -36.80 | -20.73 | 10 | 6.2 | Southern Mid-Atlantic Ridge |
| 2003/03/11 | 07:27:32 | -4.70 | 153.13 | 10 | 6.8 | New Ireland region, Papua New Guinea |
| 2003/05/13 | 21:21:13 | -17.40 | 167.66 | 10 | 6.2 | Vanuatu Islands |
| 2003/05/21 | 18:44:18 | 36.88 | 3.73 | 10 | 6.8 | Northern Algeria |
| 2003/06/12 | 08:59:20 | -5.94 | 154.70 | 185 | 6.2 | Bougainville region, Papua New Guinea |
| 2003/08/04 | 04:37:20 | -60.56 | -43.49 | 10 | 7.5 | Scotia Sea |
| 2003/08/21 | 12:12:50 | -45.18 | 167.12 | 10 | 7.0 | South Island of New Zealand |
| 2003/09/26 | 20:38:21 | 42.05 | 144.47 | 10 | 6.0 | Hokkaido region, Japan |
| 2003/09/29 | 02:36:54 | 42.44 | 144.39 | 10 | 6.5 | Hokkaido region, Japan |
| 2003/10/08 | 09:06:55 | 42.66 | 144.49 | 10 | 6.7 | Hokkaido region, Japan |
| 2003/10/18 | 22:27:13 | 0.52 | 126.05 | 10 | 6.4 | Molucca Sea |
| 2003/10/31 | 01:06:28 | 37.83 | 142.59 | 10 | 7.0 | Honshu, Japan |
| 2003/12/27 | 16:00:59 | -22.03 | 169.65 | 10 | 7.3 | Southeast of the Loyalty Islands |
| 2004/01/03 | 16:23:18 | -22.30 | 169.70 | 10 | 7.1 | Southeast of the Loyalty Islands |

**Figure 3.** Contour plot showing the minimum value in $(\phi, \delta t)$-space as indicated by the dot. In this case the fast polarization direction is N8°E and the delay time is 1.05 s. The first contour around the dot bounds the 95% confidence region.

other contours are multiples of the first one and are located at higher "elevations" or mountains. The black dot is located at the bottom of a valley. The 95% confidence contour was calculated using equation (16) in Silver and Chan (1991) and taking one degree of freedom for each second of the record containing the *SKS* arrival (Silver and Chan, 1991; K. M. Fischer, Brown University, personal communication, 1998). The uncertainties are read directly from the contour plots. In this case, the measurement with its $\pm 1\sigma$ uncertainty is $(\phi, \delta t) = (8\pm27°, 1.05\pm0.65 \text{ s})$. In the event that the 95% confidence region is not approximately symmetric, the largest of the two possible $1\sigma$ values is used, i. e. in going from 8° to 35°, as opposed to going from 8° to -5° (Figure 3). The contour plots are also useful to gauge the quality of the measurements. For example, a large 95% confidence area means that the parameters are poorly constrained. If multiple minima occur then the measurement is not reliable. Another possibility is that the 95% contour does not close, thus indicating a null measurement. All the individual splitting measurements are reported in Table 2.

It is important to run a number of checks in order to make sure that the observation of *SKS* energy on the transverse component is indeed the result of anisotropy and does not arise from a different process such as scattering (Silver and Chan, 1991; Savage, 1999). Likewise, these checks mean that the values determined for $\phi$ and $\delta t$ are reliable. (1) An "unsplitting" correction is applied to the radial and transverse records using the estimated splitting parameters. If $(\phi, \delta t)$ do describe anisotropy, then the *SKS* wave must disappear, or at least its amplitude is decreased, from the corrected transverse component (Figure 2b). Similarly, the amplitude of *SKS* is increased on the corrected radial component, although this effect is small. (2) The particle motion of the *SKS* arrival in the transverse component is plotted as function of the radial component. Before the unsplitting correction, particle motion must be approximately elliptical (Figure 4a), and after correction it becomes nearly linear (Figure 4b). (3) The N-S and E-W records are rotated through the



**Figure 4.** A further check was a comparison of the particle motion in the transverse component as a function of the radial. (a) Before correcting for the anisotropy the particle motion is elliptical. (b) After a correction for the measured anisotropy is applied, the particle motion becomes close to linear.
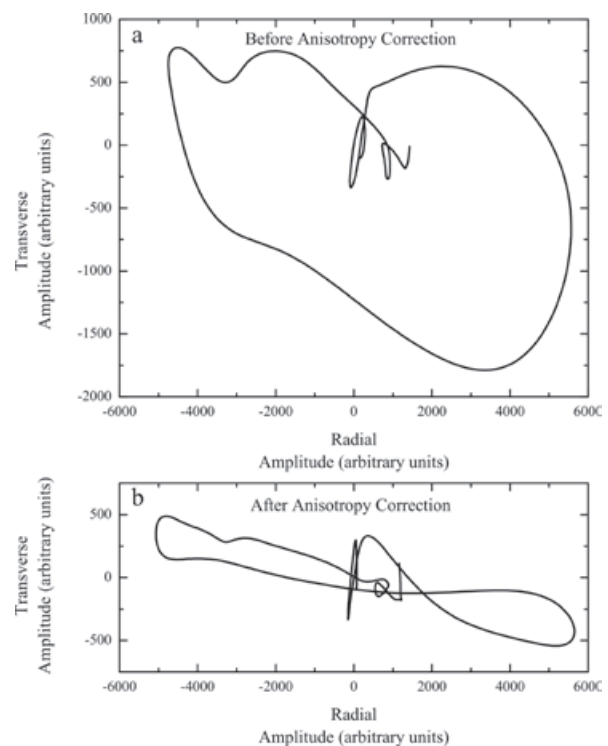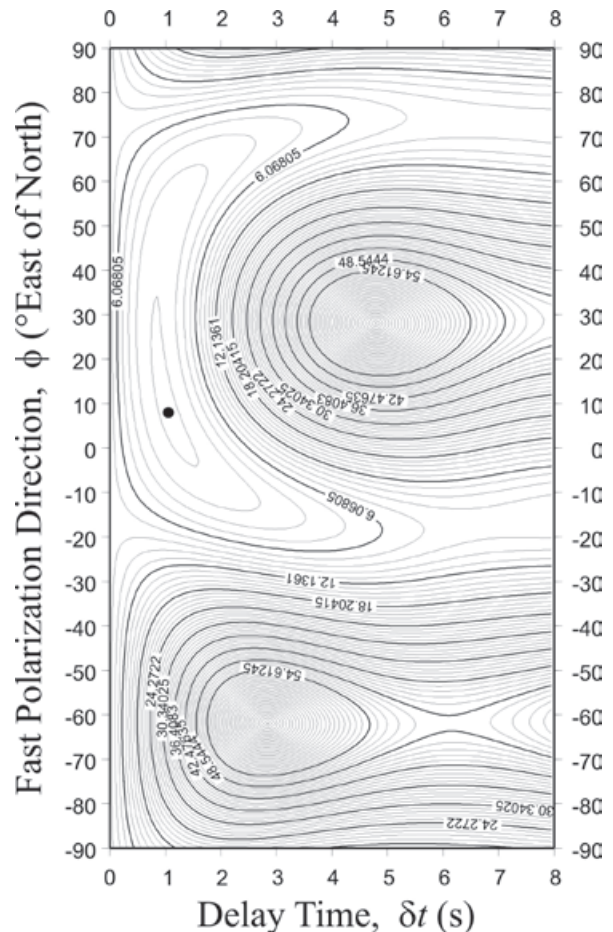
**Table 2.** Individual splitting parameters measured at each station.

| Station | Date Y/M/D | $\varphi_b$ (°) | Phase | $\varphi$ (°) | $\sigma_\varphi$ (°) | $\delta t$ (s) | $\sigma_{\delta t}$ (s) |
|---------|------------|------------------|-------|----------------|-----------------------|-----------------|--------------------------|
| CAIG | 2000/03/28 | 300.22 | SKS  | -84 | 51 | 0.95 | 0.85 |
|      | 2000/03/28 | 300.22 | sSKS | 37  | 38 | 2.25 | 1.65 |
|      | 2002/06/28 | 324.69 | SKS  | 42  | 77 | 1.10 | 1.60 |
|      | 2003/05/13 | 254.08 | SKS  | 50  | 31 | 1.60 | 0.90 |
|      | 2003/10/31 | 314.47 | SKS  | 42  | -  | -    | -    |
| CCIG | 2002/06/28 | 328.76 | SKS  | -13 | 66 | 0.50 | 4.20 |
|      | 2003/05/13 | 255.90 | SKS  | 48  | 45 | 0.80 | 1.00 |
|      | 2003/09/29 | 320.97 | SKS  | -19 | 55 | 0.70 | 1.90 |
| CJIG | 1998/05/16 | 244.16 | SKS  | -31 | -  | -    | -    |
|      | 2000/08/21 | 148.88 | SKS  | -23 | 12 | 1.35 | 0.55 |
|      | 2002/06/28 | 322.76 | SKS  | -17 | 11 | 0.55 | 0.30 |
|      | 2002/08/19 | 244.39 | SKS  | -31 | -  | -    | -    |
|      | 2002/10/04 | 245.10 | SKS  | -41 | -  | -    | -    |
| CMIG | 2002/04/26 | 293.39 | sSKS | 20  | -  | -    | -    |
|      | 2002/06/22 | 32.68  | SKKS | 44  | -  | -    | -    |
|      | 2002/10/04 | 248.63 | SKS  | 54  | 5  | 1.70 | 0.50 |
|      | 2002/10/22 | 248.86 | SKS  | 52  | -  | -    | -    |
|      | 2003/05/13 | 255.45 | SKS  | 50  | 60 | 1.00 | 0.90 |
|      | 2003/08/04 | 157.23 | SKS  | 67  | -  | -    | -    |
|      | 2003/08/21 | 227.36 | SKS  | 54  | -  | -    | -    |
|      | 2003/10/31 | 316.79 | SKS  | 51  | -  | -    | -    |
| COIG | 1999/04/05 | 270.48 | SKS  | 24  | 38 | 0.80 | 1.00 |
|      | 2000/03/28 | 299.22 | SKS  | 18  | -  | -    | -    |
|      | 2000/05/06 | 259.82 | SKS  | 48  | 59 | 1.15 | 1.15 |
|      | 2002/10/14 | 316.57 | SKS  | -30 | 42 | 1.10 | 0.60 |
|      | 2003/05/13 | 253.32 | SKS  | 17  | 41 | 0.60 | 0.90 |
|      | 2003/05/21 | 49.85  | SKS  | 44  | -  | -    | -    |
|      | 2003/06/12 | 268.28 | SKS  | 72  | 64 | 0.85 | 0.95 |
| CUIG | 2000/05/06 | 261.25 | SKS  | 38  | 55 | 1.20 | 1.25 |
| HUIG | 1999/02/22 | 250.44 | SKS  | 59  | -  | -    | -    |
|      | 1999/04/13 | 247.08 | SKS  | 65  | -  | -    | -    |
|      | 1999/07/07 | 321.63 | SKS  | 51  | -  | -    | -    |
|      | 1999/07/28 | 239.08 | SKS  | 63  | -  | -    | -    |
|      | 1999/08/01 | 238.85 | SKS  | 63  | -  | -    | -    |
|      | 1999/11/26 | 255.74 | SKS  | 66  | -  | -    | -    |
|      | 2000/05/06 | 261.50 | SKS  | 50  | 43 | 1.10 | 0.60 |
|      | 2000/06/14 | 244.58 | SKS  | 63  | -  | -    | -    |
|      | 2002/10/04 | 248.31 | SKS  | 66  | -  | -    | -    |
|      | 2002/10/22 | 248.54 | SKS  | 59  | -  | -    | -    |
|      | 2003/05/13 | 254.93 | SKS  | 66  | -  | -    | -    |
| LVIG | 1998/05/16 | 247.19 | SKS  | 43  | 11 | 1.15 | 0.55 |
|      | 2003/05/13 | 255.57 | SKS  | 44  | 56 | 1.45 | 1.75 |
|      | 2003/12/27 | 250.52 | SKS  | 46  | 65 | 1.60 | 2.60 |
|      | 2004/01/03 | 250.24 | SKS  | 47  | 12 | 1.40 | 0.70 |

**Table 2.** Continuation.

| Station | Date Y/M/D | $\varphi_b$ (°) | Phase | $\varphi$ (°) | $\sigma_\varphi$ (°) | $\delta t$ (s) | $\sigma_{\delta t}$ (s) |
|---------|------------|-----------------|-------|---------------|----------------------|----------------|-------------------------|
| MOIG | 2000/08/15 | 237.13 | SKS | -60 | 47 | 0.90 | 0.80 |
|      | 2002/06/22 | 27.29 | SKKS | 55 | 26 | 0.95 | 0.35 |
|      | 2002/08/15 | 288.85 | PKS | 25 | - | - | - |
|      | 2002/08/19 | 245.80 | SKS | -85 | 50 | 0.45 | 1.25 |
|      | 2002/09/15 | 325.72 | SKS | 77 | 18 | 1.35 | 0.55 |
|      | 2002/09/15 | 325.72 | SKKS | 51 | - | - | - |
|      | 2003/10/08 | 317.76 | SKS | 89 | - | - | - |
| OXIG | 1998/05/16 | 247.05 | SKS | 8 | 27 | 1.05 | 0.65 |
|      | 1999/04/08 | 326.42 | SKS | 42 | 30 | 1.20 | 0.70 |
|      | 1999/04/20 | 237.71 | SKS | 49 | 13 | 1.35 | 0.45 |
|      | 1999/05/12 | 319.87 | SKS | 38 | 60 | 1.75 | 1.65 |
|      | 1999/10/18 | 147.96 | SKS | 35 | 22 | 1.20 | 0.40 |
|      | 2000/03/28 | 301.82 | SKS | 32 | - | - | - |
|      | 2000/08/28 | 281.77 | PKS | 7 | - | - | - |
|      | 2002/08/02 | 310.28 | SKS | 32 | 7 | 2.15 | 0.65 |
|      | 2002/09/08 | 276.40 | SKS | 28 | 55 | 1.15 | 1.55 |
|      | 2002/09/15 | 327.60 | SKS | 11 | 33 | 0.65 | 0.40 |
|      | 2002/10/04 | 248.09 | SKS | 41 | 23 | 0.85 | 0.45 |
|      | 2003/05/13 | 254.99 | SKS | 41 | 26 | 1.35 | 0.55 |
|      | 2003/10/08 | 319.30 | SKS | 35 | 23 | 1.25 | 1.20 |
| PLIG | 1999/04/08 | 325.21 | SKS | 70 | 10 | 2.00 | 1.00 |
|      | 1999/05/17 | 271.32 | SKS | 38 | 19 | 1.70 | 0.30 |
|      | 1999/10/18 | 147.24 | SKS | -18 | 68 | 1.05 | 0.55 |
|      | 1999/11/12 | 36.62 | SKS | 70 | 38 | 1.25 | 0.75 |
|      | 2000/03/28 | 300.90 | SKS | 58 | 34 | 0.95 | 0.75 |
|      | 2000/03/28 | 300.90 | sSKS | 34 | 14 | 2.15 | 1.15 |
|      | 2000/05/06 | 261.01 | SKS | 13 | 10 | 1.35 | 0.45 |
|      | 2000/06/06 | 313.39 | SKS | 51 | - | - | - |
|      | 2000/06/14 | 243.71 | SKS | 32 | 46 | 0.65 | 0.85 |
|      | 2000/08/15 | 237.62 | SKS | 46 | 56 | 1.00 | 1.20 |
|      | 2002/04/26 | 291.79 | sSKS | 42 | 65 | 0.70 | 0.80 |
|      | 2002/06/28 | 325.24 | SKS | 73 | 7 | 1.85 | 0.65 |
|      | 2002/08/02 | 309.22 | SKS | 54 | 86 | 0.80 | 1.20 |
|      | 2002/08/19 | 246.43 | SKS | 52 | 18 | 0.95 | 0.55 |
|      | 2002/09/08 | 276.11 | SKS | 5 | - | - | - |
|      | 2002/09/15 | 326.39 | SKS | 73 | 8 | 2.05 | 1.05 |
|      | 2002/10/04 | 247.18 | SKS | 23 | 30 | 0.70 | 0.50 |
|      | 2003/01/20 | 263.19 | SKS | 67 | 13 | 1.85 | 0.85 |
|      | 2003/02/10 | 270.86 | SKS | 16 | 50 | 1.55 | 0.75 |
|      | 2003/05/13 | 254.46 | SKS | 19 | 23 | 1.05 | 0.35 |
|      | 2003/08/21 | 227.12 | SKS | 50 | - | - | - |
|      | 2003/10/18 | 287.97 | PKS | 40 | 20 | 1.50 | 0.70 |
| PNIG | 1998/08/20 | 308.92 | SKS | 20 | - | - | - |
|      | 1999/10/18 | 147.65 | SKS | 23 | 73 | 0.45 | 2.55 |
|      | 2000/03/28 | 300.98 | SKS | 16 | - | - | - |
|      | 2000/03/28 | 300.98 | sSKS | 14 | - | - | - |
|      | 2002/06/28 | 325.63 | SKS | 26 | 51 | 0.50 | 0.40 |
|      | 2002/09/15 | 326.79 | SKS | 18 | 58 | 0.60 | 2.20 |
| PPIG | 2000/01/08 | 264.29 | SKS | 31 | 51 | 1.40 | 1.55 |
|      | 2001/01/26 | 14.73 | PKS | 32 | 9 | 2.15 | 0.75 |
|      | 2002/09/08 | 276.79 | SKS | 24 | 14 | 2.15 | 0.85 |
|      | 2003/08/04 | 156.03 | SKS | 22 | 56 | 1.80 | 2.55 |

**Table 2.** Continuation.

| Station | Date Y/M/D | $\varphi_b$ (°) | Phase | $\varphi$ (°) | $\sigma_\varphi$ (°) | $\delta t$ (s) | $\sigma_{\delta t}$ (s) |
|---------|------------|------|-------|------|------|------|------|
| SCIG | 2002/05/08 | 251.16 | SKS | -16 | - | - | - |
|      | 2003/03/02 | 130.64 | SKS | -49 | - | - | - |
| TEIG | 1998/05/16 | 249.78 | SKS | 61 | 19 | 1.40 | 0.90 |
|      | 1999/04/08 | 331.62 | SKS | 59 | - | - | - |
|      | 1999/05/12 | 323.97 | SKS | 67 | - | - | - |
|      | 2002/06/28 | 331.62 | SKS | 60 | - | - | - |
|      | 2003/08/04 | 159.58 | SKS | 70 | - | - | - |
| TPIG | 2003/03/11 | 271.81 | SKS | 35 | 13 | 1.50 | 0.30 |
|      | 2003/06/12 | 270.07 | SKS | 32 | 21 | 1.45 | 0.55 |
|      | 2003/08/21 | 227.39 | SKS | 44 | - | - | - |
| TUIG | 1998/05/16 | 247.75 | SKS | 53 | 49 | 1.25 | 1.25 |
|      | 1999/05/12 | 320.91 | SKS | 52 | - | - | - |
|      | 1999/10/18 | 148.51 | SKS | 66 | - | - | - |
|      | 2002/08/02 | 311.75 | SKS | 44 | - | - | - |
| YAIG | 1998/05/16 | 246.31 | SKS | 55 | 66 | 0.40 | 1.20 |
|      | 1999/11/12 | 36.77 | SKS | 61 | 22 | 1.40 | 0.70 |
|      | 2000/03/28 | 301.22 | SKS | 56 | 14 | 2.15 | 0.85 |
|      | 2000/03/28 | 301.22 | sSKS | 70 | 24 | 1.05 | 0.55 |
|      | 2000/08/15 | 237.77 | SKS | 70 | - | - | - |
|      | 2002/06/28 | 325.52 | SKS | 82 | - | - | - |
|      | 2002/09/15 | 326.66 | SKS | 78 | - | - | - |
|      | 2003/01/20 | 263.43 | SKS | 89 | - | - | - |
|      | 2003/09/26 | 318.17 | SKS | 74 | - | - | - |
|      | 2003/09/29 | 318.38 | SKS | 70 | 33 | 1.60 | 1.25 |
|      | 2003/10/31 | 315.19 | SKS | 52 | - | - | - |
| ZAIG | 1998/11/08 | 281.19 | PKS | -78 | - | - | - |
|      | 1999/05/17 | 271.54 | SKS | -87 | - | - | - |
|      | 1999/10/18 | 146.14 | SKS | -57 | 27 | 1.05 | 0.45 |
|      | 2000/06/14 | 242.75 | SKS | -62 | 28 | 0.90 | 0.40 |
|      | 2000/08/15 | 236.74 | SKS | -64 | 28 | 0.75 | 0.35 |
|      | 2000/10/29 | 270.55 | SKS | -88 | - | - | - |
|      | 2000/11/07 | 146.11 | SKS | -89 | 38 | 1.00 | 1.00 |
|      | 2000/11/17 | 271.17 | SKS | -78 | - | - | - |
|      | 2002/06/06 | 276.99 | SKS | -80 | - | - | - |
|      | 2002/08/19 | 245.14 | SKS | -60 | 16 | 0.85 | 0.20 |
|      | 2002/10/14 | 317.17 | SKS | -56 | 40 | 1.10 | 1.00 |
| ZIIG | 1999/04/08 | 324.15 | SKS | -16 | 37 | 0.55 | 0.35 |
|      | 1999/04/08 | 324.15 | SKKS | -29 | 92 | 1.45 | 2.05 |
|      | 2002/06/28 | 324.19 | SKS | -8 | 32 | 0.50 | 0.35 |
|      | 2002/09/15 | 325.35 | SKKS | -14 | 71 | 1.20 | 1.75 |

Dates of the earthquakes and the phases used to measure individual splitting parameters at each station. $\varphi_b$ is the back azimuth. Parameter $\varphi$ is the fast polarization direction (measured east of north), $\delta t$ is the delay time, and $\sigma_\varphi$ and $\sigma_{\delta t}$ are the 1$\sigma$ uncertainties.
Null measurements are represented with a nonzero value for $\varphi$ and dashes for the next three columns. Therefore, any of the three following situations could occur for the particular earthquake-to-station path being considered: $\varphi \approx \varphi_b$, $\varphi \approx \varphi_b \pm 90°$, or $\delta t \approx 0$ s. The actual value listed for $\varphi$ is used as a possible interpretation of the data and is intended as additional information where appropriate.

angle $\phi$ to obtain the slow and fast components of the *SKS* pulse. The fast and slow waveforms must have roughly the same shape and the fast *SKS* must arrive before the slow *SKS* by an amount approximately equal to the measured $\delta t$ (Figure 5). Shifting the slow wave forward by a time $\delta t$ should align it with the fast wave.
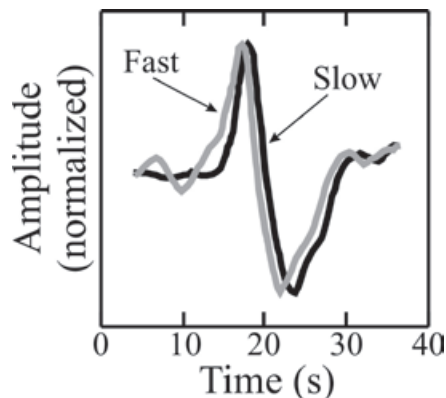


**Figure 5.** Once the fast polarization direction is known, the N-S and E-W horizontal records are rotated through the angle $\phi$ in order to obtain the slow and fast components of the *SKS* pulse. These are shown normalized to the same amplitude.

## Results

Table 1 lists the events that provided useful data for this study. Earthquake information includes the date, origin time, hypocenter, magnitude, and the geographic location. A total of 136 individual splitting measurements were made at twenty different stations and are given in Table 2. The parameters are the fast polarization direction and the delay time, both with their corresponding $1\sigma$ uncertainties. Also provided are the date of the event, the back azimuth, and the phase used (*SKS, SKKS, sSKS,* or *PKS*). The observed orientations of the fast polarization direction practically span the whole space of possible solutions, from -90 to 90°. The smallest $1\sigma_\phi$ uncertainty for the fast polarization direction is 5°, while the largest is 92°. The latter value is quite large and such an estimate normally would not be reliable. In general, such large uncertainties arise from a poor signal-to-noise ratio. We allowed large uncertainties for a few measurements if the data at the station were scarce. Furthermore, Wolfe and Silver (1998) showed that in certain cases, stacking measurements with large error regions can lead to improved estimates of the splitting parameters. As explained below, our measurements for each station were averaged using the stacking method proposed by Wolfe and Silver (1998) and consequently have smaller $1\sigma$ uncertainties than the individual measurements. It

is worth mentioning that the average uncertainty in Table 2 is 37°. The smallest delay time is 0.40 s and the largest is 2.25 s. The average delay time is 1.20 s. The smallest $1\sigma_{\delta t}$ uncertainty for the delay time is 0.20 s, and the largest is 4.20 s at station CCIG, although this is an extreme value. The second largest $1\sigma_{\delta t}$ uncertainty is 2.60 s. The average uncertainty, however, is much lower at 0.96 s. The station with the largest number of observations is PLIG with nineteen records showing clearly split waveforms and three null measurements given that it had the largest number of records meeting the selection criteria previously explained. Station CUIG had the fewest observations, only one with a clearly split waveform was available. Since this station is located within Mexico City, cultural noise is certainly a problem. On average, 6.8 measurements are reported per station. Some sites are noisier than others. Additionally, the stations were not installed simultaneously and some of them had been running for only a short time when the data for this study were gathered. Even though records from 359 different earthquakes were analyzed, only 57 of them generated observable *P* to *S* CMB conversions at the various stations. The individual splitting parameters are shown in Figure 6.

Average splitting parameters were calculated for each station using the stacking method of Wolfe and Silver (1998). The error surface associated to the contour plot of each individual measurement is normalized by its minimum eigenvalue, $\lambda_{2,i}^{min}$. The normalized error surfaces from all measurements at the station are then summed. In this way, the best splitting parameters are given by the minimum value of the sum and a new 95% confidence interval is obtained. As the noise properties vary for different earthquakes, stacking events with a similar polarization improves the final result (Wolfe and Silver, 1998). Therefore, the size of the 95% confidence region for the averaged values is smaller than for the individual measurements. The averaged splitting parameters are presented in Table 3, which includes the fast polarization direction and the delay time, both with their corresponding $1\sigma$ uncertainties, as well as the stations' coordinates and geographic location, and the total number of clearly split and null measurements. In this case, the smallest $1\sigma_\phi$ uncertainty for the fast polarization direction is 4°, while the largest is 21°. Strictly speaking, there are three uncertainties of 55, 43, and 49° at stations CUIG, HUIG, and TUIG, respectively. These stations only had one split measurement each and so the individual measurement is reported as the average. As shown in Table 2 and in Figure 6, the results at stations HUIG and TUIG are considered reliable because they also had null measurements consistent with the only split value reported. The average $1\sigma_\phi$ uncertainty in Table 3 is 16°. The smallest delay time is 0.50 s and the
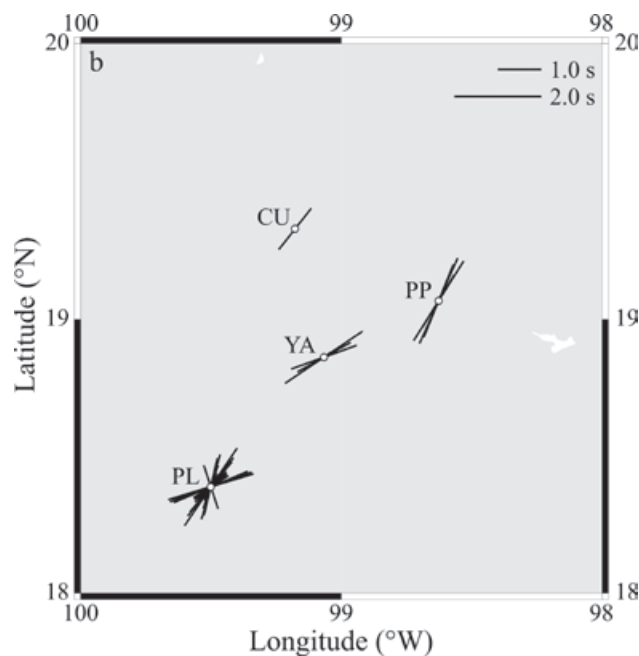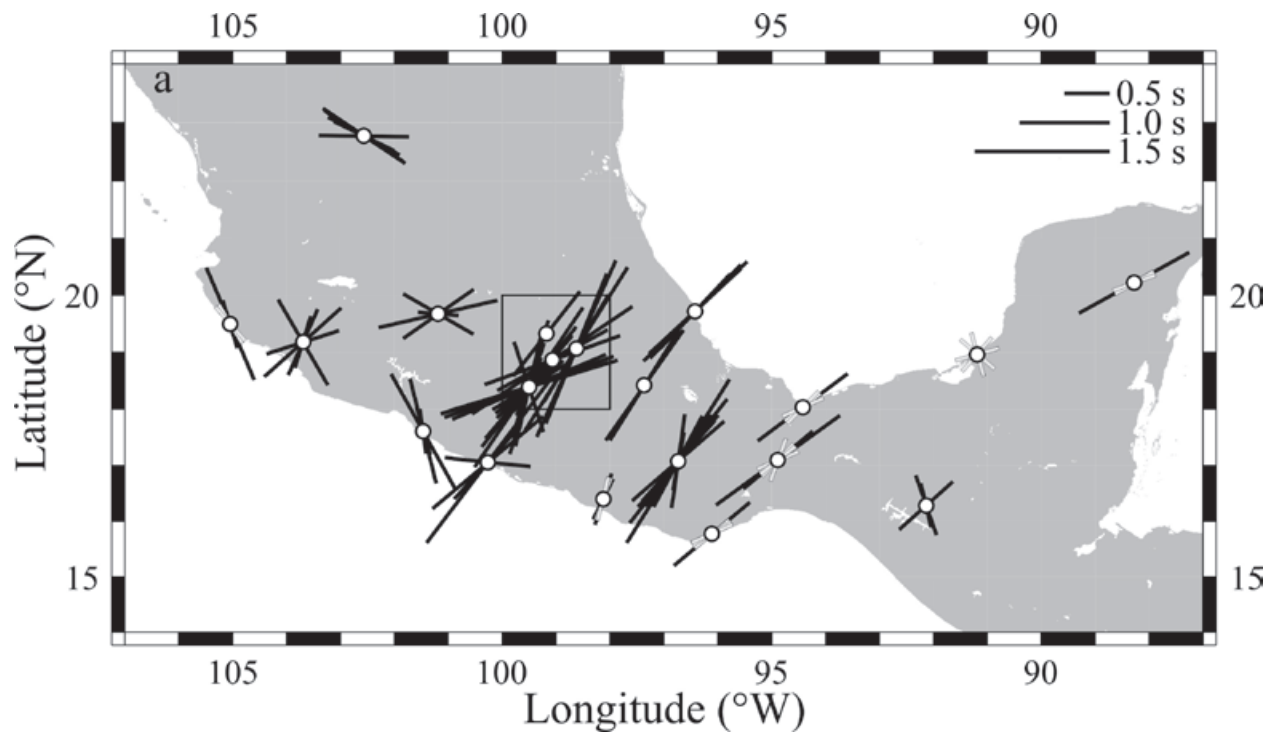
**Figure 6.** (a) Individual measurements of $\phi$ and $\delta t$ at stations in southern Mexico. Symbols are as in Figure 1. Additionally, null measurements from two nonorthogonal back azimuths are represented by the white bars (forming two crosses) for station SCIG, which is interpreted to have splitting below the threshold of the data. Other null measurements are shown only for stations with a few well constrained splitting measurements. The fast directions for these null measurements were chosen to be consistent with the split observations. The box represents the area shown as an inset in (b).

largest is 1.90 s. The average delay time is 1.09 s. The smallest $1\sigma_{\delta t}$ uncertainty for the delay time is 0.10 s, while the largest is 1.25 s. The average uncertainty is 0.46 s. Station SCIG only had two null measurements from nonorthogonal back azimuths, so it is interpreted to have splitting below the threshold of the data. The averaged splitting parameters are shown in Figure 1.

**Discussion**

Figure 1 shows the averaged splitting parameters at each station and the tectonic environment of the study area. The best coverage is found between 94 and 101°W longitude. The study area was divided into several regions based on variations in the tectonic environment as well as differences in the measured anisotropy parameters. They are discussed below.

*Mexican Subduction Zone Between 96 and 101°W Longitude*

In this region (Figure 1), subduction of the Cocos plate under the North American plate at the Middle America Trench (MAT) is bounded by the landward extension of the Orozco Fracture Zone (OFZ) and the Tehuantepec Ridge (TR). The relative velocity between the Cocos and North American plates increases from 5.7 cm/yr in the northwest to 7.3 cm/yr in the southeast (model PVEL in DeMets *et al.* (2010)) while the Cocos plate moves in the direction ~N31°E. The fast polarization direction for many stations in this region is approximately the same as the relative

**Table 3.** Averaged splitting parameters measured at each station.

| Station | Lat. (°N) | Long. (°E) | $\varphi$ (°) | $\sigma_\varphi$ (°) | $\delta t$ (s) | $\sigma_{\delta t}$ (s) | N Split | N Null | Location |
|---------|-----------|------------|---------------|----------------------|----------------|--------------------------|---------|--------|----------|
| CAIG | 17.05 | -100.27 | 43 | 10 | 1.30 | 0.60 | 4 | 1 | El Cayaco, Gro. |
| CCIG | 16.28 | -92.14 | 18 | 18 | 0.60 | 0.25 | 3 | 0 | Comitán, Chis. |
| CJIG | 19.50 | -105.04 | -18 | 13 | 0.70 | 0.40 | 2 | 3 | Chamela, Jal. |
| CMIG | 17.09 | -94.88 | 53 | 10 | 1.60 | 0.50 | 2 | 6 | Col. Cuauhtémoc, Oax. |
| COIG | 19.18 | -103.69 | 17 | 21 | 0.75 | 0.40 | 5 | 2 | Colima, Col. |
| CUIG[a] | 19.33 | -99.18 | 38 | 55 | 1.20 | 1.25 | 1 | 0 | Ciudad Universitaria, D. F. |
| HUIG | 15.77 | -96.11 | 50 | 43 | 1.10 | 0.60 | 1 | 10 | Huatulco, Oax. |
| LVIG | 19.72 | -96.42 | 45 | 7 | 1.35 | 0.45 | 4 | 0 | Laguna Verde, Ver. |
| MOIG | 19.68 | -101.19 | 71 | 5 | 1.00 | 0.20 | 4 | 3 | Morelia, Mich. |
| OXIG | 17.08 | -96.72 | 28 | 6 | 0.90 | 0.20 | 11 | 2 | Oaxaca, Oax. |
| PLIG | 18.39 | -99.50 | 57 | 5 | 1.10 | 0.20 | 19 | 3 | Platanillo, Gro. |
| PNIG | 16.40 | -98.13 | 23 | 11 | 0.50 | 0.30 | 3 | 3 | Pinotepa Nacional, Oax. |
| PPIG | 19.07 | -98.63 | 34 | 6 | 1.90 | 0.35 | 4 | 0 | Popocatépetl, Tlamacas, Pue. |
| SCIG | 18.97 | -91.19 | 00 | - | - | - | 0 | 2 | Sabancuy, Camp. |
| TEIG | 20.23 | -88.28 | 61 | 19 | 1.40 | 0.90 | 1 | 4 | Tepich, Q. R. |
| TPIG | 18.42 | -97.36 | 32 | 13 | 1.50 | 0.40 | 2 | 1 | Tehuacán, Pue. |
| TUIG | 18.03 | -94.42 | 53 | 49 | 1.25 | 1.25 | 1 | 3 | Tuzandépetl, Ver. |
| YAIG | 18.86 | -99.07 | 70 | 4 | 1.15 | 0.15 | 5 | 6 | Yautepec, Mor. |
| ZAIG | 22.77 | -102.57 | -61 | 5 | 0.85 | 0.10 | 6 | 5 | Zacatecas, Zac. |
| ZIIG | 17.61 | -101.47 | -13 | 13 | 0.60 | 0.20 | 4 | 0 | Zihuatanejo, Gro. |

Parameter $\varphi$ is the fast polarization direction (measured east of north), $\delta t$ is the delay time, and $\sigma_\varphi$ and $\sigma_{\delta t}$ are the 1σ uncertainties. Averages were calculated using the stacking method of Wolfe and Silver (1998). N is the number of measurements available for analysis. The abbreviations after the locations stand for the names of Mexican states.
The station with a 00 value for $\varphi$ and dashes for the next three columns does not exhibit splitting from at least two different nonorthogonal back azimuths ($\varphi_b$) and is interpreted as having splitting below the threshold of the data.
[a]Data at station CUIG are noisy, a measurement is provided but it is poorly constrained.

plate motion (RPM) between the Cocos and North American plates, and approximately perpendicular to the MAT. Most of these stations overlie the Cocos plate where it subducts subhorizontally (Pardo and Suárez, 1995; Pérez-Campos *et al.,* 2008; Husker and Davis, 2009) and likely reflect the flow direction of the upper mantle below the slab. Given the conditions expected to prevail beneath the slab, such as low stress, low water content, and relatively high temperature, we assume that the lattice preferred orientation (LPO) of olivine is of type-A (Jung *et al.,* 2006; Long and Silver, 2008). Therefore, the fast anisotropy axis and mantle flow are oriented in the same direction. It also follows that flow is entrained under the subhorizontal Cocos slab. Most regions

with substantial subslab splitting around the world, however, show trench-parallel $\phi$, which is interpreted as 3-D return flow induced by trench migration (Long and Silver, 2008). Perhaps the most notable exception is the Cascadia subduction zone, where a trench-perpendicular pattern has been found (Currie *et al.,* 2004; Long and Silver, 2008). Trench-perpendicular fast directions have also been reported by other studies in Mexico using *SKS* phases. Soto *et al.* (2009) found trench-perpendicular $\phi$ where the Rivera plate subducts beneath the Jalisco block (the region between stations CJIG and COIG in Figures 1 and 7 of this study). Data from the Mesoamerican Subduction Experiment (MASE) array, a line of 100 seismometers running north and starting just east
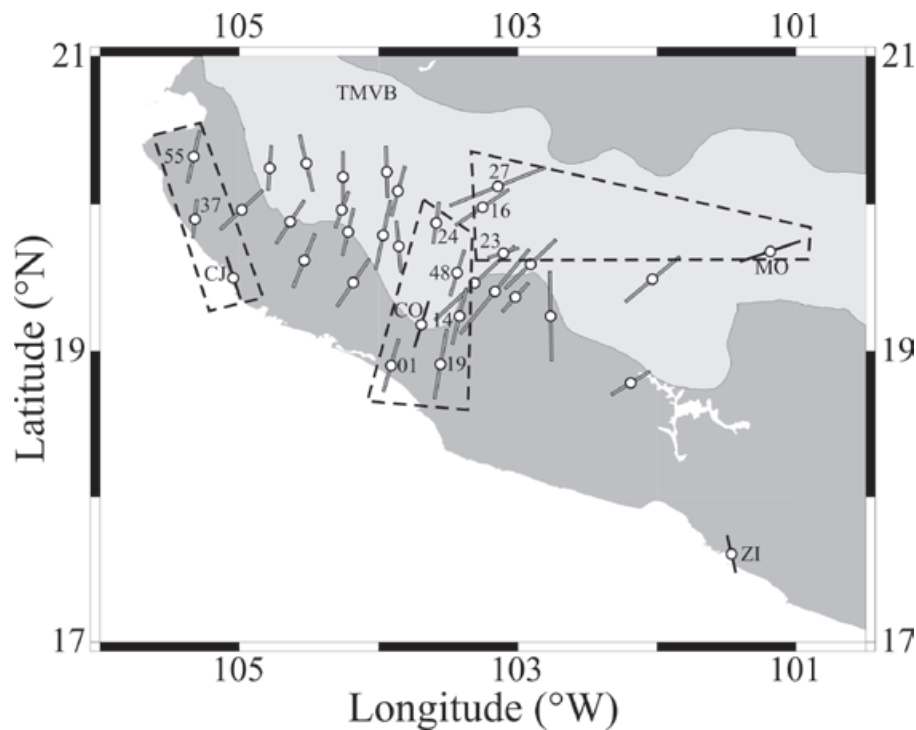
**Figure 7.** Map showing the relationship between measurements made at the MARS stations (Soto *et al.,* 2009) and those from SSN stations in the present study. The stations enclosed by dashed-line polygons are discussed in the main text. MARS station codes were shortened by dropping the MA- prefix.

of CAIG (Figure 1), show an average $\phi$ of N41°E for stations in the fore-arc, while $\phi$ averages N8°W for stations in the back-arc (the volcanic arc is located at the southern edge of the Trans-Mexican Volcanic Belt) (Stubailo and Davis, 2007, 2012a, 2012b; Rojo-Garibaldi, 2012). Farther east, measurements from the Veracruz-Oaxaca (VEOX) profile, a line of 46 seismometers running north-south across the Isthmus of Tehuantepec (just west of CMIG in Figure 1), reveal fast directions consistent with nearby SSN stations TUIG, CMIG, and HUIG (Bernal-Díaz *et al.,* 2008).

In order to allow for the 3-D return flow induced by trench migration observed at most subduction zones, Long and Silver (2008, 2009) propose the existence of a thin decoupling zone between the downgoing slab and the subslab mantle. The decoupling zone may result from the entrainment of a thin layer of buoyant asthenosphere which is produced through shear strain and shear heating (Phipps Morgan *et al.,* 2007; Long and Silver, 2008, 2009). In this study, however, the approximately trench-perpendicular fast directions observed beneath the Cocos plate in the Mexican states of Guerrero and Oaxaca, just like observations at Cascadia (Long and Silver, 2009), suggest that the thin decoupling zone does not exist. Therefore, the downgoing slab and sub-slab mantle are coupled at depth, which results in entrained flow. The age of the subducting oceanic Cocos plate at the MAT offshore Guerrero and Oaxaca is approximately between 12 and 16 Myr

(Kanjorski, 2003). Both Cascadia and the Middle America Trench represent the most extreme examples of the subduction of young lithosphere. Consequently, Long and Silver (2009) hypothesize that the amount of strain is not yet high enough for the shear mechanism to reach steady state and so decoupling has not yet occurred. Farther east along the MAT, in Nicaragua and Costa Rica, Abt *et al.* (2010) interpret their anisotropy measurements using teleseismic *SKS* and local *S* phases as mantle flow parallel to the trench, both beneath the subducted Cocos slab and in the mantle wedge. The age of the lithosphere subducting at the MAT there is between 18 and 24 Myr (Abt *et al.,* 2009).

The trench-perpendicular fast directions found beneath the Cocos plate in Guerrero and Oaxaca in the present study stand in contrast to the trench-parallel fast directions observed by Stubailo *et al.* (2012) using Rayleigh waves. They obtained phase velocity maps for waves of different periods in the range from 16 to 100 s. Since phase velocities provide a depth-integrated image of the upper mantle, they inverted the phase velocity maps and determined a 3-D model for shear wave velocity and anisotropy. Their model is parameterized into three layers: the continental crust, mantle lithosphere, and asthenosphere down to a depth of 200 km. Both the lithospheric and asthenospheric layers show trench-parallel fast directions in the fore-arc with values ranging between 0.5 and 2% $\psi$ in anisotropy. Farther west, coincident with

the landward projection of the Orozco Fracture Zone, the fast axes become trench-perpendicular. Stubailo *et al.* (2012) interpret these results as toroidal flow into the mantle wedge coming in from the two edges that limit the segment of the Cocos slab located between the OFZ to the east and the Rivera slab to the west. If the trench-parallel fast directions observed by Stubailo *et al.* (2012) in Guerrero and Oaxaca, where the slab is subhorizontal, are interpreted as 3-D return flow produced by trench rollback, this would be inconsistent with our interpretation of entrained flow. The delay times measured from *SKS* splitting in this region range from 0.5 to 1.9 s. Using the common assumption that shear wave anisotropy is 4% (Silver and Chan, 1991; Savage, 1999), a delay time of 1 s corresponds to an effective thickness for the anisotropic layer of 115 km. Therefore, the observed delay times translate into anisotropic layer thicknesses between 60 and 220 km. It is possible that the anisotropic regions sampled by the Rayleigh and *SKS* waves are different given that their paths are different. The sensitivity kernel for a period of 100 s peaks at a depth of 140 km (Stubailo *et al.,* 2012) and so Rayleigh waves sample the lithosphere preferentially. Thus, if the *SKS* anisotropic layer is placed under the Rayleigh wave anisotropic layer, it would start at a depth of ~150 km. Admittedly, the vertical resolution for shear wave splitting is poor, but it is generally agreed that anisotropy resides in the shallow part of the upper mantle (Silver, 1996; Savage, 1999). If the anisotropic layer in the present study is placed too deep, however, it will no longer be in contact with the subducted slab and consequently entrained flow cannot be used to explain the observed anisotropy. A possible way to resolve this discrepancy may be to carry out a joint inversion of the surface wave and *SKS* data. Anisotropy in this region has also been reported by other researchers. Song and Kim (2012b) found that the upper oceanic crust of the subducting Cocos slab is an ultraslow-velocity layer (USL). It is 3 to 5 km thick and it shows anisotropy larger than 5%. Additionally, Song and Kim (2012a) discovered that the topmost 2-6 km of the Cocos subducted oceanic mantle is an anisotropic high-velocity lid (HVL).

The average $\delta t \pm \sigma_{\delta t}$ for stations in the fore-arc with trench-perpendicular $\phi$ is 1.20±0.41 s. The trench migration (retreating) velocity for this segment of the MAT is 21 mm/yr (Heuret and Lallemand, 2005). Long and Silver (2008) proposed a relationship for average subslab $\delta t$ as a function of trench migration velocity, mostly for trench-parallel $\phi$ (Cascadia is an exception but it is also included). The values given above plot in their Figure 2 close to the entry for the MAT in Nicaragua and Costa Rica but $\delta t$ is smaller for Guerrero and Oaxaca, so they are roughly consistent with the trend observed by Long and

Silver (2008). Calculation with the equation given in the caption to their Figure 2 predicts $\delta t = 0.72$ s for the MAT in Guerrero and Oaxaca.

*Mexican Subduction Zone East of 96°W Longitude*

A slight (~25°) clockwise rotation of the anisotropy fast axes is observed for stations HUIG, CMIG, and TUIG relative to nearby stations PNIG, OXIG, and TPIG which are located to the west (Figure 1). These directions are also consistent with preliminary *SKS* results from the N-S VEOX profile deployed just west of CMIG (Bernal-Díaz *et al.,* 2008). Using VEOX data and local earthquakes within the Cocos slab, León-Soto *et al.* (2011) found that the fast anisotropy axis is trench-perpendicular in the mantle wedge. Several changes in subduction zone morphology take place in this area: (1) The Middle America Trench makes a bend southeast of station HUIG. (2) The Tehuantepec Ridge intersects the MAT. The TR has long been recognized as a sharp contrast in the properties of the Cocos plate. The oceanic crust of the Guatemala Basin in the southeast is older and deeper than the region northwest of the TR; see Manea *et al.* (2005) for a review. (3) The coastline is farther away from the MAT than in the area located to the west, which implies the existence of a broad continental shelf. (4) The subducting Cocos plate is not subhorizontal anymore and dips at an angle of ~25° (Pardo and Suárez, 1995; Rodríguez-Pérez, 2007; Melgar and Pérez-Campos, 2011; Kim *et al.,* 2011). Furthermore, recent results suggest the possibility of a tear in the slab somewhere in the region where it changes from subhorizontal to a dip of ~25° (Pérez-Campos *et al.,* 2012). The rotation of the *SKS* fast axes may be caused by the change in dip of the Cocos slab. Furthermore, this orientation may be transitional to the orientation of the fast axis at station TEIG in the Yucatán peninsula, which coincides with the absolute motion of the North American plate.

Farther east (Figure 1), the fast axis is oriented NNE-SSW and has a short delay time (0.60±0.25 s) at station CCIG. This direction agrees with the RPM between Cocos and North America and is roughly trench-perpendicular. South of CCIG the hypocenters reach depths of ~175 km and the Cocos slab subducts more steeply (~45°) than in the region to the west (Rodríguez-Pérez, 2007). The fast direction may be consistent with corner flow within the mantle wedge.

*Mexican Subduction Zone West of 101°W Longitude*

A few stations are available at the western end of the subducting Cocos plate and around the Rivera plate. Between the MAT and the coastline, the

θωερτψυιοπασδφγηφ

boundary between the Cocos and Rivera plates is continued by the bathymetric feature known as El Gordo Graben, which further extends on land as the N-S trending Colima rift. Additionally, Colima volcano is located within the rift. The Rivera plate subducts more steeply than the adjacent Cocos slab (Pardo and Suárez, 1995) and a gap between the two was imaged tomographically at depths greater than 150 km (Yang *et al.,* 2009). This gap is located under the rift. Delay times at stations CJIG, COIG, and ZIIG are short and range from 0.60 to 0.75 s (Figure 1). Soto *et al.* (2009) previously used data from CJIG and COIG together with records from the Mapping the Rivera Subduction Zone (MARS) experiment. The present study concurs with the interpretation of Soto *et al.* (2009). The fast direction at station CJIG, and also at their stations MA37 and MA55, shows that the subslab mantle beneath the fore-arc flows around the western edge of the Rivera slab as the subducted plate rolled back (Figure 7). The fast directions at COIG and stations MA01, MA14, MA19, MA24, and MA48 (Soto *et al.,* 2009) within the Colima rift (Figure 7) are consistent with mantle flow through the slab gap between the Rivera and Cocos plates, and perhaps with the fact that Colima volcano is located within the rift (Yang *et al.,* 2009). Ferrari *et al.* (2001) documented rollback of the Rivera plate based on the trenchward migration of the volcanic front and further proposed asthenospheric infiltration into the mantle wedge from both the western and eastern edges of the subducted Rivera slab. Recent results of laboratory, analog models of the Rivera and Cocos slabs reveal complex patterns of toroidal and corner flows in agreement with seismic anisotropy studies (Neumann *et al.,* 2012).

The *SKS* fast axis at station ZIIG is oriented N13°W and looks clearly different from observations to the east, where the fast axis is roughly parallel to the RPM between Cocos and North America (Figure 1). ZIIG is located near the projected extension of the Orozco Fracture Zone beneath the North American plate. The subducting Cocos plate dips more steeply west of the projected OFZ than to the east, where the subhorizontal slab is found (Pardo and Suárez, 1995). Both Stubailo *et al.* (2012) and Dougherty *et al.* (2012) presented evidence for a tear in the Cocos slab underneath the projection of the OFZ. The *SKS* anisotropy pattern at ZIIG is consistent with flow through the gap in between the two segments of the torn slab. Furthermore, Stubailo *et al.* (2012) interpreted the anisotropy in their Rayleigh wave data in terms of toroidal mantle flow around the slab edges driven by slab rollback (Ferrari, 2004). The fast anisotropy axes in the region around ZIIG from surface wave data sampling the mantle lithosphere and asthenosphere are oriented slightly east of north (Stubailo *et al.,* 2012) and

are somewhat different from the *SKS* data in the present study given that the fast axis at ZIIG is oriented slightly west of north.

*Fast Axes Oriented With the Absolute Plate Motion of North America*

The absolute motion of the North American plate throughout southern Mexico is about 4 cm/yr and is oriented in a direction ~N254°E according to model HS3-NUVEL1A in Gripp and Gordon (2002); see Figure 1. A few stations (MOIG, YAIG, and PLIG) in or near the TMVB have their fast directions aligned with the APM and their delay times range from 1.00 to 1.15 s. Such a pattern can be explained as the rigid lithosphere moves and consequently drags the asthenosphere below (Silver, 1996). It is expected in regions where other tectonic processes have not operated and is observed frequently. The alignment of the fast axes with the APM at these stations may signal a change in the tectonic regime as one moves away from the MAT. Soto *et al.* (2009) found the fast axes for stations within the Colima rift oriented ~N-S. Stations located just east of the Colima rift and south of the Chapala-Tula rift (CTR), however, show fast axes rotated to ~NE-SW and ~ENE-WSW. Interestingly, the fast axes at the northernmost stations MA16, MA23, and MA27, just south of the CTR, agree with the measurements at MOIG located at about the same latitude but ~200 km farther east (Figure 7), which might suggest a consistent trend for stations within the TMVB east of Colima rift.

A single splitting measurement at CUIG (38±55°, 1.20±1.25 s) is poorly constrained but its large 95% confidence interval is consistent with nearby stations in the northern segment of the MASE deployment where the fast direction is oriented slightly west of north (Rojo-Garibaldi, 2012). Station TEIG was installed in the Yucatán peninsula and is found in an entirely different tectonic setting. The fast axis here agrees with the APM of North America and is consistent with its location away from current plate boundaries.

*Station ZAIG in the Mesa Central*

ZAIG is the northernmost station in the present study (Figure 1). The SSN coverage in this part of the country is sparse since it is far away from the seismogenic plate boundaries. The fast axis is oriented WNW-ESE and is clearly different from that observed in any of the other stations analyzed. The station is located within the Mesa Central, which is an elevated plateau and is recognized as a morphotectonic province. It is bounded to the south by the TMVB, to the west by the Sierra Madre Occidental, and to the north and east by the Sierra Madre Oriental (SMOr), which separates it from the Eastern Mexican

Basin and Range farther north (Sedlock *et al.,* 1993). The Mesa Central was under compression during the Laramide orogeny which created the SMOr to the east (Nieto-Samaniego *et al.,* 2005). It was subsequently subjected to extension, likely related to the Basin and Range. The main episodes of extension occurred during the Eocene, oriented NE-SW; and during the Oligocene, with predominant extension of ~20% oriented E-W plus ~10% extension oriented N-S (Nieto-Samaniego *et al.,* 2005). Neither the episodes of compression nor extension can explain the orientation of $\phi$. The fast axis is predicted to align parallel to transpressional structures, and parallel to the extension direction (Silver, 1996). The APM of North America cannot explain the orientation of $\phi$ either (Figure 1). It should be mentioned that in the Western Mexican Basin and Range the direction of $\phi$ is consistent with both the current APM of North America and with extension during the Miocene (Obrebski *et al.,* 2006; van Benthem *et al.,* 2008). Comparison with the Rayleigh wave model of Stubailo *et al.* (2012) shows that ZAIG is located in their low resolution area. It is nonetheless interesting that the fast direction in their model at periods from 44 to 85 s agrees with the fast direction observed in the present study.

Another possibility for explaining the anisotropy at ZAIG is to look at the evolution of the subducted slab in the mantle. The *P* wave velocity tomographic model of Yang *et al.* (2009) can image the subducted Rivera plate down to depths of ~350 km. They speculate that the leading edge of the slab may have detached from the upper portion and might be found at greater depths. Likewise, the adjacent Cocos slab to the east can be followed as a continuous feature from the surface down to a depth of ~400 km, which is the lower limit of their model. The *S* wave velocity tomographic model of van der Lee and Nolet (1997a, 1997b) images the broken and subducted Farallon plate in the upper mantle. The slab shows roughly a WNW-ESE trend, which agrees with the fast anisotropy axis at ZAIG. The southernmost extent of the Farallon slab at a depth of ~350 km is located underneath station ZAIG. Being at such a great depth it is unclear, however, how the slab might control the anisotropy observed at ZAIG. On the other hand, the *P* wave velocity tomography of Gorbatov and Fukao (2005) shows the Farallon slab under ZAIG at a depth of ~400 km, but it trends roughly E-W.

## Conclusions

The fast anisotropy polarization directions for stations located where the Cocos plate subducts subhorizontally, beneath Guerrero and Oaxaca states, are oriented with the relative motion between the Cocos and North American plates and are perpendicular to the Middle America Trench. This observation is consistent with subslab entrained flow in a regime of type-A olivine. The situation is similar to that reported in Cascadia, except that the slab is not subhorizontal. At most subduction zones around the world, however, $\phi$ is trench-parallel, which may be caused by a thin asthenospheric layer that decouples the downgoing slab from the subslab mantle and allows flow to be driven by trench migration. Given the young age of the lithosphere being subducted, both in Mexico and in Cascadia, the decoupling layer may be absent. The fast directions observed around the edges of the Rivera slab, and near the projection of the Orozco Fracture Zone under the continent, are consistent with mantle flow around the edges of the torn slabs. Furthermore, this flow is driven by slab rollback. Stations located east of the subhorizontal slab, where the subducting plate starts to increase its dip, show a slight clockwise rotation of their fast axes relative to nearby stations located to the west. A few stations in or near the TMVB, and away from the plate boundaries, show fast directions consistent with asthenospheric flow driven by the absolute motion of the North American plate. The same is also true for one station in the Yucatán peninsula. Finally, the fast polarization direction for a single station within the Mesa Central is oriented WNW-ESE and it is different from measurements at any of the other stations. Previous episodes of compression and subsequent extension in the region fail to account for this direction. The fast direction is also inconsistent with the APM of North America.

## Bibliography

Abt D.L., Fischer K.M., Abers G.A., Strauch W., Protti J.M., González V., 2009, Shear wave anisotropy beneath Nicaragua and Costa Rica: Implications for flow in the mantle wedge, *Geochem. Geophys. Geosyst.,* 10, Q05S15, doi:10.1029/2009GC002375.

Abt D.L., Fischer K.M., Abers G.A., Protti M., González V., Strauch W., 2010, Constraints on upper mantle anisotropy surrounding the Cocos slab from *SK(K)S* splitting, *J. Geophys. Res.,* 115, B06316, doi:10.1029/2009JB006710.

Bernal-Díaz A., Valenzuela-Wong R., Pérez-Campos X., Iglesias A., Clayton R.W., 2008, Anisotropía de la onda *SKS* en el manto superior debajo del arreglo VEOX (abstract), *Geos Boletín Informativo de la UGM,* 28, 2, 199-200.

Currie C.A., Cassidy J.F., Hyndman R.D., Bostock M.G., 2004, Shear wave anisotropy beneath the Cascadia subduction zone and western North American craton, *Geophys. J. Int.,* 157, 341-353.

DeMets C., Gordon R.G., Argus D.F., 2010, Geologically current plate motions, *Geophys. J. Int.,* 181, 1-80.

Dougherty S.L., Clayton R.W., Helmberger D.V., 2012, Seismic structure in central Mexico: Implications for fragmentation of the subducted Cocos plate, *J. Geophys. Res.,* 117, B09316, doi:10.1029/2012JB009528.

Ferrari L., 2004, Slab detachment control on mafic volcanic pulse and mantle heterogeneity in central Mexico, *Geology,* 32, 77-80, doi:10.1130/G19887.1.

Ferrari L., Petrone C.M., Francalanci L., 2001, Generation of oceanic-island basalt-type volcanism in the western Trans-Mexican volcanic belt by slab rollback, asthenosphere infiltration, and variable flux melting, *Geology,* 29, 507-510.

Gorbatov A., Fukao Y., 2005, Tomographic search for missing link between the ancient Farallon subduction and the present Cocos subduction, *Geophys. J. Int.,* 160, 849-854.

Gripp A.E., Gordon R.G., 2002, Young tracks of hotspots and current plate velocities, *Geophys. J. Int.,* 150, 321-361.

Heuret A., Lallemand S., 2005, Plate motions, slab dynamics and back-arc deformation, *Phys. Earth Planet. Int.,* 149, 31-51, doi:10.1016/j.pepi.2004.08.022.

Husker A., Davis P.M., 2009, Tomography and thermal state of the Cocos plate subduction beneath Mexico City, *J. Geophys. Res.,* 114, B04306, doi:10.1029/2008JB006039.

Jung H., Katayama I., Jiang Z., Hiraga T., Karato S., 2006, Effect of water and stress on the lattice-preferred orientation of olivine, *Tectonophysics,* 421, 1-22.

Kanjorski M.N., 2003, Cocos plate structure along the Middle America subduction zone off Oaxaca and Guerrero, Mexico: Influence of subducting plate morphology on tectonics and seismicity, Ph. D. thesis, University of California, San Diego, USA.

Kim Y., Clayton R.W., Keppie F., 2011, Evidence of a collision between the Yucatán block and Mexico in the Miocene, *Geophys. J. Int.,* 187, 989-1000, doi: 10.1111/j.1365-246X.2011.05191.x.

León-Soto G., González-López A., Valenzuela-Wong R., Pérez-Campos X., Iglesias A., Clayton R.W., 2011, Anisotropía sísmica de ondas *S* locales en el Istmo de Tehuantepec (abstract), *Geos Boletín Informativo de la UGM,* 31, 1, 117.

Long M.D., 2010, Frequency-dependent shear wave splitting and heterogeneous anisotropic structure beneath the Gulf of California region, *Phys. Earth Planet. Int.,* 182, 59-72, doi:10.1016/j.pepi.2010.06.005.

Long M. D., Silver P. G., 2008, The subduction zone flow field from seismic anisotropy: A global view, *Science,* 319, 315-318.

Long M.D., Silver P.G., 2009, Mantle flow in subduction systems: The subslab flow field and implications for mantle dynamics, *J. Geophys. Res.,* 114, B10312, doi:10.1029/2008JB006200.

Manea M., Manea V. C., Ferrari L., Kostoglodov V., Bandy W. L., 2005, Tectonic evolution of the Tehuantepec ridge, *Earth Planet. Sci. Lett.,* 238, 64-77.

Melgar D., Pérez-Campos X., 2011, Imaging the Moho and subducted oceanic crust at the Isthmus of Tehuantepec, Mexico, from receiver functions, *Pure Appl. Geophys.,* 168, 1449-1460, doi:10.1007/s00024-010-0199-5.

Neumann F., Contreras-Pérez J., Tolson-Jones G., Vásquez-Serrano A., 2012, An analog model of the Middle American subduction zone and the mantle flow beneath the Jalisco and Michoacán blocks (abstract), *Geos Boletín Informativo de la UGM,* 32, 1, 252.

Nieto-Samaniego A.F., Alaniz-Alvarez S.A., Camprubí-í-Cano A., 2005, La Mesa Central de México: Estratigrafía, estructura y evolución tectónica cenozoica, *Bol. Soc. Geol. Mex.,* LVII, 285-318.

Obrebski M., Castro R.R., 2008, Seismic anisotropy in northern and central Gulf of California region, Mexico, from teleseismic receiver functions and new evidence of possible plate capture, *J. Geophys. Res.,* 113, B03301, doi:10.1029/2007JB005156.

Obrebski M., Castro R.R., Valenzuela R.W., van Benthem S., Rebollar C.J., 2006, Shear-wave splitting observations at the regions of northern Baja California and southern Basin and Range in Mexico, *Geophys. Res. Lett.,* 33, L05302, doi:10.1029/2005GL024720.

Pardo M., Suárez G., 1995, Shape of the subducted Rivera and Cocos plates in southern Mexico: Seismic and tectonic implications, *J. Geophys. Res.,* 100, 12,357-12,373.

Park J., Levin V., 2002, Seismic anisotropy: Tracing plate dynamics in the mantle, *Science,* 296, 485-489.

Pérez-Campos X., Kim Y., Husker A., Davis P.M., Clayton R.W., Iglesias A., Pacheco J.F., Singh S.K., Manea V.C., Gurnis M., 2008, Horizontal subduction and truncation of the Cocos plate beneath central Mexico, *Geophys. Res. Lett.,* 35, L18303, doi:10.1029/2008GL035127.

Pérez-Campos X., Clayton R.W., Brudzinski M.R., Cabral E., Arciniega A., 2012, Slab geometry under Oaxaca and its relationship with the eastern Trans-Mexican Volcanic Belt (abstract), *Geos Boletín Informativo de la UGM,* 32, 1, 254.

Phipps Morgan J., Hasenclever J., Hort M., Rüpke L., Parmentier E.M., 2007, On subducting slab entrainment of buoyant asthenosphere, *Terra Nova,* 19, 167-173, doi:10.1111/j.1365-3121.2007.00737.x.

Rodríguez-Pérez Q., 2007, Estructura tridimensional de velocidades para el sureste de México, mediante el análisis de trazado de rayos sísmicos de sismos regionales, M.

Sc. thesis, 83 pp., Instituto de Geofísica, Universidad Nacional Autónoma de México, Mexico City, Mexico.

Rojo-Garibaldi B., 2012, Anisotropía de las ondas *SKS* en el manto superior debajo de un arreglo sísmico entre Guerrero y Veracruz, B. Sc. thesis, 84 pp., Facultad de Ciencias, Universidad Nacional Autónoma de México, Mexico City, Mexico.

Savage M.K., 1999, Seismic anisotropy and mantle deformation: What have we learned from shear wave splitting?, *Rev. Geophys.,* 37, 65-106.

Sedlock R.L., Ortega-Gutiérrez F., Speed R.C., 1993, *Tectonostratigraphic terranes and tectonic evolution of Mexico, Special Paper 278,* 146 pp., Geological Society of America, Boulder, Colorado, USA.

Silver P.G., 1996, Seismic anisotropy beneath the continents: Probing the depths of Geology, *Annu. Rev. Earth Planet. Sci.,* 24, 385-432.

Silver P.G., Chan W.W., 1991, Shear wave splitting and subcontinental mantle deformation, *J. Geophys. Res.,* 96, 16,429-16,454.

Singh S.K., Pacheco J., Courboulex F., Novelo D.A., 1997, Source parameters of the Pinotepa Nacional, Mexico, earthquake of 27 March, 1996 ($M_w$ = 5.4) estimated from near-field recordings of a single station, *J. Seismol.,* 1, 39-45.

Song T.-R. A., Kim Y., 2012a, Anisotropic uppermost mantle in young subducted slab underplating central Mexico, *Nat. Geosci.,* 5, 55-59, doi:10.1038/ngeo1342.

Song T.-R. A., Kim Y., 2012b, Localized seismic anisotropy associated with long-term slow-slip events beneath southern Mexico, *Geophys. Res. Lett.,* 39, L09308, doi:10.1029/2012GL051324.

Soto G.L., Ni J.F., Grand S.P., Sandvol E., Valenzuela R.W., Guzmán Speziale M., Gómez González J.M., Domínguez Reyes T., 2009, Mantle flow in the Rivera-Cocos subduction zone, *Geophys. J. Int.,* 179, 1004-1012, doi: 10.1111/j.1365-246X.2009.04352.x.

Stubailo I., Davis P., 2007, Shear wave splitting measurements and interpretation beneath Acapulco-Tampico transect in Mexico, *Eos Trans. AGU,* 88, 52, Fall Meet. Suppl., Abstract T51B-0539.

Stubailo I., Davis P.M., 2012a, Anisotropy of the Mexico subduction zone based on shear-wave splitting analysis (abstract), *Seism. Res. Lett.,* 83, 2, 379.

Stubailo I., Davis P.M., 2012b, Anisotropy of the Mexico subduction zone based on shear-wave splitting and higher modes analysis, Abstract T11A-2538 presented at 2012 Fall Meeting, AGU, San Francisco, CA, 3-7 Dec.

Stubailo I., Beghein C., Davis P.M., 2012, Structure and anisotropy of the Mexico subduction zone based on Rayleigh-wave analysis and implications for the geometry of the Trans-Mexican Volcanic Belt, *J. Geophys. Res.,* 117, B05303, doi:10.1029/2011JB008631.

van Benthem S.A.C., Valenzuela R.W., Obrebski M., Castro R.R., 2008, Measurements of upper mantle shear wave anisotropy from stations around the southern Gulf of California, *Geofís. Int.,* 47, 127-143.

van der Lee S., Nolet G., 1997a, Seismic image of the subducted trailing fragments of the Farallon plate, *Nature,* 386, 266-269.

van der Lee S., Nolet G., 1997b, Upper mantle *S* velocity structure of North America, *J. Geophys. Res.,* 102, 22,815-22,838.

Wessel P., Smith W.H.F., 1998, New, improved version of Generic Mapping Tools released, *Eos Trans. AGU,* 79, 579.

Wolfe C.J., Silver P.G., 1998, Seismic anisotropy of oceanic upper mantle: Shear wave splitting methodologies and observations, *J. Geophys. Res.,* 103, 749-771.

Yang T., Grand S.P., Wilson D., Guzmán-Speziale M., Gómez-González J.M., Domínguez-Reyes T., Ni J., 2009, Seismic structure beneath the Rivera subduction zone from finite-frequency seismic tomography, *J. Geophys. Res.,* 114, B01302, doi:10.1029/2008JB005830.